2P

STUDY OF AN INSTRUMENT FOR SENSING ERRORS IN A TELESCOPE WAVEFRONT

L. J. Golden
R. V. Shack
P. N. Slater

Final Report
Prepared for the
George C. Marshall Space Flight Center
Marshall Space Flight Center
Alabama 35812
Under National Aeronautics and
Space Administration
Contract NAS8-27863

Optical Sciences Center
The University of Arizona
Tucson, Arizona 85721

May 1974

ABSTRACT

This report describes two years of work on NASA contract NAS8-27863 entitled "Study of an Instrument for Sensing Errors in a Telescope Wavefront." It contains results of theoretical and experimental investigations of different focal plane sensors for determining the error in a telescope wavefront.

The construction of three candidate test instruments and their evaluation in terms of small wavefront aberration measurements are described. A laboratory wavefront error simulator was designed and fabricated to evaluate the various test instruments. This simulator can introduce low-order aberrations up to several waves in magnitude, with an incremental adjustment capability better than $\lambda/100$. Each aberration type can be introduced independently and with any orientation desired. The laboratory wavefront error simulator was used to evaluate three tests, a Hartmann test, a polarization shearing interferometer test, and an interferometric Zernike test.

The Hartmann test was chosen for its relatively wide range of operation, potential sensitivity, and relative simplicity. The Hartmann test configuration is discussed and analyzed, and the construction of an experimental test instrument is described.

The wavefront error simulator was used to determine experimentally the Hartmann test instrument's capability to detect different amounts of low-order aberrations of different types under laboratory

conditions. *It was found that sensitivities in the λ/50 to λ/100 range could be realized.*

The polarization shearing interferometer test was chosen for the purpose of evaluating a polarization type readout using a star source. A lateral shearing polarization interferometer was evaluated analytically to predict sensitivities based on available star sources. An error analysis was done considering the effects of alignment and fabrication errors. The fabricated interferometer was evaluated with the wavefront error simulator, using a laser star source. *Sensitivities of λ/100 were obtained under laboratory conditions.*

The Zernike test was chosen for its potential high sensitivity and simplicity. A new interpretation from an interferometric point of view is presented for the Zernike test. Analytical expressions are derived for the interference effects, in terms of physically controllable Zernike disk parameters (radius, phase, and transmission) and low-order aberrations. These provide a method for choosing the Zernike disk parameters so as to optimize performance for maximum sensitivity and linear range. Using these parameters, a signal-to-noise analysis was performed to predict sensitivity.

A step-by-step procedure for manufacturing a Zernike disk and the design and fabrication of a laboratory model of the Zernike test instrument are described. The laboratory wavefront error simulator was used to evaluate the low-order aberration measurement sensitivity of the Zernike test instrument. *Sensitivities were found to be better than λ/100 for all the low-order aberration types.*

CONTENTS

TABLE OF CONTENTS--(Continued)

LIST OF ILLUSTRATIONS

LIST OF ILLUSTRATIONS--Continued

LIST OF ILLUSTRATIONS--Continued

LIST OF ILLUSTRATION--Continued

LIST OF TABLES

CHAPTER 1

INTRODUCTION

The purpose of the work carried out at the Optical Sciences Center under contract NAS8-27863 was to conduct experimental and analytical research on optical testing concepts suitable for application to the Large Space Telescope (LST) program. The following report includes much of the analytical procedures and experimental design information that was reported in the first-year interim report. In addition, this final report contains actual experimental evaluation of the various optical testing concepts and a bibliography on optical testing.

For LST application, an optical testing device, which we will refer to for brevity as a figure sensor, should have a wide dynamic range from a few waves to about a hundredth of a wave. Such a sensor would serve as an absolute standard for alignment-associated problems and as a means of sensing figure errors for the purpose of correction or measuring wavefront errors for post-detection image processing. For these purposes either selected wavefront samples or the entire system wavefront should be accessible for measurement. In order to accomplish these goals the figure sensor has to be placed at the focal plane of the telescope, and a real star source has to be used.

Under the premise that there is no single test that has the range required for alignment-associated wavefront errors and also the sensitivity required ($\lambda/100$) for image processing and figure correction,

we divided our work into a study of (1) a coarse-range geometrical sensor operating from several waves to a large fraction of a wave, and (2) a fine-range sensor useful from a large fraction of a wave to approximately $\lambda/100$. We narrowed our study to one candidate in the coarse range (a modified Hartmann test) and to three contenders in the fine-range region (Zernike test, shearing polarization test, and Zernike polarization test). These are discussed in detail in this report. We expected that many of the components used in the fine-range sensor would also be suitable for use with the coarse-range sensor and that the range of operation for coarse and fine sensing would have significant overlap.

CHAPTER 2

ABERRATED TELESCOPE WAVEFRONT SIMULATOR

1. General

In order to experimentally determine the performance capabilities of the various types of figure sensors, we designed and fabricated a device to produce a simulated aberrated telescope wavefront. This simulator includes a variable magnitude star, imaged by a specially designed telescope that can introduce various alignment, focus, and figure errors such as may occur in the operational LST. The aberrated star image produced can then be evaluated by the figure sensor under study. A sketch of the simulator appears in Fig. 1. The star source illuminator consists of a quartz iodine tungsten filament lamp, which is run by a stabilized power supply. The filament is focused onto a 25-μm pinhole, through a narrow band interference filter if required. The star source can be moved in the x,y direction to simulate wavefront tilt in any direction. This light is collimated by a 1.2-m

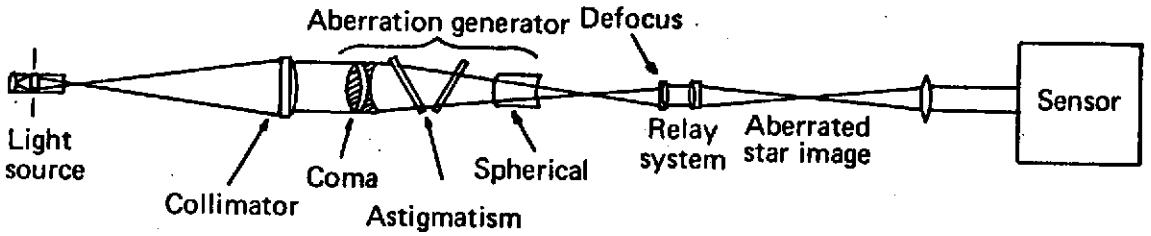

Fig. 1. Aberrated telescope wavefront simulator.

(48-in.) focal length telescope objective to simulate a star at infinity. The next five elements (biconvex lens, biconcave lens, two flat plates, and thick meniscus) are collectively called the aberration generator. This group of elements produces an f/6 beam into which various orientations and magnitudes of coma, astigmatism, and spherical aberration may be introduced in an exact manner. A relay system then reimages the f/6 image. The first element of the relay system is a 40-mm cemented doublet that collimates the aberrated star image. The element can be moved along the optical axis of the system in order to correct for focus shift produced by the aberration generator or in order to introduce known amounts of defocus into the wavefront. The second element of the relay system is an 80-mm focal length telescope objective, which converges the light to an f/12 cone, completing the simulation of an f/12 telescope where tilt, defocus, astigmatism, coma, and spherical aberration can be introduced into the beam in differential amounts of about $\lambda/100$ and over the range of ± 2 waves. The final collimating lens is related to the figure sensor under test and will be discussed in detail later.

2. Aberration Generator

At the heart of the aberrated telescope wavefront simulator is the aberration generator. This instrument has been designed to introduce precisely known amounts and orientations of different primary aberration types. What follows is a discussion of the design concept, the optical evaluation, the mechanical components, and the systematic error and calibration of the aberration generator.

a. Design Concept

The optical design is shown diagrammatically in Fig. 2. The instrument consists of an achromatic air-spaced doublet with a 25.4-mm clear aperture and a 152.4-mm focal length. The air-spaced doublet is designed for high coma but minimum spherical and chromatic aberration.

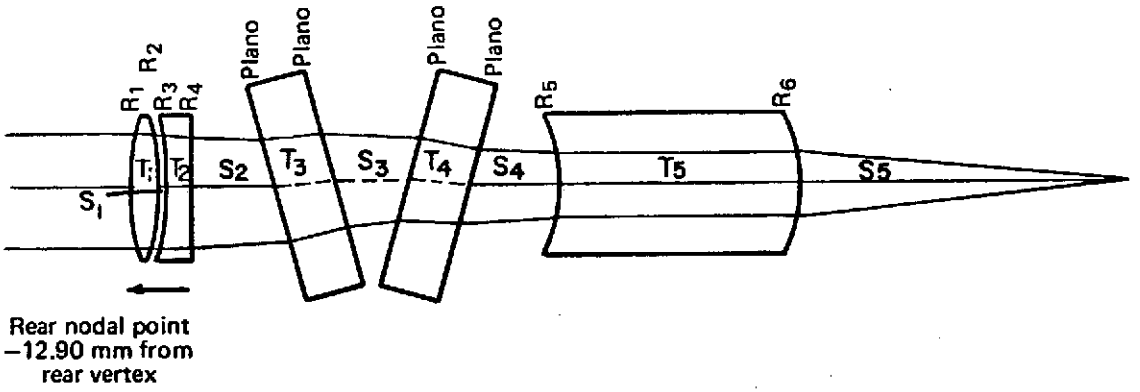

$R_1 = R_2 = 65.94$ mm
$R_3 = 59.36$ mm
$R_4 = 269.72$ mm
$R_5 = R_6 = 44.72$ mm
$T_1 = 6.36$ mm
$T_2 = 5.08$ mm
$T_3 = T_4 = 12.70$ mm
$T_5 = 51.08$ mm
$S_1 = 1.27$ mm
$S_2 + S_3 + S_4 = 51.46$ mm
when tilts = 0°
$S_5 = 70.87$ mm

Element 1: diameter = 30.18 mm
Element 2: diameter = 30.18 mm
Element 3: diameter = 47.62 mm
Element 4: diameter = 47.62 mm
Element 5: diameter = 30.18 mm
Glass: element 2 = Schott F4
all others = Schott SK4
Coatings: all MgF_2, n = 1.62
Maximum tilt of plates ≈ 15° (astigmatism)
Maximum tilt of front doublet = 1.5° (coma)
12-mm leftward movement of meniscus = 2.8 waves of −OPD
20-mm rightward movement of meniscus = 1.2 waves of +OPD
Maximum image excursion ≈ 3 mm

Fig. 2. Aberration generator; achromatic, nominal 5900 Å, nominal 152-mm EFL, f/6.

The residual astigmatism, inherent in a doublet design, is unavoidable but can be readily taken into account. This doublet is tilted about its rear nodal point (located 12.90 mm inside the last radius R_4) to generate approximately 2 waves to third-order coma at a tilt of 1.5°. About 0.4 waves of sagittal astigmatism are generated unavoidably at this angle. However, since the coma varies linearly with tilt, while the astigmatism varies quadratically, the astigmatism will be negligible for small amounts of coma (i.e., for up to about a quarter wave of coma, the residual astigmatism is less than $\lambda/100$). Higher-order aberration terms are negligible for the objective. Although the doublet is color corrected, a 40- to 50-nm bandwidth filter should be used for precise work. Following the doublet are a set of parallel plates that can be counter tipped to introduce astigmatism. No third-order coma is introduced, and higher-order aberrations are negligible. These plates can be tilted up to 15°, at which point 4.4 waves of sagittal astigmatism are introduced. Again, this astigmatism contribution varies quadratically. The last element, a thick miniscus lens, can be moved longitudinally for generation of +2.8 to -1.2 waves of spherical aberration. However, the effect of moving this meniscus is complicated since both fifth- and third-order spherical aberration are changed. A change in focal position and effective focal length must also be taken into account.

b. Optical Evaluation

i. Coma

The air-spaced doublet has been ray traced at a field angle of

1.5°, and the important coefficients for two wavelengths appear below in Table I.

Table I

Design coefficients for air-spaced doublet

λ = 546.1 nm, Field Angle 1.5°					
SA3	SA5	SA7	CMA3	CMA5	AST3
-1.84587E-3	+1.70755E-3	+1.86313E-4	-2.23989E-3	-1.7334E-5	-8.95394E-4
λ = 632.8 nm					
-2.57982E-3	1.66305E-3	1.87093E-4	-2.22001E-3	-2.45111E-5	-8.92584E-4

The meniscus element is positioned to minimize any spherical aberration residual. Because extrinsic higher-order aberration contributions are small and higher-order coma and astigmatism are negligible, we can compute the optical path difference (OPD) changes introduced by the doublet by using

$$OPD_{Doublet} = -\frac{1}{2} CMA3r^3 \cos\phi U - \frac{1}{4} AST3(\cos 2\phi + 1)r^2U^2,$$

where r is the fractional pupil height, ϕ is the angle measured from a direction perpendicular to the tilt axis, and U is the fractional tilt angle. As mentioned before, for OPD ≤ ¼ wave, the astigmatism contribution is < λ/100 and can be ignored.

ii. Astigmatism

The two plane-parallel plates were ray traced at an angle of 15° in an f/6 convergent beam. Because of the high degree of correction in the objective, it is expected that extrinsic contributions due to objective imperfection will be negligible. Since two counter-tipped plates are used, the third-order coma cancels and the third-order astigmatism dominates, with higher-order aberrations inconsequential. The meniscus element is positioned to minimize the residual spherical aberration. A summary of the third- and fifth-order coefficients for the two counter-tipped plates appears in Table II. The OPD due to astigmatism is calculated from

$$OPD_{Astigmatism} = -\frac{1}{4} AST3(\cos 2\phi + 1) r^2 U^2.$$

Table II

Design coefficients for astigmatism

	SA3	SA5	AST3	AST5
λ = 546.1 nm, Plate Tilt 15°				
	4.68100E-4	-1.50419E-6	4.83740E-3	-1.60639E-6
λ = 632.8 nm				
	4.67761E-4	-1.49766E-6	4.833908E-3	-1.599410E-6

iii. Spherical aberration

The position of the meniscus element relative to the doublet will determine the amount of spherical aberration in the system. Strictly speaking, this aberration contribution is very complex; third-, fifth-, seventh-, and higher-order spherical coefficients are used to determine the OPD in the pupil. However, from comparisons of exact ray trace OPD to those calculated by using third-, fifth-, and seventh-order coefficients, the computational error is always better than 5% or 7% in the OPD, where the smaller percentage refers to meniscus position changes made to introduce small errors (approximately $\lambda/10$), and the larger percentage refers to meniscus position changes made to introduce larger errors (approximately $\lambda/2$). The OPD is calculated from

$$OPD = -\frac{1}{8} SA3r^4 - \frac{1}{12} SA5r^6 - \frac{1}{16} SA7r^8.$$

As we reposition the meniscus we also change the back focal position (BFP) and the aberration generator effective focal length (GEFL). This change in BFP is compensated in the relay optics, and the change in GEFL results in an f/No. change that can be compensated by stopping down the pupil in order to maintain an f/6 cone in the generator and an f/12 cone in the simulator. Figure 3 illustrates the BFP as a function of meniscus position. Figure 4 shows the GEFL as a function of meniscus position. Figures 5, 6, and 7 show the variation of third-, fifth-, and seventh-order spherical aberration with meniscus position for two wavelengths.

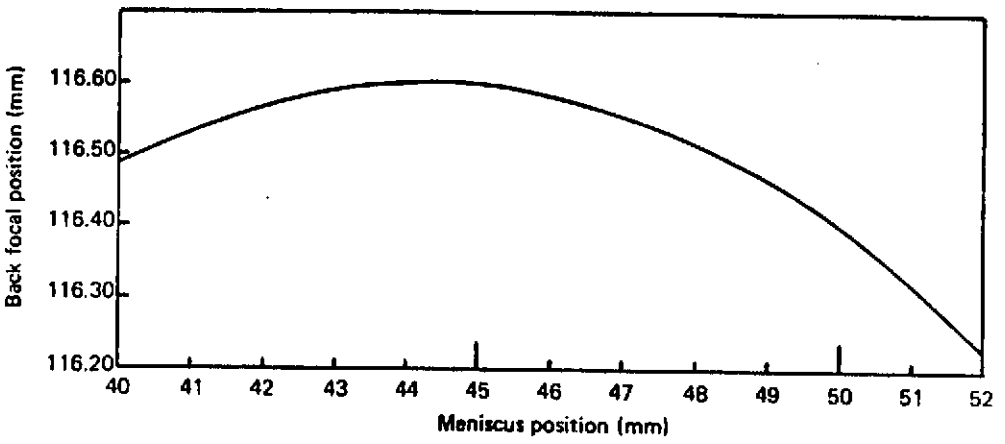

Fig. 3. Back focal position as a function of meniscus position.

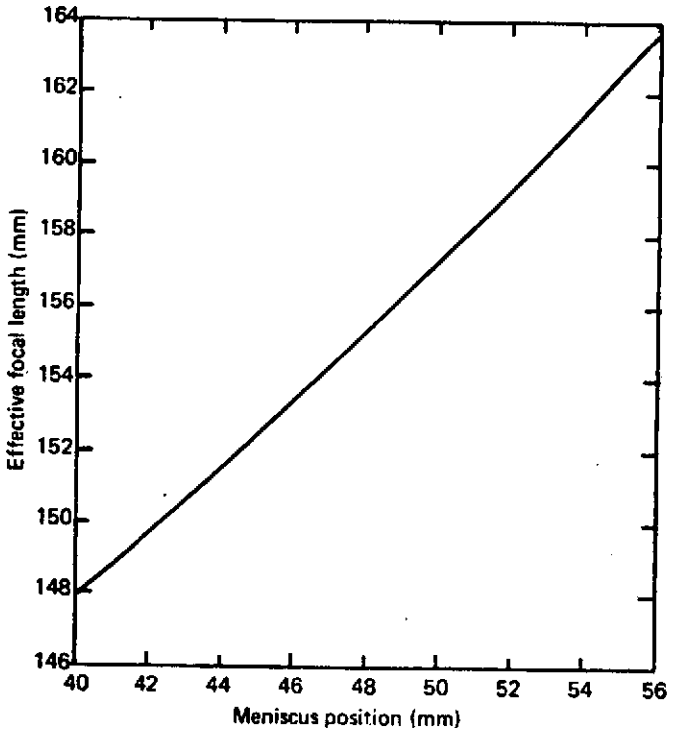

Fig. 4. Aberration generator effective focal length (GEFL) as a function of meniscus position.

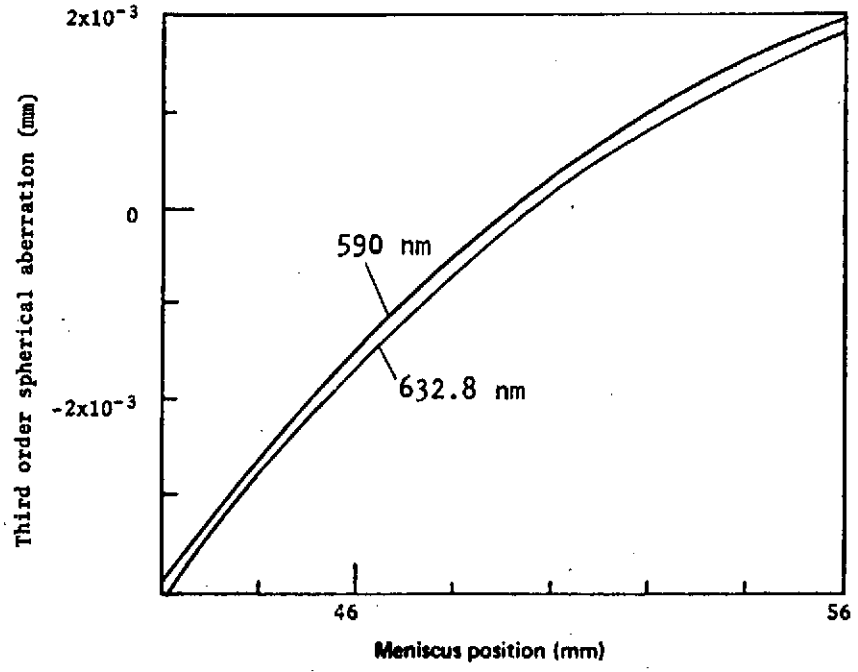

Fig. 5. Third-order spherical aberration as a function of meniscus position

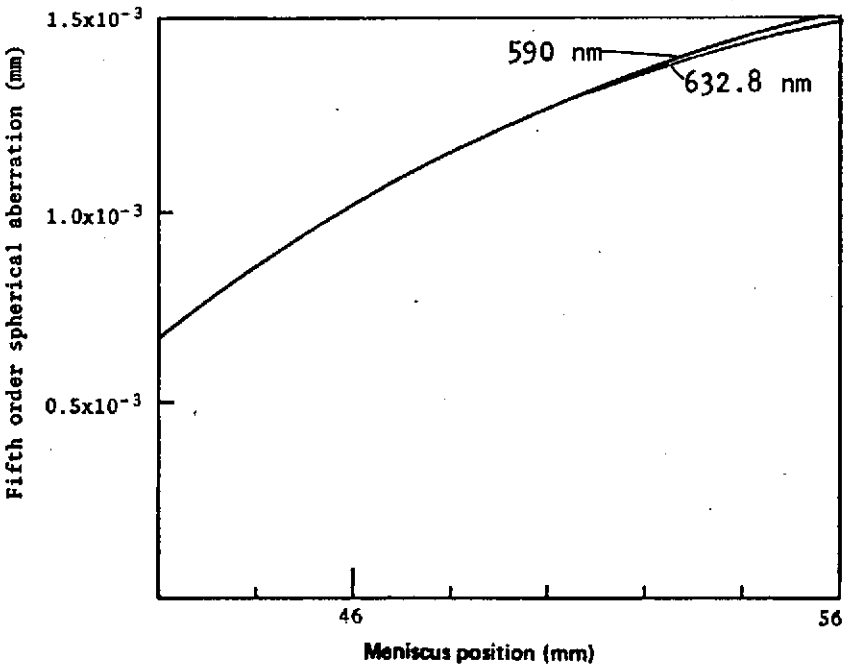

Fig. 6. Fifth-order spherical aberration as a function of meniscus position.

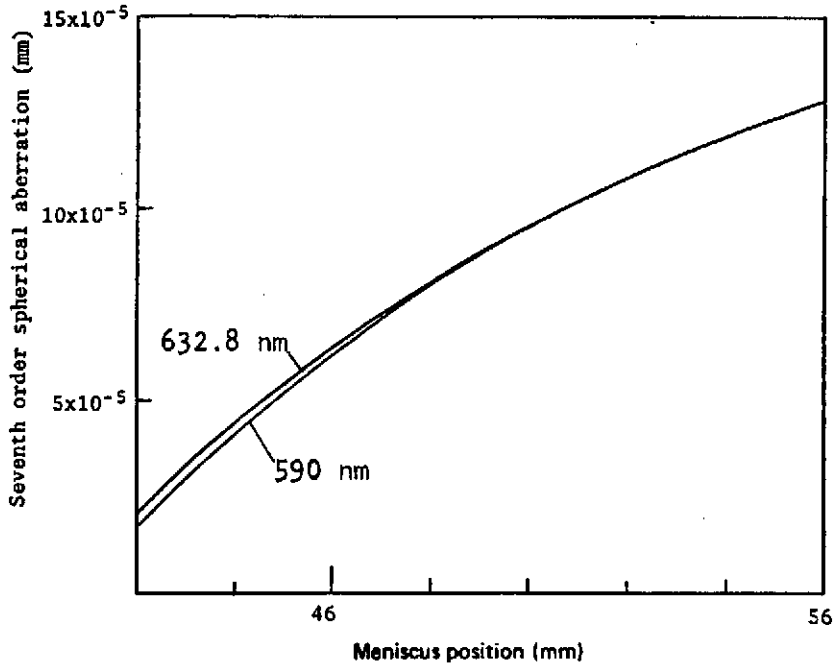

Fig. 7. Seventh-order spherical aberration as a function of meniscus position.

iv. Overall optical path difference

The coefficients for the parameters below were obtained by ray tracing at various positions of the meniscus. In order to obtain analytical expressions for BFP, GEFL, SA3, SA5, and SA7 each of the curves was fitted to a polynomial expression that resulted in the following equations:

$$SA3 = (2.4683572 \times 10^{-7})x^3 - (5.4403322 \times 10^{-5})x^2 + (3.9624001 \times 10^{-3})x - 0.092684628$$

$$SA5 = (5.4406814 \times 10^{-8})x^3 - (1.0583634 \times 10^{-5})x^2 + (7.0274608 \times 10^{-4})x - 0.014209098$$

$$SA7 = (7.9180215 \times 10^{-9})x^3 - (1.4642964 \times 10^{-6})x^2 + (9.3790299 \times 10^{-5})x - (1.9275608 \times 10^{-3})$$

$$BFP = -(3.9558132 \times 10^{-5})x^3 - (8.0375794 \times 10^{-4})x^2 + (0.30452283)x + 108.12638$$

$$GEFL = (3.8922327 \times 10^{-5})x^3 + (3.9824714 \times 10^{-4})x^2 + (0.65624124)x + 118.61591$$

where x refers to the spacing (in millimeters) between the plane-parallel plates and the meniscus element. It is found by adding the reading on the dial indicator to a constant C. This constant was determined experimentally in the calibration of the generator so as to compensate for residual manufacturing errors. In using the full generator aperture, as was done in the Hartmann and shearing tests, the nominal calibration reference was 46.2 mm. For the Zernike test the generator had to be stopped down, and the new calibration reference was 49.2 mm. These corresponded to C values of 36.2 mm and 39.2 mm, respectively.

Using these equations and the expressions for the OPD contribution of the various components of the aberration generator we can generate an overall expression for OPD introduced by the total aberration generator as follows:

$$OPD_{Total} = OPD_{Pinhole} + OPD_{Doublet} + OPD_{Plates} + OPD_{Meniscus} + OPD_{Relay}$$

where the optical path difference for the total aberration generator OPD_{Total} is equal to the sum of the OPD's of the individual components of the system.

The optical path difference contributed by lateral shifts in the pinhole position $OPD_{Pinhole}$ has the effect of tilting the wavefront. This is expressed as

$$OPD_{Pinhole} = -\frac{h}{R}\beta r\cos(\phi-\alpha) = -\frac{12.7}{R}\beta r\cos(\phi-\alpha)$$

where h is the radius of the entrance pupil, R is the focal length of the aberration generator, β is the lateral distance from the pinhole to the axial position, r is the lateral distance from the optical axis (expressed as a fraction of the pupil radius) to the point on the wavefront being evaluated, ϕ is the angular position of the point on the wavefront as measured from the vertical y axis, and α is the angular position of the pinhole as measured from the vertical y axis. The parameters β and α are determined by the readings of the micrometers that position the pinhole x-y movement stage. They are

$$\beta = \frac{\sqrt{x^2 + y^2}}{CLEFL} = \frac{\sqrt{(AX-AXO)^2 + (AY-AYO)^2}}{CLEFL}$$

$$\alpha = \arctan\frac{X}{Y} = \arctan\frac{AX-AXO}{AY-AYO}$$

where CLEFL is the focal length of the collimating lens, AX and AY are the readings on the micrometers for the X and Y axes, respectively, and AXO and AYO are the positions of the micrometers when the pinhole is

located on the optical axis. The parameters r and ϕ are determined by the readings of the micrometers on the x-y stage that positions the sampling aperture. The measurements made for r are divided by the radius h' of the pupil in the plane of the sampling aperture

$$h' = \frac{(SEFL)(R1EFL)}{(GEFL)(R2EFL)} h$$

where SEFL is the focal length of the sampling lens (this lens recollimates the light from the second relay lens as shown in Fig. 1), R1EFL and R2EFL are the focal lengths of the first and second relay lenses, respectively, and GEFL is the focal length of the aberration generator as determined above. Then,

$$r = \frac{1}{h'} \sqrt{x^2 + y^2} = \frac{1}{h'} \sqrt{(PX-PXO)^2 + (PY-PYO)^2}$$

$$\phi = \arctan \frac{x}{y} = \arctan \frac{PX-PXO}{PY-PYO},$$

where PX and PY are the readings of the micrometers that position the sampling aperture and PXO and PYO are the readings when the sampling aperture is centered about the optical axis.

The optical path difference contributed by the tilt of the doublet $OPD_{Doublet}$ is expressed by

$$OPD_{Doublet} = -\tfrac{1}{2}(CMA3)r^3U\cos\theta$$

$$= -\tfrac{1}{2}(CMA3)r^3(U_x\cos\phi + U_y\sin\phi)$$

$$= -\tfrac{1}{2}(CMA3)r^3\left(\frac{1}{0.040}\right)\{(GXO-GX)\cos\phi + (GY-GYO)\sin\phi\}$$

where CMA3 is the amount of coma introduced by tilting the doublet 1.5°, U is the angle of tilt from the optical axis as a fraction of the maximum angle of 1.5°, and θ is the angular position of the point being sampled on the wavefront as it relates to the direction in which the coma is being introduced. U_x and U_y are the x- and y-axis components of the angle of the doublet and are measured by GX and GY as the readings on the micrometers of the orientation device. GXO and GYO are the micrometer readings when there is no tilt in the doublet. The 0.049 factor is the micrometer movement for a tilt of 1.5° and gives the angle as a fraction of the angle for which CMA3 was determined.

The optical path difference contributed by the tilting and rotating of the plane-parallel plates OPD_{Plates} is expressed by

$$OPD_{Plates} = -\tfrac{1}{2}(AST3)\omega^2 r^2 \cos^2\theta'$$

$$= -\tfrac{1}{2}(AST3)\left\{\frac{2(BZ-BZO)}{15}\right\}^2 r^2 \cos^2[\phi - (RZ-RZO)],$$

where AST3 is the amount of astigmatism introduced when the plates are tilted at an angle of 15° from their position normal to the optical axis, ω is the fraction of the 15° that they are actually tilted, and θ' is the angular position of the point being sampled on the wavefront (as it relates to the direction in which the astigmatism is being introduced) and is equal to the difference between ϕ and the angle from the vertical y axis of the coordinate system in which the plates are tilted. BZ is the reading on the tilt dial indicator showing the tilt, and BZO is the reading when the plates are both perpendicular to the optical

axis. The difference is multiplied by two because each unit division on the dial indicator is equal to 2° and then is divided by 15 to show the angle as a fraction of the angle for which AST3 was determined. RZ is the reading on the rotation indicator, and RZO is the reading when sagittal astigmatism is introduced in the direction of the y axis.

The optical path difference contributed by the longitudinal movement of the meniscus lens $OPD_{Meniscus}$ is represented by

$$OPD_{Meniscus} = -\frac{h^2}{2Q^2}\delta_z r^2 - \frac{1}{8}(SA3)r^4 - \frac{1}{12}(SA5)r^6 - \frac{1}{16}(SA7)r^8$$

$$= -\frac{(12.7)^2}{2(GEFL)^2}(BFP-BFPO)r^2 - \frac{1}{8}(SA3)r^4$$

$$- \frac{1}{12}(SA5)r^6 - \frac{1}{16}(SA7)r^8,$$

where δ_z is the change in focal position from the paraxial spherical aberration condition position with change of the meniscus lens position, and Q is the focal length of the aberration generator. BFP is the back focal position of the star image, and BFPO is the back focal position for minimum spherical aberration. SA3, SA5, SA7, GEFL, and BFP are defined in detail above.

The optical path difference contributed by the movement of the first relay lens OPD_{Relay} is expressed by

$$OPD_{Relay} = -\frac{h^2}{2Q^2}\delta_R r^2 = -\frac{(12.7)^2}{2(GEFL)^2}(DZO-DZ)r^2,$$

where δ_R is the movement of the first relay lens. DZ is the reading of

the dial gauge for the position of the relay lens, and DZO is the lens position when its focal point coincides with the focal point of the aberration generator with the meniscus lens positioned to give minimum spherical aberration.

3. Mechanical Components

The air-spaced doublet in the aberration generator is counted in a cell that threads into a Lansing Research Model 10.203 angular orientation device with linear micrometer adjustments. Each 0.0001 in. division of linear motion of the micrometers corresponds to a 13.5 arc second rotation of the lens. The cell is threaded into the orientation device until the rear nodal point of the lens coincides with the intersection of the x- and y-gimbal tilt axes. The direction and amount of coma introduced are calculated from the angle at which the doublet is tilted from the system optical axis.

The two plane-parallel plates are mounted into metal plates on individual axes parallel to one another. A toothed gear on each plate meshes with the gear on the other plate. Since both gears are of equal size, a tilt of one plate will cause an equal and opposite tilt of the other plate. One of these plates is geared to a dial indicator. Each 0.02 division on the dial is equivalent to a 2.4 minute tilt of each plate. This whole assembly is bearing-mounted so that it will rotate about the system optical axis. The bearing rotation is gear controlled. These gears also operate a digit counter where a one-digit change corresponds to 1^{o} of rotation about the optical axis. The amount of

astigmatism is computed from the angle difference between the two plates, and the direction is determined by the tilt orientation.

The thick meniscus lens is mounted into a cell that is attached to a micrometer slide. Initially the lens is positioned so as to give minimum spherical aberration for the system. The lens can then be moved toward or away from the air-spaced doublet and parallel plates to put various amounts of positive or negative spherical aberration into the system. The travel of the lens is measured with a dial gauge having a 25-mm travel and reading to 0.01 mm. The amount of spherical aberration is calculated from the distance between the adjusted position of the meniscus lens and its nominal position when the system has minimum spherical aberration.

The two cemented doublets for the relay optics are mounted in individual cells. The cell for the first lens is mounted on a micrometer slide and is positioned so that its focal point coincides with the image formed by the aberration generator. As the image point moves along the optical axis when the meniscus lens is moved, the first relay lens is moved on its micrometer slide so as to keep its focal point and the image in coincidence. This keeps the beam coming from this lens collimated. The collimated beam is then brought to a focus by the second lens, an f/12 telescope objective. A photograph of the complete assembly appears in Fig. 8.

4. Aberration Generator Systematic Error and Calibration

All radii, indices of refraction, thicknesses, and focal lengths

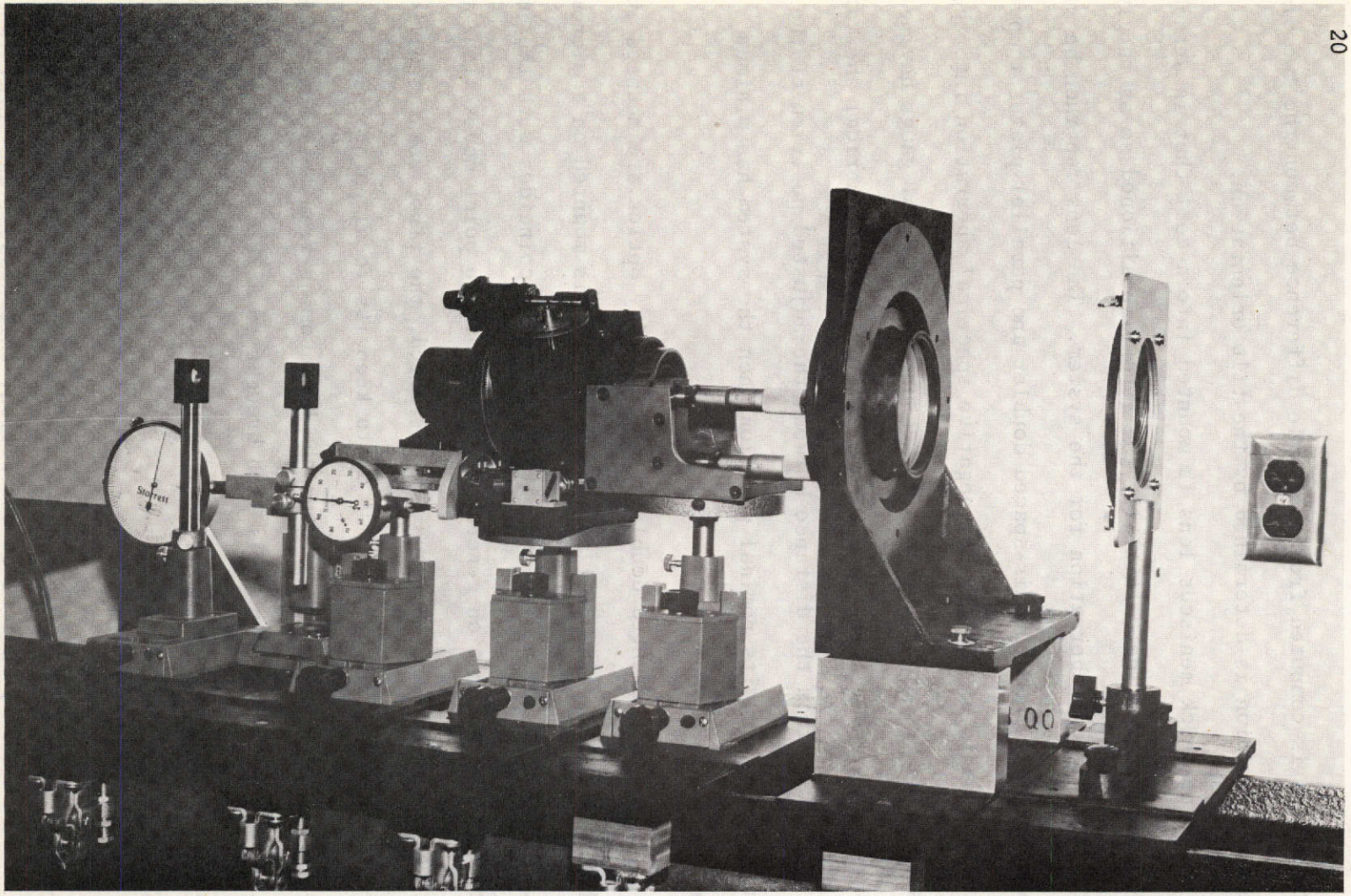

Fig. 8. Aberration generator and relay system.

of the various elements in the generator were either measured or known, so the calculated coefficients for aberration prediction do not vary from nominal values sufficiently to affect calculated OPD's by more than 2% to 3%.

There were two major sources of systematic errors. The first was associated with the calibration error of the nominal zero position setting of the meniscus element. The other was the error associated with micrometer adjustments for the various components.

a. Meniscus Position Calibration and Associated Systematic Error

The following is a description of the procedure used to determine the nominal zero position of the meniscus element.

After all components of the generator were aligned, a visual inspection of the star image was made and the meniscus element was set so as to compensate for residual spherical aberration in the doublet and parallel plates and for surface fabrication irregularities. The actual numerical value of the nominal zero aberration reference position had to be determined. This was necessary in order to use the non-linear analytical expressions for spherical aberration and image shift (BFP) to calculate the OPD for a change in meniscus position. This was accomplished by using procedures for data collection associated with the Hartmann test (Chapter 3).

First, the meniscus element was moved forward and backward 2 mm from the nominal zero setting. Ray deviation measurements were taken using the Hartmann test at pupil locations near the optical axis. From

these measurements, defocus calculations were performed to determine the change in BFP for the forward 2-mm movement and backward 2-mm movement. By comparison of the changes in BFP (see Fig. 3) for forward and backward movements, it was concluded that the nominal zero setting of the meniscus was in the vicinity of 46 mm. To determine a more precise figure the meniscus element was displaced 1 mm from the nominal zero setting, and several ray displacement measurements were made at position 9 in the pupil (Chapter 3). These ray displacement values were then compared to values predicted for a 1-mm movement using the design parameters of the generator. This was done using different values of the nominal zero position in the vicinity of 46 mm. The measured displacements agreed most closely with the predicted displacements for a nominal zero value of 46.2 mm.

i. Systematic error

Since the variations of the measured ray displacement values were within a ±1 μm range, the nominal zero position could be specified as 46.2 mm ± 0.1 mm at worst. For a 1-mm movement of the meniscus, this uncertainty corresponds to a ± λ/130 uncertainty in the predicted value at full f/6 aperture and ± λ/200 at position 9.

b. Systematic Errors Associated with Micrometer Adjustments in the Generator

i. Coma (doublet)

The tilt micrometer could be adjusted to ± 0.0001 in. This

corresponds to a systematic error of ± λ/200 at the full f/6 aperture.

ii. Astigmatism

The dial adjustment could be set to ± 0.01 division = ± 0.02°. Since astigmatism varied quadratically as a function of plate tilt, the systematic error would vary linearly with the amount. Thus the systematic error was ± W_{22}/25 at the full f/6 aperture, where W_{22} is the amount of astigmatism in waves (i.e. for W_{22} = λ/10 the systematic error is ± λ/250).

iii. Defocus (relay)

The relay lens could be positioned to ± 0.00005 in. The associated systematic error was ± λ/130 at the full f/6 aperture.

CHAPTER 3

THE COARSE RANGE SENSOR

1. General

Several types of coarse range (geometrical) optical tests were considered. Three of the most common are the Foucault knife-edge test, the wire test, and the Ronchi test. Effectively, in each of these tests, a particular type of obscuration mask (knife edge, wire, multiple wire) is placed in the vicinity of the focal plane. We can then obtain ray slope information (and, by integration, wavefront data) by noting the mask location and parameters. However, these tests suffer from a common flaw: the test mask must be rotated for nonsymmetric aberrations like astigmatism and coma. Also, the pupil must be scanned to obtain meaningful error measurements. Consequently, the Hartmann test was chosen because it is as sensitive as the above-mentioned tests, but it does not require mask rotation and control. It also allows us to monitor any point on the pupil that we wish.

2. The Hartmann Test

a. General Arrangement

In the classical application of the Hartmann test a mask of precisely located holes is placed in the exit pupil of the optical system. Each hole lets through a particular ray that converges toward focus. Two photographic plates are exposed, one in front of focus and

the other behind. By knowing the distance between the plates and by reading out on a comparator the positions of the rays on the plates, a slope can be determined for each ray in the pupil.

This classical form of the Hartmann test is obviously not suited to remote testing. However, as illustrated in Fig. 9, only a simple modification is required. Plane A indicates the optical system exit pupil. Lens B is positioned so that its rear focal point lies at the system focus. At location C we have the reimaged optical system pupil in collimated light space. In this relayed space we can sample a particular pupil location conveniently by means of a movable aperture. Any departure from a perfect system wavefront will show up in the sampled ray as a small angular deviation from collimated light. The slope error in the system exit pupil at this corresponding point can be found easily by multiplying the measured angular departure by the ratio of the relay lens focal length to the system focal length. This technique allows us to sample any pupil location we so desire and to use the full energy spectrum available. We also have an increased measurement

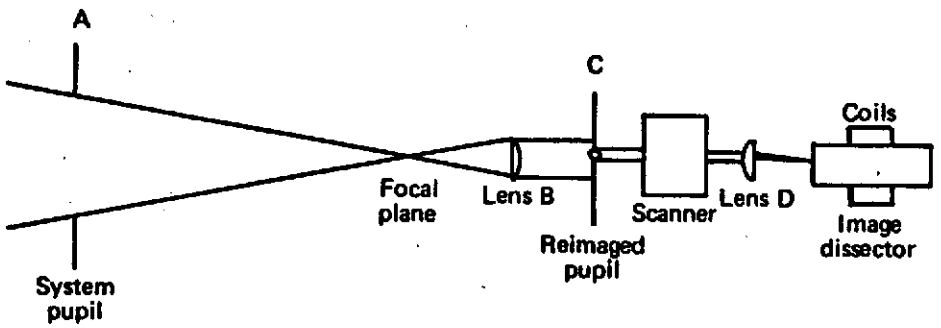

Fig. 9. Hartmann sensor configuration.

sensitivity equal to the ratio of the system focal length to the relay lens focal length.

i. Automatic readout

We are now left to read out the angular deviations of these various rays. A suggested automatic technique involves the use of an image dissector tube of the star tracker variety. The arrangement is indicated in Fig. 9. The second lens, D, focuses a particular ray bundle, which is sampled at its rear focal plane, at some position off axis that depends on the slope error and the sampled pupil position. The image dissector measures this off-axis location. This position, divided by the focal length of lens D, is the magnified slope error at the pupil position.

The dissector tube consists of a photocathode that has been deposited within a transparent window. An electrostatic focusing system refocuses the electron image produced by the sampled ray bundle within or in the vicinity of a metallic plate containing a circular aperture in its center. Those electrons getting through the aperture produce a current. An orthogonal set of magnetic coils is phased 90° apart with equal deflection amplitude thus producing a circular scan of the electron image about the metallic circular aperture. Synchronous amplification of the resulting signal is carried out at approximately the scanning frequency. If the ray image is perfectly centered in its scan about the circular disk, then there is no synchronous error signal produced. However, if the ray bundle is displaced, an ac error signal is produced

with some particular phasing depending upon the ray position. From this we extract an x,y-axis error signal that can then be applied as an offset signal to the deflection coils until the error signals are nulled. Knowing the calibration on the offset deflection signal, we obtain the ray position.

ii. Simulated automatic readout

This scheme has been simulated in the laboratory with the use of a Risley prism scanner, a movable pinhole, and a standard photomultiplier tube (PMT). This is illustrated in Fig. 10.

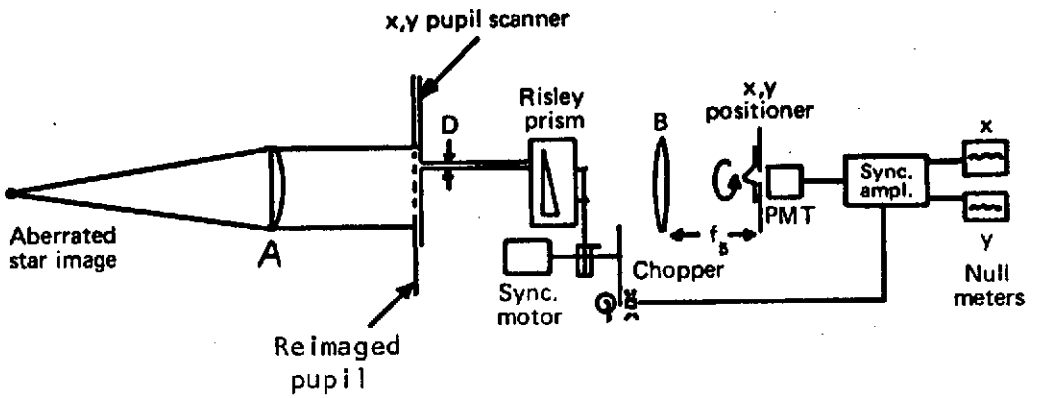

Fig. 10. Laboratory Hartmann test simulator.

Lens B focuses a particular ray bundle on or near the pinhole. This diffraction image is spun about the pinhole by a Risley prism whose orientation has been adjusted to give a circular spin diameter equal to the pinhole diameter. A mechanical chopper driven by the prism motor at 30 Hz gives a reference signal phased on the x axis. Behind the pinhole is an EMR 9858 PMT. As the image is moved around the pinhole, any offset produces a 30 Hz variation in the PMT output current. As

illustrated in Fig. 10 this 30-Hz signal is preamplified and converted into a voltage signal. The voltage signal is then fed into a synchronous amplifier that first filters and amplifies the incoming signal and then splits the signal into two identical components 90° apart in phase. Each component is connected to the input of a phase-sensitive demodulator where the signal is mixed with the reference voltage signal to produce sum and difference currents. A filter at the output of the phase-sensitive demodulator rejects the high-frequency (sum) frequencies and passes the zero or dc difference component corresponding to the component of the signal spectrum at the reference frequency. This zero-frequency current is the error signal output. We have two of these: one in phase that indicates the x-axis displacement, and a quadrature signal that indicates the y-axis displacement. By moving the collection pinhole we can first zero out the x-error and then the y-error signals, read the micrometers, and calculate our wavefront slope errors. Figure 11 is a photograph of the Hartmann test wavefront simulator being evaluated by the aberrated telescope.

b. Theoretical Discussion

We have investigated several theoretical problems concerning the Hartmann test. These include an examination of the effect of sampling aperture size in the exit pupil on measurement of primary aberrations and detection sensitivity. They also include the basis for determining the optimum size scanning pinhole for subsequent S/N ratio calculations.

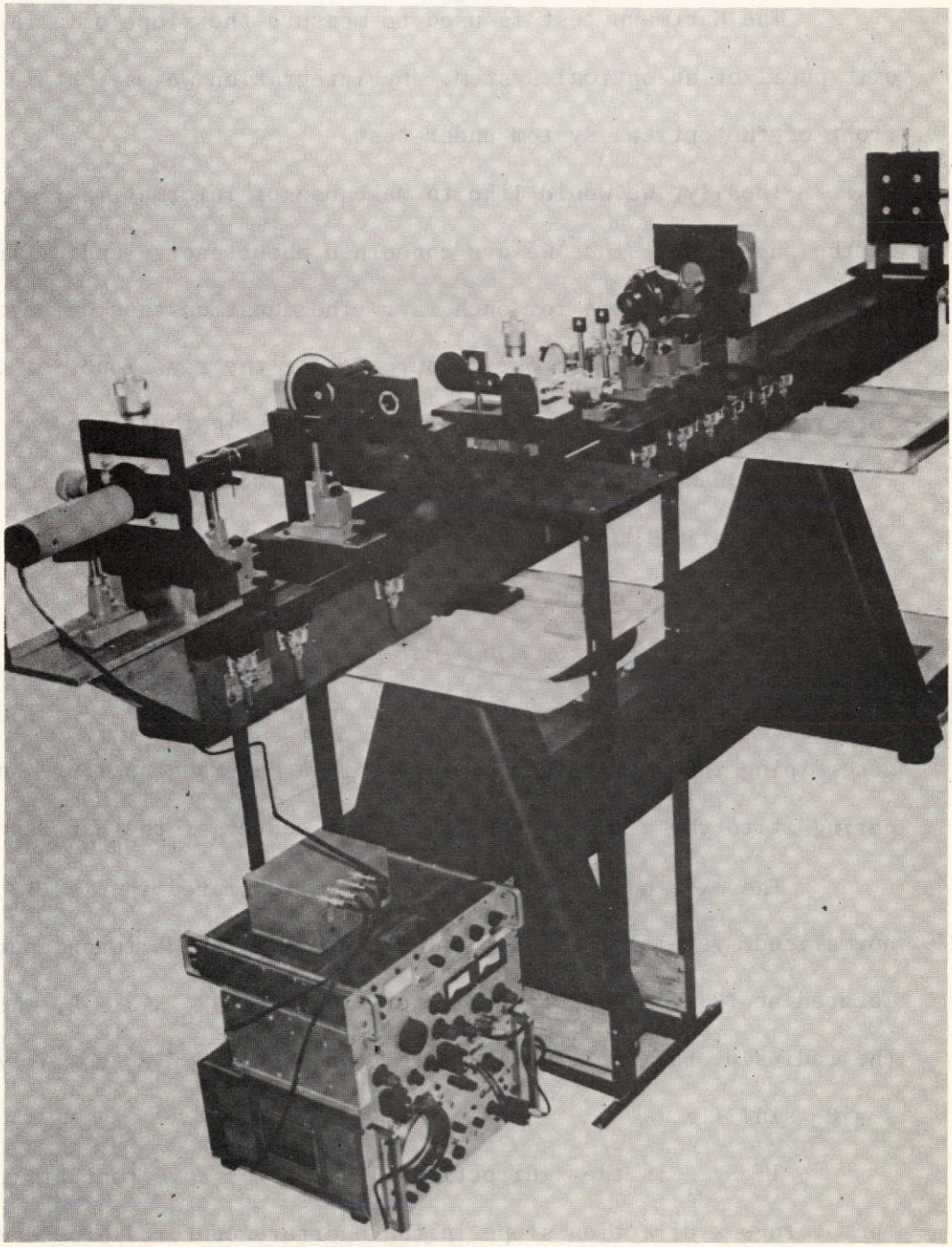

Fig. 11. Hartmann test simulator and aberrated telescope wavefront simulator.

i. Effects of sampling aperture on third-order aberrations

The Hartmann test is used to measure the slope of a ray in the exit pupil of an optical system. By integration we may obtain the wavefront of the optical system under test.

Ideally, we would like to make use of information from one point in the pupil, but since we are concerned about energy and diffraction we need a finite aperture for each ray. The question then arises: How does the aperture size affect our measurement of the ray slope, since we are integrating over a finite area of wavefront? In the following discussion we develop quantitatively a wavefront error measurement expression in terms of relative Hartmann aperture size and aberration type. Diffraction effects are considered in ii.

The *assumption is made that we have a measuring scheme that will locate the centroid of the image of the Hartmann aperture.* Thus we are determining the average slope of rays in a Hartmann aperture and comparing it to the slope of the ray at the center of the Hartmann aperture.

The exit pupil of the system is illustrated in Fig. 12. In a normalized system $X^2 + Y^2 \leq 1$. The center of the Hartmann aperture is located at (R_c, Φ). Our analysis here restricts $R_c \leq 1 - D$, where D is the radius of the Hartmann aperture. Obviously $Y = R_c \cos\Phi + y$; $X = R_c \sin\Phi + x$.

If S_{xXY} is the x-direction slope of the wavefront at X, Y, then the average x-direction slope in the aperture centered around R_c, Φ is

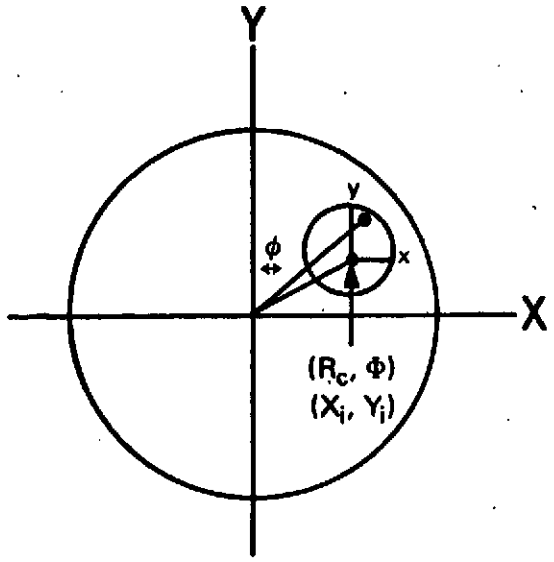

Fig. 12. Telescope system exit pupil.

$$\overline{S}_{xX_iY_i} = \frac{\int_{-D}^{+D} \int_{-(D^2-x^2)^{\frac{1}{2}}}^{(D^2-x^2)^{\frac{1}{2}}} S_{xXY}\,dxdy}{\pi D^2} .$$

Likewise the average slope in the y-direction is

$$\overline{S}_{yX_iY_i} = \frac{\int_{-D}^{+D} \int_{-(D^2-x^2)^{\frac{1}{2}}}^{(D^2-x^2)^{\frac{1}{2}}} S_{yXY}\,dxdy}{\pi D^2} .$$

Now let us consider several aberration types and their measurement errors introduced in the Hartmann test.

iii. Aberrations and measurement errors

Defocus

$$W = W_{20}(X^2 + Y^2)$$

$$S_{xXY} = \frac{\partial W}{\partial X} = 2W_{20}X$$

$$S_{yXY} = \frac{\partial W}{\partial Y} = 2W_{20}Y.$$

In our small displaced aperture D,

$$W = W_{20}(R_c^2 + x^2 + y^2 + 2R_c\,[x \sin\Phi + y \cos\Phi])$$

$$S_{xXY} = \frac{\partial W}{\partial x} = W_{20}(2x + 2R_c \sin\Phi)$$

$$\bar{S}_{xX_iY_i} = \frac{\iint S_{xXY}}{\pi D^2} = \frac{\iint (2x + 2R_c \sin\Phi)dxdy}{\pi D^2}.$$

The first term integrates to zero and we are left with

$$\bar{S}_{xX_iY_i} = 2W_{20}R_c \sin\Phi = 2W_{20}X_i$$

or

$$\bar{S}_{xX_iY_i} = S_{xX_iY_i}$$

or the average x-slope in the aperture D is equal to the actual x-slope at the center coordinate of D for the defocus aberration. Likewise,

$$\bar{S}_{yX_iY_i} = S_{yX_iY_i}.$$

Thus defocus in the absence of other aberrations causes no shift in the Hartmann image centroid.

Tilt

The wavefront aberration for tilt is $W = W_{y11}Y + W_{x11}X$ where W_{y11} is a tilt of wavefront in the Y-direction

$$S_{xX_iY_i} = \frac{\partial W}{\partial X} = W_{x11}(\text{x-slope at } X_iY_i)$$

$$W = W_{y11}(R_c \cos\phi + y) + W_{x11}(R_c \sin\phi + x)$$

$$S_{x_{XY}} = \frac{\partial W}{\partial X} = W_{x11}$$

$$\bar{S}_{x_{XY}} = \frac{\iint W_{x11}\,dxdy}{\pi D^2} = W_{x11}.$$

Thus,

$$\bar{S}_{x_{XY}} = S_{x_{X_iY_i}}.$$

We see that in the absence of other aberrations a tilt causes no shift in the Hartmann image centroid.

Astigmatism

The wavefront aberration for astigmatism is

$$W = W_{22}\rho^2 \cos\phi^2 = W_{22}Y^2$$

$$S_{y_{X_i Y_i}} = 2W_{22}Y_i$$

$$W = W_{22}(y^2 + R_c^2 \cos\Phi + 2yR_c \cos\Phi)$$

$$S_{y_{X_i Y}} = \frac{\partial W}{\partial y} = 2W_{22}R_c \cos\Phi = 2W_{22}Y_i + 2yW_{22} + 2yW_{22}$$

$$\bar{S}_{y_{XY}} = \frac{\int\int (2W_{22}Y_i + 2yW_{22})dxdy}{\pi D^2} .$$

The second integral is zero. Thus,

$$\bar{S}_{y_{XY}} = 2W_{22}Y_i = S_{y_{X_i Y_i}} .$$

Again astigmatism does not cause a centroid shift.

Thus far with defocus, tilt, and astigmatism we have seen that the Hartmann centroid is not shifted due to the sampling aperture size. We will see that this is not the case for third-order spherical aberration and coma. That is, the finite aperture in the Hartmann test introduces a certain error of predictable form and magnitude depending on the relative Hartmann aperture size.

Spherical aberration

$$W = W_{40}(X^2 + Y^2)^2$$

$$S_{x_{X_i Y_i}} = 4W_{40}X_i R_c^2$$

$$S_{y_{X_i Y_i}} = 4W_{40} Y_i R_c^2.$$

In the Hartmann aperture

$$W = W_{40}(R_c^2 + y^2 + x^2 + 2R_c[x \sin\Phi + y \cos\Phi])^2$$

$$S_{x_{XY}} = \frac{\partial W}{\partial x} = 2W_{40}(R_c^2 + y^2 + x^2 + 2R_c [x \sin\Phi + y \cos\Phi]) \cdot (2x + 2R_c \sin\Phi)$$

$$= 4W_{40}[\underset{\checkmark}{xR_c^2} + \underset{\checkmark}{xy^2} + \underset{\checkmark}{x^3} + 2X_i x^2 + \underset{\checkmark}{2Y_i xy}]$$

$$+ 4X_i W_{40}[R_c^2 + (x^2 + y^2) + 2X_i x + 2Y_i y].$$

All odd functions integrate to zero as indicated by the ✓. We are left with

$$\bar{S}_{x_{X_i Y_i}} = 8W_{40} X_i \frac{\iint x^2 dxdy}{\pi D^2} + 4X_i W_{40} R_c^2$$

$$+ 4X_i W_{40} \frac{\int_0^{2\pi} \int_0^D \rho^2 \rho d\rho d\theta}{\pi D^2}$$

$$\bar{S}_{x_{X_i Y_i}} = S_{x_{X_i Y_i}} + 2D^2 X_i W_{40} + W_{40} X_i D^2.$$

By symmetry

$$\bar{S}_{y_{X_iY_i}} = S_{y_{X_iY_i}} + 2D^2Y_iW_{40} + W_{40}Y_iD^2$$

$$W_{Measured} = \int_0^{X_M} \bar{S}_{x_{X_iY_i}} dX_i + \int_0^{Y_M} \bar{S}_{y_{X_iY_i}} dY_i$$

$$W_{Measured} = W_{40}(X_M^2 + Y_M^2)^2 + 3W_{40}[D^2] \cdot [X_M^2 + Y_M^2]$$

$$W_{Measured} = W_{40}R_M^4 + 3W_{40}D^2R_M^2.$$

We see that when we measure spherical aberration with a Hartmann array we get an additional term in our measurement, which takes the form of a focusing error with coefficient $3W_{40}D^2$. However, since we have obtained the functional form of the associated error we can now apply this knowledge to a correction term on our defocus measurement and thus compensate for the finite Hartmann aperture size.

Coma

$$W = W_{31}\rho^2 \cos\Phi = W_{31}(X^2 + Y^2)Y$$

$$S_{x_{X_iY_i}} = \frac{\partial W}{\partial X} = 2W_{31}X_iY_i$$

$$S_{y_{X_iY_i}} = \frac{\partial W}{\partial Y} = W_{31}(X_i^2 + Y_i^2) + 2W_{31}Y_i^2$$

$$S_{x_{XY}} = \frac{\partial W}{\partial x} = 2W_{31}(xy + xR_c \cos\Phi + yR_c \sin\Phi) + S_{x_{X_iY_i}}.$$

Since the first three terms integrate to zero

$$\bar{S}_{x_{XY}} = S_{x_{X_iY_i}}.$$

Thus there is no x-component of slope error. However,

$$S_{y_{XY}} = \frac{\partial W}{\partial y} = S_{y_{X_iY_i}} + W_{31}(\rho^2 + 2R_c x \sin\Phi + 3R_c y \cos\Phi)$$

$$+ 2W_{31}(y^2 + 2yR_c \cos\Phi).$$

Integrating we obtain

$$\bar{S}_{y_{XY}} = S_{y_{X_iY_i}} + W_{31}D^2.$$

Since

$$W_{Measured} = \int_0^{X_M} \bar{S}_{x_{XY}} + \int_0^{Y_M} \bar{S}_{y_{XY}} dY$$

$$W_{Measured} = W_{31}(X_M^2 + Y_M^2)Y_M + W_{31}Y_M D^2.$$

We thus see that in the case of coma, a finite size Hartmann aperture will introduce an error that takes the form of a tilt aberration. This information can be used as a correction on tilt measurement.

We see from the preceding discussion that if we are measuring the Hartmann centroid the only third-order aberrations that introduce errors are spherical aberration and coma, and that the amounts of error are extremely small. We could predict the amounts of error for these

aberration measurements by using the error formulas developed. We can also take advantage of our knowledge of the aberrational form of error to eliminate it. If we were monitoring an active system and were looking for changes, and we measured a change in spherical aberration we would also be able to predict the defocus type error that would be associated with it and thus not confuse it with an actual defocus change. The same argument holds for the coma and tilt error.

iii. Optimal signal recording geometry

In order to calculate the signal generated by the slightly off-center diffraction image of a sampled bundle of rays, we must know the nature of the diffraction pattern formed on the image dissector's face, the impulse response of the tube, and the dimensions of the collecting aperture within the tube. The convolution of these three quantities will give us the normalized amount of energy passing into the dissector for a given diffraction image collecting aperture displacement. From this convolution curve we can determine the change in signal current for a change in position of the diffraction pattern on the tube face due to a slope error. Thus we will be able to make signal predictions based upon star source characteristics, f/No. of sampled pupil area, tube scanning aperture sizes, and tube impulse response characteristics.

Referring to Fig. 10 let D be the sampling aperture size, f the lens focal length, and λ the average wavelength of the collimated light. The intensity distribution in the image dissector collecting plane for a unit amplitude disturbance is

$$I(r) = \frac{\pi^2 D^4}{16\lambda^2 f^2}\left[\frac{2J_1(\frac{\pi Dr}{\lambda f})}{(\frac{\pi Dr}{\lambda f})}\right]^2 .$$

The impulse response of the dissector tube is approximately Gaussian and can be written as

$$G(r) = \frac{1}{2\sigma^2} e^{-\frac{\pi r^2}{2\sigma^2}} .$$

Here σ is the Gaussian width of the response. The collecting aperture can be represented by $H(r) = \text{circ}(r/\ell/2)$, which is a function such that

$$H(r) = 1 \qquad 0 \leq r \leq \frac{\ell}{2}$$

$$H(r) = 0 \qquad r > \frac{\ell}{2} .$$

The energy getting through the aperture for a displaced diffraction image is

$$L(r) = I(r)*G(r)*H(r),$$

where * is convolution, and r is the coordinate of the diffraction image.

Taking the Fourier transform (F)

$$FL(r) = FI(r) \cdot FG(r) \cdot FH(r)$$

where

$$F\left(I(r)\right) = \frac{D^2}{2}\left[\cos^{-1}\frac{S\lambda f}{D} - \frac{S\lambda f}{D}\left(1 - (\frac{S\lambda f}{D})^2\right)^{\frac{1}{2}}\right]$$

when

$$S \leq \frac{D}{\lambda f}$$

$$F\left(I(r)\right) = 0 \quad \text{when } S > \frac{D}{\lambda f}$$

$$FG(r) = e^{-\pi 2\sigma^2 S^2}$$

$$FH(r) = \left(\frac{\ell}{2}\right)^2 \frac{J_1(\pi \ell S)}{\frac{\ell S}{2}} .$$

Multiplying and taking the inverse transform yields

$$L(r) = \frac{\pi D^2 \ell}{2} \int_0^{\varepsilon} J_o(2\pi S r) J_1(\pi \ell S) e^{-2\pi\sigma^2 S^2} \left[\cos^{-1} \frac{S}{\varepsilon} - \frac{S}{\varepsilon} \left(1 - \left(\frac{S}{\varepsilon}\right)^2\right)^{\frac{1}{2}} \right] dS$$

where

$$\varepsilon = \frac{D}{\lambda f} .$$

We have evaluated this convolution for a series of possible ε parameters, in particular for an image dissector with a Gaussian width 2σ of 0.0035 in. and a collection aperture diameter ℓ of 0.020 in. These convolution data were then used to determine the peak-to-peak change in signal per micrometer of displacement, the change in signal per arc second deviation of the sampled ray, and a signal-to-noise figure of merit as shown in Table III. (Signal current is defined as the

peak-to-peak difference in the ac error signal generated by a ray displacement. Noise is determined by the total current generated by photons passing through the collection aperture ℓ.)

Table III

Hartmann test sensitivity values

$\varepsilon\lambda$	D (in.)	f (in.)	% signal change per arc second	S/N figure of merit
0.01	0.1	10	4.3	3.2
0.005	0.1	20	6.0	4.1
0.002	0.1	50	7.2	5
0.0015	0.1	66	8	5.2
0.001	0.1	100	10	4.1
0.0005	0.1	200	11	2.9

By plotting the S/N figure of merit versus focal length (Fig. 13) we see that we do have an optimum choice of focal length. However, the function is slowly varying over a large focal length range. The real optimization choice should be made considering the displacement stability of the coils, which can be relaxed at larger focal lengths, and residual mechanical vibration problems, which become worse at larger focal lengths. A good compromise for this tube is a focal length of about 50 in.

iv. Signal-to-noise ratio for image dissector readout

Assuming we have optimized according to the above argument, we can now calculate signal-to-noise ratios.

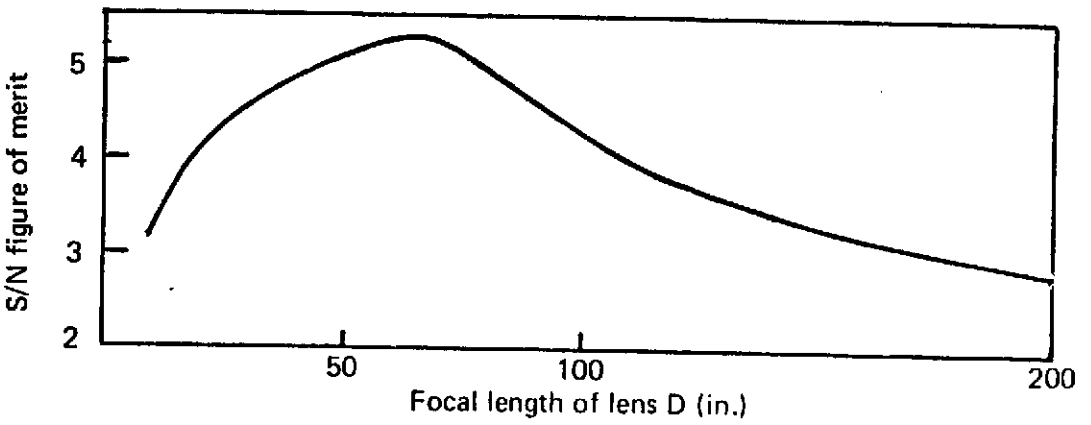

Fig. 13. S/N figure of merit as a function of focal length (image dissector tube).

For an extended red photocathode the total signal at the cathode, for a zero magnitude A_o star, assuming a 700 cm^2 sampling area collecting aperture, is $I = 0.50 \times 10^{-10}$ amps on the photocathode, which corresponds to the maximum photocathode current the tube can handle. Now assuming the parameter optimization as described in the last section

$$\text{(Shot Noise)} \quad I_N = \sqrt{2e\Delta f I}$$

$$I_N = \sqrt{0.5 \times 10^{-10}(2)(1.6 \times 10^{-19})(1)}$$

$$\simeq 4 \times 10^{-15} \text{ amps.}$$

From above, for a 1 arc-sec detection, the signal is approximately 0.06 of the total current on the photocathode, I

$$I_S = 30 \times 10^{-13} \text{ amp}$$

$$S/N = \frac{30 \times 10^{-13}}{4 \times 10^{-15}} \simeq 7.50 \times 10^{2} \simeq 750,$$

where dark current noise is approximately 10^{-16} amp for a 0.020-in. aperture.

We compute signal-to-noise ratios for other star magnitudes and summarize the results in Table IV.

Table IV

Best signal-to-noise ratios for detecting a 1 arc-sec slope change

Magnitude	S/N	Detection certainty (%)
0	750	100
2.5	250	100
5	60	100
7.5	6	100

The above analysis has not considered noise problems associated with deflection coils and field effects in image tubes.

v. Prediction of rms wavefront error σ_W from rms slope error σ_S

If the noise associated with each slope measurement is uncorrelated and has the same rms value at each measurement position, it can be shown that in one dimension

$$\sigma_W = L\sigma_S \frac{\left(\sum_{n=1}^{K} n\right)^{1/2}}{K^{3/2}} .$$

The rms wavefront error from all points in the pupil is σ_W, L is the pupil size, K is the number of points sampled, and σ_S is the rms slope error at each point.

If a dissector tube is used, such that the net rms position stability is at least 3 μm and the readout lens focal length f_E is approximately 60 in., then the value of $\sigma_S \simeq 2 \times 10^{-6}$ rad ≈ 0.4 arc sec. For a reimaged pupil radius of 12.5 mm where 10 points are sampled across this radius, the rms wavefront error would be expected to be

$$\sigma_W = 12.5\ (2 \times 10^6)(58/1000)^{\frac{1}{2}}$$

$$\simeq 0.006\ \mu m \simeq \lambda/100\ \text{rms}.$$

The rms wavefront error associated with using the dynamic Hartmann test readout aboard the LST can be predicted. The wavefront error would be determined to λ/100 rms by using a 12.5-mm reimaged pupil radius where 10 points are sampled across a pupil radius if (1) at least a fifth magnitude star is used, (2) deflection coil and tube stability are $\sigma_{\text{stability}} \simeq 2$ μm, and (3) short-term vibrations in the LST are less than $\sigma_W < 0.2$ arc sec, referred to the detector plane.

c. Experimental Evaluation of Hartmann Test

i. Experimental arrangement

The laboratory model of the Hartmann test (HT) figure sensor was designed and constructed using the simulated star tracker readout mechanism previously discussed. The laboratory figure sensor and the wavefront error simulator are pictured with the associated electronics

in Fig. 11. The entire bench arrangement was isolated from vibration from the laboratory floor by using a sand-filled optical bench that floated on inner tube pods. The Risley scanner was isolated from the bench by being positioned on a sturdyplatform that straddled the bench but did not come in contact with it. Further vibration isolation for the scanner was provided through the use of soft rubber mounts. The reference signal to the synchronous amplifier was produced by a laser beam incident on a photodiode, which was pulsed off and on by a chopper blade mounted on the Risley scanner motor.

All important parameters for the wavefront simulator are discussed in Chapter 2. The laboratory HT parameters are discussed below. For information clarity it is helpful to refer to Figs. 10 and 11.

Lens A was a high-quality telescope objective with a 220.3-mm focal length. The reimaged pupil of the aberration generator, with a measured diameter of 18.34 mm, was located approximately in the rear focal plane of lens A. A 2.5-mm-diameter sampling aperture was located in this plane and could be positioned while scanning the pupil with an accuracy of ± 0.0005 in. The Risley prism consisted of two matched 1-min-deviation prisms independently mounted in a scanner device such that their respective angular orientations could be adjusted and locked. This provided for the introduction of variable angular deviations, so that the diffraction pattern of the sampled ray bundle could be adjusted to scan around the perimeter of the detector pinhole. The readout lens B consisted of two elements, a 297.54-mm focal length telescope objective and a microscope objective. The conjugates of

the microscope objective were adjusted to give 5.0 X lateral magnification of the ray displacements in the rear focal plane of the telescope objective. This combination yielded a lens B effective focal length of 1487.7 mm. This arrangement had two advantages. First, it shortened the system. Second, the microscope objective was baffled and contained in a tube so that stray light on the PMT was minimized. The readout pinhole was placed at the effective rear focal plane of lens B and had a 0.3-mm radius. It was mounted on an X,Y stage and could be moved by micrometers with dial indicator readout to ± 0.25 μm.

ii. Experimental procedure

Preliminary parameter study

According to predictions made in the parameter study on the star tracker tube, the best S/N ratios could be obtained by using a readout lens B that caused the diffraction size of the sampled bundle to be slightly larger than the size of the detection pinhole aperture. Several experiments were performed using various collecting pinhole aperture sizes for the simulated star tracker readout. It was found that under laboratory conditions pinhole sizes from approximately one-half to two times the Airy disk size gave the best angular sensitivity, with variations in this range being indistinguishable. Thus the 0.3-mm radius pinhole was chosen to be used in conjunction with the lens B readout focal length of 1487.7 mm and sampling aperture of 1.25-mm radius. These parameters were also compatible with results of the star tracker simulation parameter optimization study.

Measurement stability of ray bundle deviation

It was found that the micrometer position for nulling out error signals for a particular sampled ray bundle had a short-term readout repeatability over the course of a few seconds of ± 1 μm to ± 2 μm and sometimes worse depending on the time of day and the particular day. Also, over the course of 15 minutes it was not unusual for the null position to drift ± 10 μm. The first problem was associated with residual random vibrations and the second with slower term variations in the index of the optical path due to air movement. To cope with the first problem experiments were run at those times when vibrations appeared to be near the low levels. Furthermore, several readings were taken at each point for averaging purposes. To deal with the slow drift problem, large portions of the optical path were enclosed, and laboratory air movement was kept to a minimum. Any residual drift was monitored so that ray deviation measurements could be compensated. This technique is described below.

Procedure for measurement of ray deviations

With the aberration generator micrometers and indicators set at the nominal zero aberration settings, the pupil sampling aperture was set centered on the optical axis. The detector pinhole was moved until the x and y axis error signals were nulled. The micrometer readings were recorded, and the sampling aperture was moved to another position where the micrometer readings for the null setting were again recorded. This procedure was repeated for preselected pupil locations so as to

scan the pupil diameter at equal increments out to the limiting point in the pupil, such that the sampling aperture remained completely filled (i.e., out to 7.94 mm in the pupil radius of 9.17 mm). To compensate for the slow drift of the star image, the central position of the reimaged pupil was chosen for referencing, and between each sampled pupil position ray deviation measurement, the reference ray position measurement was taken. The appropriate reference ray deviation position was then subtracted from each of the sampled position ray deviation measurements. This procedure produced a nominal zero aberration baseline of ray deviations measured at known pupil positions where the star source drift was eliminated.

Next a micrometer adjustment on the aberration generator was made to introduce a particular known amount of one of the low-order aberrations. The data collection procedure used for the baseline measurement was then repeated at the same preselected pupil locations. Again, star source drift was compensated by monitoring the central pupil reference ray position between each pupil position ray deviation measurement.

The aberration change ray deviation measurements were then subtracted from the baseline ray deviation measurements. This procedure resulted in a data set of aberration change ray deviation measurements at the preselected pupil locations.

These data appear in Figs. 14a, 15a, 16a, and 17a for different types and magnitudes of aberration change. Plotted with the measured ray deviation data are the theoretical predicted ray deviations based on the

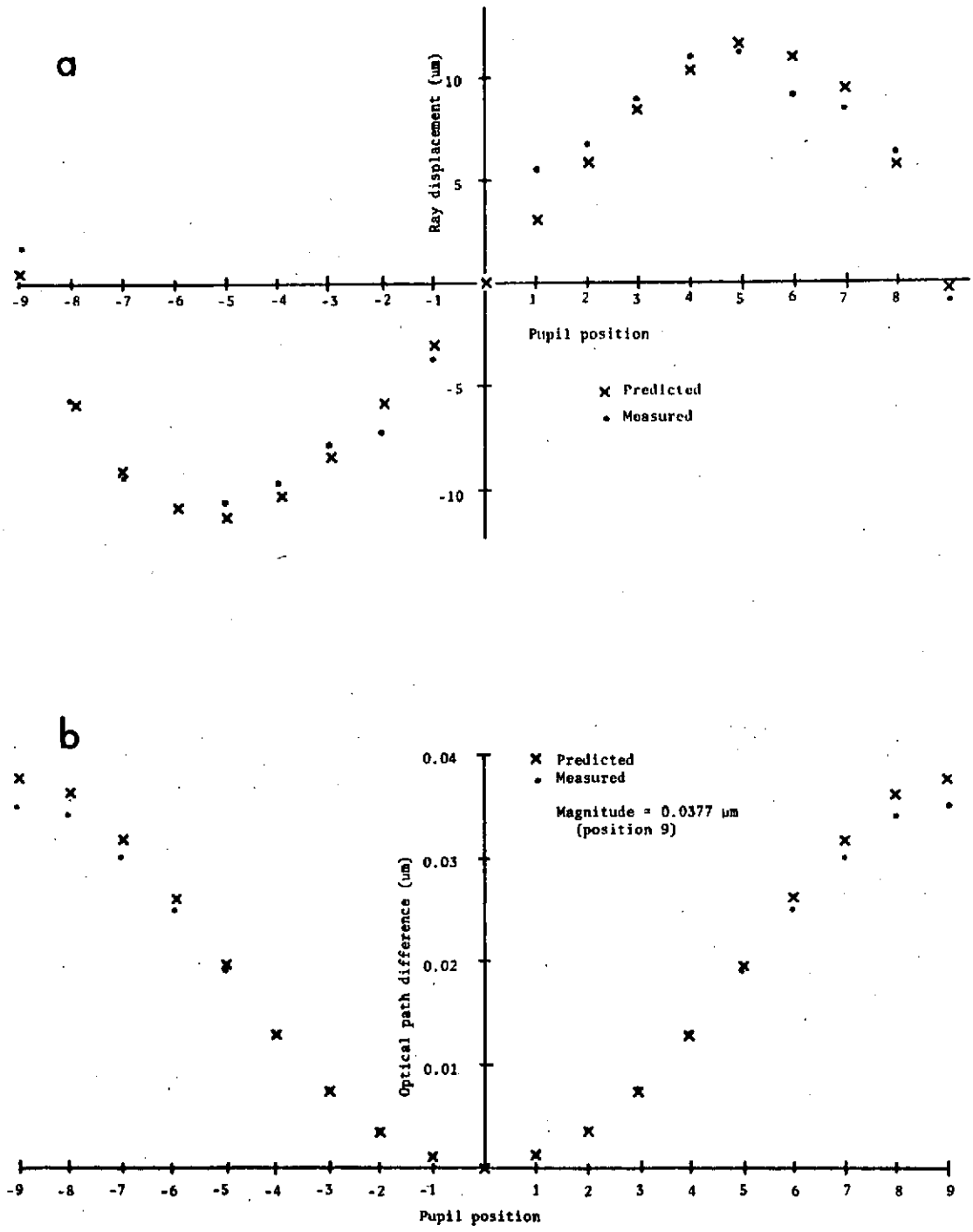

Fig. 14. Pupil position vs (a) ray displacement and (b) optical path difference for defocus plus spherical aberration.

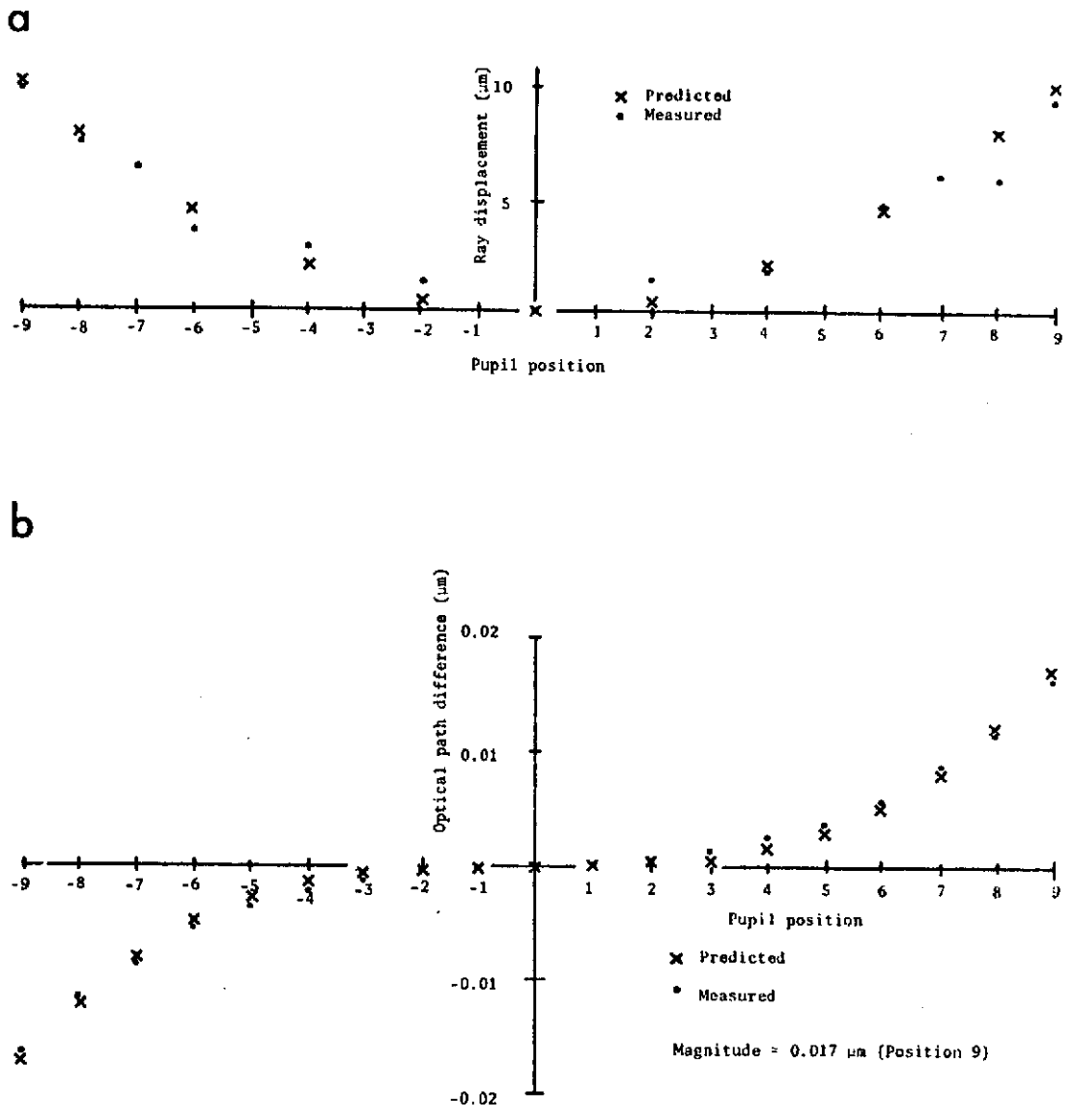

Fig. 15. Pupil position vs (a) ray displacement and (b) optical path difference for coma aberration at 0.017 μm magnitude.

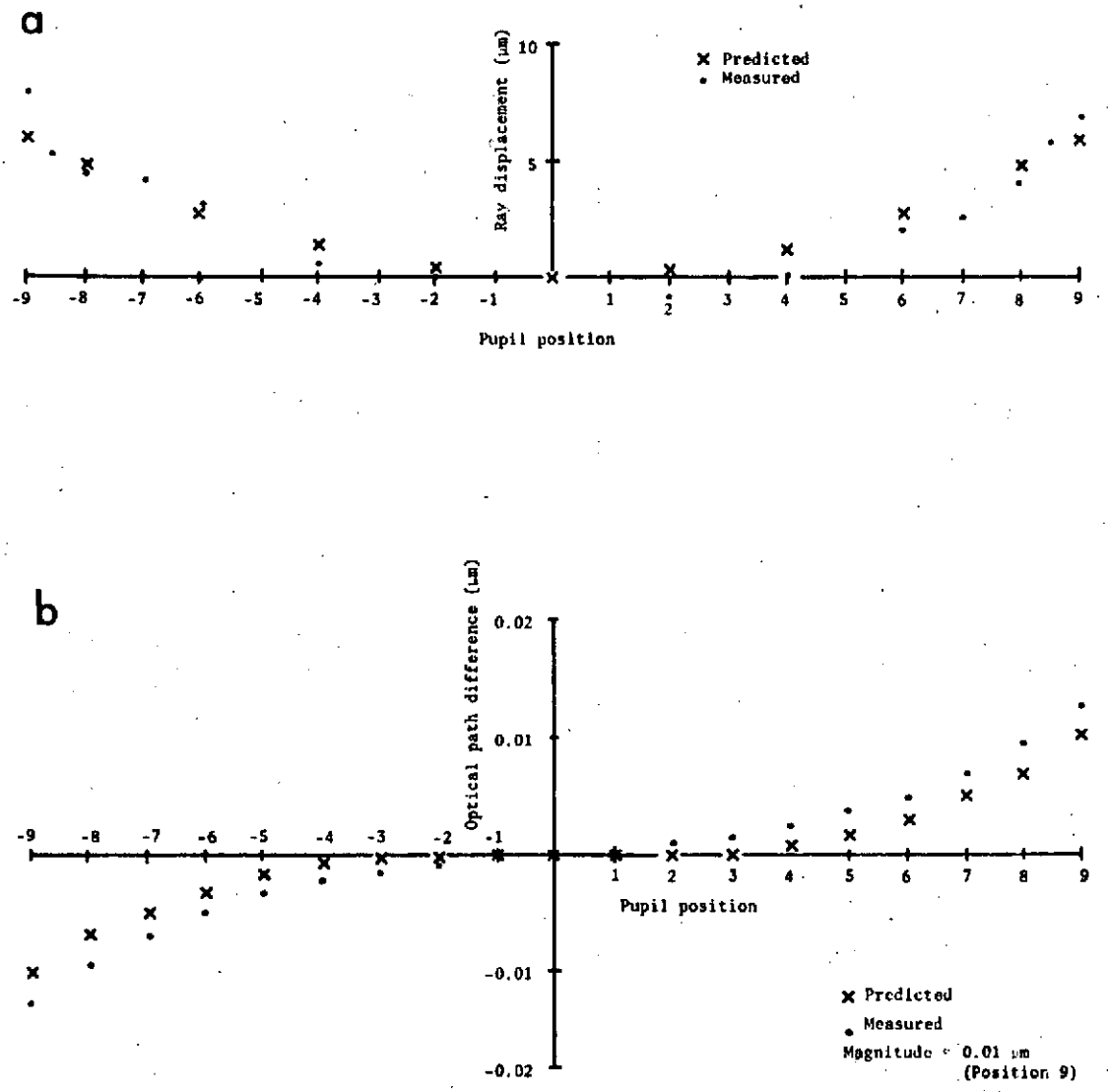

Fig. 16. Pupil position vs (a) ray displacement and (b) optical path difference for coma aberration at 0.01-μm magnitude

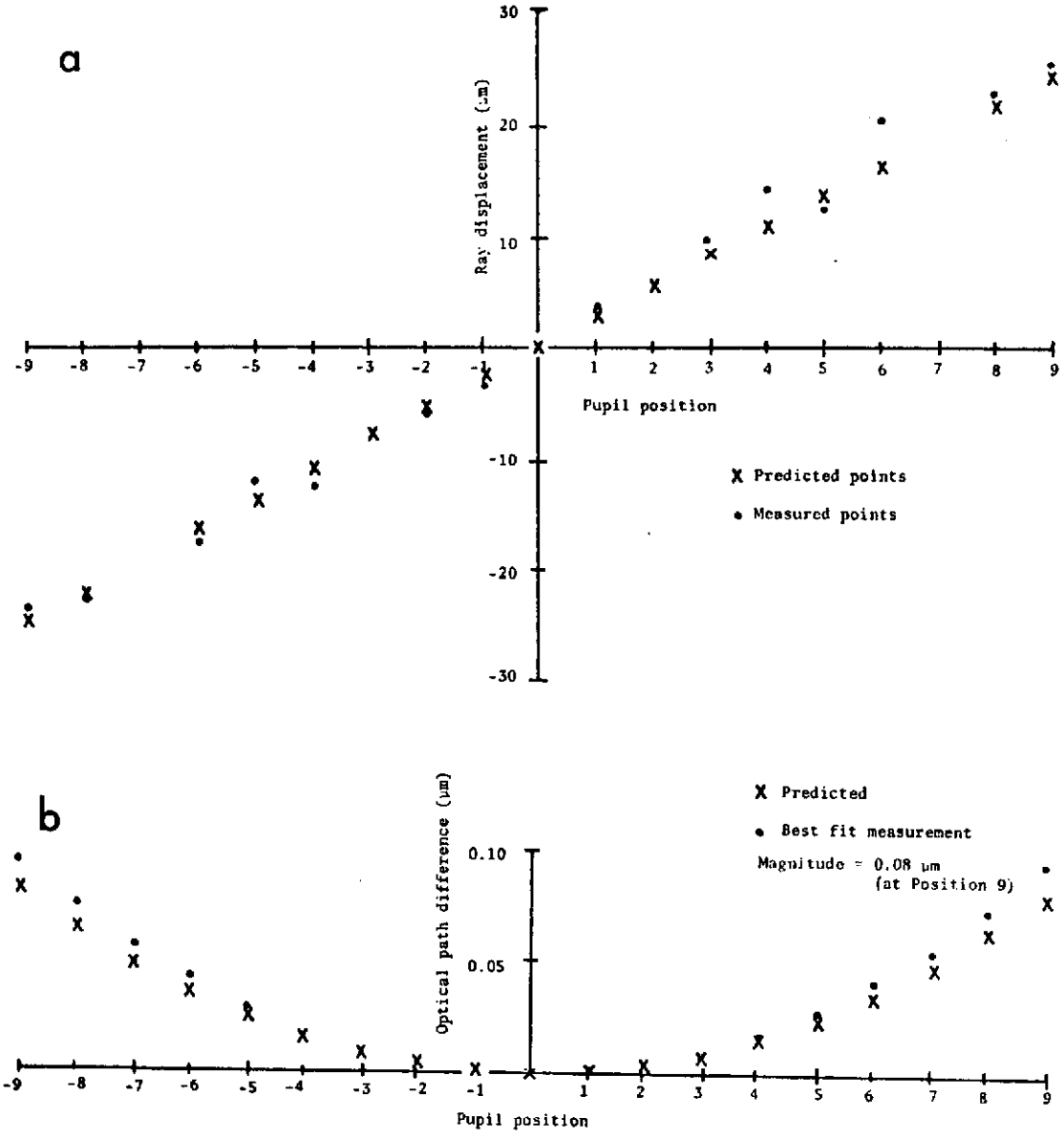

Fig. 17. Pupil position vs (a) ray displacement and (b) optical path difference for defocus aberration.

nominal parameters of the system. These theoretical values were obtained by differentiating the expression for OPD given in Chapter 2 and multiplying by the focal length of lens B.

iii. Data reduction procedure

In order to compute OPD changes from the measured ray deviation data the following procedure was followed.

The data on each of the graphs in Figs. 14a, 15a, 16a, and 17a were fitted to a low-order polynomial expression of the form $\varepsilon = a + br + cr^2 + dr^3 + er^4 + fr^5$ where ε is ray displacement in micrometers and r is sampled pupil position in micrometers. This yielded an analytical expression for ray deviation versus pupil position. To determine the OPD change this expression was divided by the focal length of lens B and integrated to obtain the expression for OPD

$$\text{OPD} = \frac{1}{f_B}\left[ar + \frac{b}{2}r^2 + \frac{c}{3}r^3 + \frac{d}{4}r^4 + \frac{e}{5}r^5 + \frac{f}{6}r^6\right] .$$

These data were then plotted in Figs. 14b, 15b, 16b, and 17b along with theoretical OPD's calculated from the equation developed in Chapter 2 for the wavefront error simulator.

iv. Discussion of results and errors

From an examination of Figs. 14a through 17a on ray displacement measurements, it is evident that the ability to measure ray deviations for the low-order aberrations was on the order of ± 1 μm compared to nominal predictions. Calculations on rms ray deviation measurements compared to the nominal predictions show a range of σ_{rms} = 1.4 μm in

the best case to σ_{rms} = 2 μm in the worst case. These correspond to rms angular errors of 0.2 arc sec and 0.3 arc sec, respectively.

A calculation of photon statistical S/N based upon the simulated star radiant output and PMT characteristics showed an expected S/N ratio of 4 for this order of angular sensitivity. As discussed previously, short-term vibrations under best conditions permitted ± 1 μm position measurement repeatability. Thus our measurement sensitivity, although approaching the statistical limit, as indicated by the nominal rms deviations calculated above, was indeed limited by residual laboratory vibration conditions.

From an inspection of the OPD's obtained by smoothing and integrating our ray displacement data (Figs. 14b, 15b, 16b, and 17b), we see that our measured values agree with the nominal predicted values to better than an indicated λ/100 in the best cases and to λ/40 at worst. It must be remembered that the nominal predicted curves have aberration generator systematic errors associated with them, which are discussed in Chapter 2. In addition, the vibrational noise contributes a λ/150 rms associated statistical error to the measured data. Considering these errors, it is reasonable to state that the aberrations were measured to the order of λ/50 to λ/100 using the Hartmann test. A more precise determination of sensitivity was influenced by residual laboratory vibrations and the systematic error associated with the wavefront error simulator calibration.

CHAPTER 4

FINE RANGE SENSORS

1. The Zernike Test

a. General Discussion

The usual interpretation of the Zernike test is based upon the spatial filtering concept. Consider a disturbance $e^{i\phi(x,y)}$ in the pupil of an optical system as shown in Fig. 18. If the aberrations are very small then we can represent $e^{i\phi(x,y)} = 1 + i\phi$. The important observation is that the aberration information and pupil information are 90° out of phase.

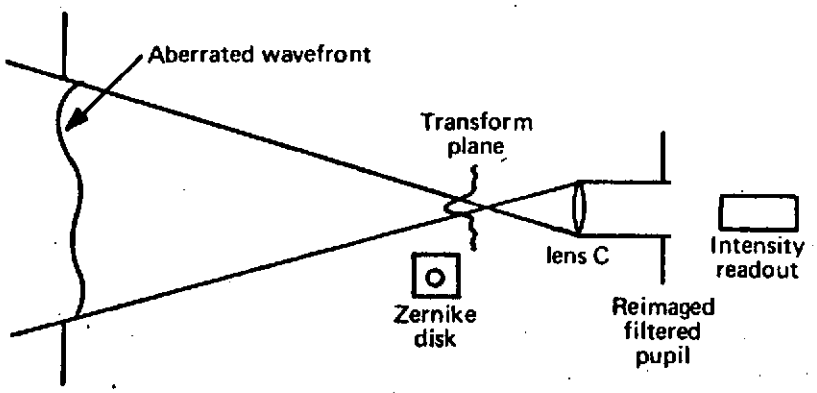

Fig. 18. Zernike phase contrast test arrangement.

If, in addition, the aberrations are of a high spatial frequency type, the Fourier transform of the pupil function consists of a zero order, due to the pupil aperture, and a separated higher order spectrum 90°

out of phase and separated from the zero order (see Fig. 19). We then argue that a phase delay of 90° introduced by a phase filter on the zero order will bring the higher-order information in phase with the zero order. Lens C then re-transforms the filtered spectrum with the aberration information and pupil effects in phase so that the intensity pattern in the pupil contains a modulation proportional to the phase error in the pupil for small aberrations. Furthermore, by attenuating the zero order, the modulation effects can be improved.

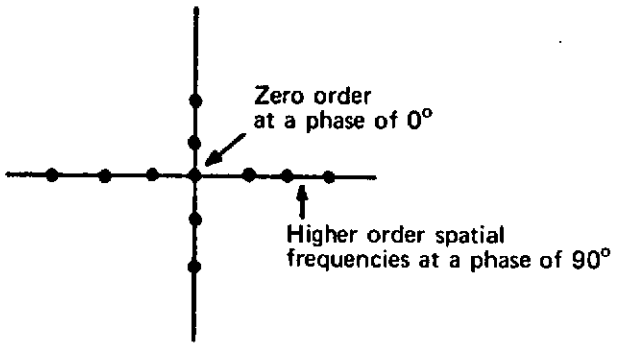

Fig. 19. Spatial frequency distribution.

In the situation where we are looking for low-order aberrations, such as may occur in figuring errors, thermal deformation errors, or misalignments, the problem is somewhat different. In this case the magnitudes of the aberrations are not so small that only a first-order expansion is permissible and, secondly, the aberration information is no longer separated out from the zero-order diffraction pattern. These considerations lead to a different interpretation of the problem as well as a more general formulation of the design of the Zernike disk

itself, in terms of its size, the optimum phase shift, and the optimum attenuation. Zernike did some work on the low order problem in terms of a Zernike polynomial representation of the aberrations. However, he considered only the first-order term in the expansion and did not generalize the problem considering obscuration effects. He also assumed the $\pi/4$ phase shift and did not consider optimization of the disk parameters. What follows is a general development of the effects of a Zernike disk on the reimaged pupil. We show the relationship between disk size, phase shifts, and attenuations, and how these parameters affect signal-to-noise ratio, fringe visibility, and the intensity in the reimaged pupil with and without various types of aberrations. We will also discuss the fabrication of the disk, effects of fabrication errors and tolerancing.

b. General Development of Intensity Equation for Reimaged Pupil

In Fig. 20 plane A represents the exit pupil, with fractional obscuration ϵ of an optical system with radius a and focal length f. The

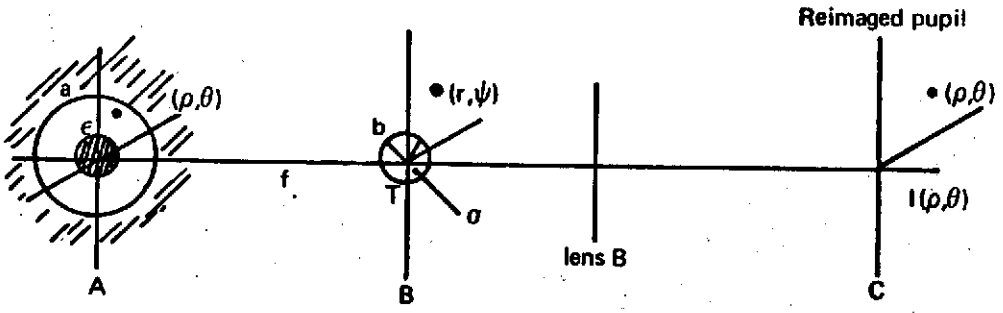

Fig. 20. Pupil geometry for Zernike equation derivations.

exit pupil contains a general wavefront represented by $e^{i\phi(\rho,\theta)}$. The normalized coordinate ρ ranges from ϵ to 1. The pupil amplitude is then represented by

$$P_o = e^{i\phi}\Pi\left(\frac{\rho}{2}\right)\left[1 - \Pi\left(\frac{\rho}{2\epsilon}\right)\right],$$

where

$$\Pi\left(\frac{\rho}{2x}\right) = 1 \qquad \frac{\rho}{x} \leq 1$$

$$= 0 \qquad \frac{\rho}{x} > 1.$$

At plane B, the Fraunhofer plane, the amplitude of the diffraction pattern $\tilde{P}$ is

$$\tilde{P} = K_1\tilde{P}_0,$$

where

$$\tilde{P}_0 = K_1 \int_0^1 \int_0^{2\pi} e^{i\phi}\, e^{-i[v\rho\cos(\theta-\psi)]}\rho d\rho d\theta$$

$$K_1 = -\frac{ia^2}{\lambda f} \qquad v = \frac{2\pi}{\lambda}\frac{a}{f}r$$

and r, ψ are coordinates in plane B.

In plane B we place a circular mask of radius b, which produces a phase shift σ within b and contains an amplitude attenuation (or relative amplification factor) T outside b. Thus, after passing through the mask $\tilde{P}$, the amplitude diffraction pattern becomes

$$\tilde{P}' = K_1 T \tilde{P}_0 \left[1 - \Pi\left(\frac{r}{2b}\right)\right] + e^{i\sigma} K_1 \tilde{P}_0 \Pi\left(\frac{r}{2b}\right).$$

By rearranging we obtain

$$\tilde{P}' = K_1 T \tilde{P}_0 + (e^{i\sigma} - T) K_1 \tilde{P}_0 \Pi\left(\frac{r}{2b}\right) = K_1 T \tilde{P}_0 + A e^{i\gamma} K_1 \tilde{P}_0 \Pi\left(\frac{r}{2b}\right),$$

where

$$A e^{i\gamma} = e^{i\sigma} - T$$

$$A^2 = 1 + T^2 - 2T \cos\sigma$$

$$\tan\gamma = \frac{\sin\sigma}{\cos\sigma - T}.$$

It is at this point that we make a very important observation. The first term in the above expression for $\tilde{P}'$ is an attenuated representation of the diffraction pattern of the system under test, while the second term represents an attenuated phase shifted core of the diffraction pattern, where A determines the attenuation, σ the phase shift, and b the size of the core. As we will see, this results in an expression for two-beam interferometer wave interference, where the first term transforms to the system test wave and the second term transforms to a self-generated reference wave.

This field $\tilde{P}'$ then passes through lens B and at plane C (the conjugate plane to A) the amplitude of the disturbance $P_0^{\,i}$ is

$$P_0^{\,i} = K_2 \tilde{\tilde{P}}'$$

where

$$\tilde{\tilde{P}}' = \int_0^{\infty} \int_0^{2\pi} \tilde{P}' e^{-iwr\cos(\psi-\theta')} r dr d\psi .$$

$$w = \frac{2\pi a \cdot \rho}{\lambda f} \qquad K_2 = \frac{i}{\lambda f} \qquad q = \frac{2\pi a}{\lambda f}$$

We are assuming lens B has an aperture sufficiently large to accept all scattered rays. Integrating we obtain

$$P_0^{\,i} = \frac{4\pi^2 K_1 K_2}{q^2} T\, e^{i\phi(-X,-Y)} \Pi\left(\frac{\rho}{2}\right) \left[1 - \Pi\left(\frac{\rho}{2\varepsilon}\right)\right] + A e^{i\gamma} K_1 K_2 \left[\widetilde{\tilde{P}_0 \Pi\left(\frac{r}{2b}\right)}\right]$$

where

$$\left[\widetilde{\tilde{P}_0 \Pi\left(\frac{r}{2b}\right)}\right] = \int_0^{b} \int_0^{2\pi} \tilde{P}_0 e^{-iwr\cos(\psi-\theta')} r dr d\psi$$

is in general a complex function $X(\rho,\psi)$

$$= X(\rho,\psi) = Q(\rho) e^{i\psi}$$

$$Q(\rho,\psi) = \sqrt{\text{Re } X^2 + \text{Im } X^2}$$

$$\psi(\rho,\psi) = \arctan \frac{\text{Im } X(\rho,\psi)}{\text{Re } X(\rho,\psi)} .$$

Substituting we obtain

$$P_0^{\,i} = T\,P_0(-X,-Y) + \frac{a^2}{\lambda^2 f^2} A\,Q(\rho)e^{i(\psi+\gamma)}.$$

What we have here is an expression for a two-beam interferometer where $TP_0(-X,-Y)$ is the test beam containing the pupil aberration information and the second term represents a reference wave whose amplitude $\frac{a^2AQ(\rho)}{\lambda^2 f^2}$ and phase γ is determined by the Zernike disk properties. The factor ψ, as will be seen, represents the effects of the system aberrations on the reference wave. As it turns out, if b is chosen small enough, ψ is practically constant so that its effect is essentially one of shifting the intensity distribution by a constant. We will come back to the evaluation of $X(\rho)$ in the next section.

Multiplying $P_0^{\,i}$ by its complex conjugate yields the intensity of the reimaged pupil for a unit amplitude pupil function

$$I(\rho,\theta) = P_0^{\,i} \times P_0^{\,i*} = T^2 + \frac{1Q^2A^2}{16\lambda^4 F\#^4} - \frac{2TQA}{4\lambda^2 F\#^2}\sin(\xi+\psi-\phi(-X,-Y))$$

(holds for $\varepsilon \le \rho \le 1$)

where

$$\xi = \gamma - \pi/2$$

$$I(\rho,\theta) = \frac{A^2Q^2(\rho,\theta)}{16\lambda^4 F\#^4} \qquad \varepsilon > \rho > 1 .$$

Our development here gives us an added bonus in the intensity prediction outside the pupil.

The question now is: How to choose the values of T and σ to optimize the Zernike test performance? If we desire to operate on the midpoint of a fringe so we have maximum range (~ ± quarter wave) we want to choose $\xi = 0$. If this is the case we then have $\gamma = \xi + \pi/2 = \pi/2$. Then from $\tan\gamma = \sin\sigma/(\cos\sigma - T)$, we have the constraining condition that $T = \cos\sigma$, and thus $A^2 = 1 - T^2 = \sin^2\sigma$. Now we have to consider fringe visibility. The visibility

$$V = \left(\frac{2QAT}{4\lambda^2F\#2}\right) \div \left(T^2 + \frac{Q^2A^2}{16\lambda^4F\#4}\right) = \left(\frac{Q\sin2\sigma}{4\lambda^2F\#2}\right) \div \left[1 + \frac{Q^2}{16\lambda^4F\#4} + \left(1 - \frac{Q^2}{16\lambda^4F\#4}\right)\cos2\sigma\right].$$

By differentiating and setting equal to zero, we obtain the condition for maximum visibility

$$\cos2\sigma = -\frac{1 - \frac{Q^2}{16\lambda^4F^4}}{1 + \frac{Q^2}{16\lambda^4F^4}}.$$

Thus, by picking σ to satisfy this equation and the transmission to satisfy the equation $T^2 = \cos^2\sigma$, we guarantee a fringe visibility of unity and an operating point that gives us maximum range. We see that the choice of σ depends upon $\frac{Q(\rho)}{16\lambda^4F^4}$, which depends upon wavelength, system F number, and the size of the Zernike disk. As we will demonstrate later, the effect of a large Zernike disk is to yield a reimaged pupil that has large intensity graduations for a zero-aberration condition. A large Zernike disk also tends to mix aberration information into

the reference wave. Smaller disks tend to yield a uniform zero-abberation profile with little aberration mixing in the reference wave. However, the transmission factor is small and more energy is wasted. In Table V we have calculated results for the optimum phase shift and transmission required for several Zernike disk radii, corresponding to about 1/10 to 1/2 the size of the diffraction pattern of an f/12 system operating at a wavelength of 0.6 μm, making use of expressions for Q derived in the following sections. Considering signal-to-noise requirements, pupil profile, and aberration mixing, the disk corresponding to about 1/3 the size of the central diffraction lobe appears to be a good compromise.

Table 5

Zernike disk design parameters at 0.6 μm

Disk size (μm)	Phase delay σ (in λ)	T^2 (%)
2	0.228	2
3	0.206	7
4	0.189	13.8
5	0.178	18.8

c. Derivation of the Effects of the Zernike Disk on the Reimaged Pupil

The effect of the Zernike disk on the reimaged pupil manifests itself through the term $X(\rho,\theta) = Q(\rho,\theta)e^{i\psi(\rho,\theta)}$. One can evaluate the integral

$$X(\rho,\theta) = \int_0^b \int_0^{2\pi} U(r,\psi)e^{-iwr\cos(\psi-\theta)}rdrd\psi,$$

where $U(r,\psi)$ is the amplitude diffraction pattern, numerically using a good deal of computer time. We have however, taken the approach of developing analytical expressions for both $U(r,\psi)$ and $X(\rho,\theta)$. The work has provided accurate analytical expressions for $U(r,\psi)$ for aberrations of up to .22λ and accurate analytical expressions for $X(\rho,\theta)$ for Zernike disk sizes up to 2/5 of an Airy disk size. The range of accuracy could be improved by expanding the expressions developed to include higher orders. The derivations have included the effects introduced by a system obscuration.

First we develop analytical expressions for the diffraction pattern amplitude $U(r,\psi)$, which includes aberration effects and the effect of a circular obscuration. The derivations that follow are done in terms of special functions $\Lambda_N(v)$ called Lambda functions. The Lambda function is defined such that

$$\Lambda_N(v) = 2^N N! \frac{J_N(v)}{v^N}$$

where $J_N(v)$ is an Nth order Bessel function. Using the recursion formula for Bessel's function one can show that

$$\Lambda_N(v) = \Lambda_{N-1}(v) + \frac{v^2}{4N(N+1)}\Lambda_{N+1}(v)$$

$$\Lambda(\tfrac{\rho}{2})(1-\rho^2)^N\rho^M\cos^M\theta \leftrightarrow (-i)^M \frac{\pi}{N+1}\left[\frac{1}{(2\pi)^M}\frac{\partial^M}{\partial Y^M}\Lambda_{N+1}(v)\right] \qquad (A)$$

where $\leftrightarrow$ represents a two-dimensional Fourier transform, and

$$v = 2\pi r_1$$

$$r_1 = \sqrt{X^2 + Y^2}$$

$$X = \frac{X_o a}{\lambda f}$$

$$Y = \frac{Y_o a}{\lambda f} .$$

We can also show that

$$\frac{d\Lambda_N(v)}{dv} = -\frac{1}{2} v \frac{\Lambda_{N+1}(v)}{N+1}$$

$$\frac{d^2\Lambda_N(v)}{dv^2} = \frac{2N+1}{2N+2} \Lambda_{N+1}(v) - \Lambda_N(v)$$

$$\frac{d^2\Lambda_N(v)}{dv^2} = -\frac{1}{2} v \frac{1}{4}\left[\Lambda_{N+2}(v) - \frac{\Lambda_{N+1}(v)}{N+1}\right]$$

$$\frac{\partial}{\partial Y} \Lambda_{N+1}(v) = 2\pi\cos\psi\left[-\frac{1}{2} v \frac{\Lambda_{N+2}(v)}{N+2}\right]$$

$$\frac{\partial^2}{\partial Y^2} \Lambda_{N+1}(v) = -\frac{(2\pi)^2}{4} (1-\cos 2\psi) \frac{\Lambda_{N+2}(v)}{N+2}$$

$$+ \frac{(2\pi)^2}{2} (1+\cos 2\psi)\left[\frac{2N+3}{2N+4} \Lambda_{N+2}(v) - \Lambda_{N+1}(v)\right]. \qquad (B)$$

The approach is now as follows. The pupil function $e^{i\phi}$ is expanded to the second term, $1 + i\phi - \frac{1}{2}\phi^2$, where

$$\phi = W_{11}\rho\cos\phi + W_{20}\rho^2 + W_{40}\rho^4 + W_{60}\rho^6 + W_{31}\rho^3\cos\phi + W_{22}\rho^2\cos^2\phi.$$

This is a power series representation of the phase in the pupil where W_{11} is a tilt effect, W_{20} is a defocus effect, W_{40} and W_{60} are spherical aberration effects, W_{31} is a coma effect, and W_{22} is an astigmatism effect. This expansion is substituted into

$$U(r,\psi) = K_1 \int_{\varepsilon}^{1} \int_{0}^{2\pi} e^{i\phi} e^{-i[v\rho\cos(\theta-\psi)]} \rho\, d\rho\, d\theta$$

where

$$e^{i\phi} \simeq 1 + i\phi - \phi^2/2.$$

After substitution we arrive at a series of transforms of terms of the form $\rho^{2N+M}\cos^M\theta$, where N and M take on various positive values. We can show that

$$\rho^{2N+M}\cos^M\theta = \left[1 - N(1-\rho^2) + \frac{N(N-1)}{2!}(1-\rho^2)^2 - \frac{N(N-1)(N-2)(1-\rho^2)^3}{3!} + \ldots\right] \cdot \cos^M\theta\rho^M.$$

By taking each term in the power expansion and putting it into the above form, applying the Fourier transform relationship (A) and finally making use of the derivative relationships (B), we arrive at the following

expression for diffraction amplitude in plane B

$$U = U_0 + U_{11} + U_{20} + U_{40} + U_{31} + U_{22} + U_{\text{Interactions}}$$

where $U_{\text{Interactions}}$ represent cross terms resulting from the ϕ^2 term in the pupil function where

$$U_0 = \Pi[\Lambda_1(v) - \varepsilon^2\Lambda_1(\varepsilon v)] \quad \text{--diffraction pattern of the obstructed aperture.}$$

$$K = \frac{2\pi}{\lambda} .$$

Defocus:

$$U_{02} = \Pi(iKW_{20})\left[\Lambda_1(v) - \frac{1}{2}\Lambda_2(v) - \varepsilon^4(\Lambda_1(\varepsilon v) - \frac{1}{2}\Lambda_2(\varepsilon v)\right]$$

$$- \frac{\Pi K^2 W_{20}^2}{2}\left[\Lambda_1(v) - \Lambda_2(v) + \frac{1}{3}\Lambda_3(v) - \varepsilon^4\left(\Lambda_1(\varepsilon v) - \Lambda_2(\varepsilon v) + \frac{1}{3}\Lambda_3(\varepsilon v)\right)\right]$$

Third-order spherical:

$$U_{40} = \Pi(iKW_{40})\left[\Lambda_1(v) - \Lambda_2(v) + \frac{1}{3}\Lambda_3(v) - \varepsilon^6\left(\Lambda_1(\varepsilon v) - \Lambda_2(\varepsilon v) + \frac{1}{3}\Lambda_3(\varepsilon v)\right)\right]$$

$$- \frac{\Pi}{2} K^2 W_{40}^2\left[\Lambda_1(v) - 2\Lambda_2(v) + \frac{5}{3}\Lambda_3(v) - \Lambda_4(v) + \frac{1}{5}\Lambda_5(v) - \varepsilon^{10}\left(\Lambda_1(\varepsilon v) - 2\Lambda_2(\varepsilon v) + \frac{5}{3}\Lambda_3(\varepsilon v) - \Lambda_4(\varepsilon v) + \frac{1}{5}\Lambda_5(\varepsilon v)\right)\right]$$

Tilt:

$$U_{11} = \Pi(iKW_{11})(iv\cos\psi)\left[\frac{1}{4}\Lambda_2(v) - \frac{1}{4}\varepsilon^4\Lambda_2(\varepsilon v)\right]$$

$$- \frac{\Pi}{2}K^2W_{11}{}^2\left[\frac{1}{2}\left(\Lambda_1(v) - \frac{1}{2}\Lambda_2(v)\right)\right.$$

$$+ \frac{1}{2}\left(\Lambda_1(v) - \Lambda_2(v)\right)\cos2\psi$$

$$\left. - \varepsilon^4\left[\frac{1}{2}\left(\Lambda_1(\varepsilon v) - \frac{1}{2}\Lambda_2(\varepsilon v)\right) + \frac{1}{2}\left(\Lambda_1(\varepsilon v) - \Lambda_2(\varepsilon v)\right)\cos2\psi\right]\right]$$

Astigmatism:

$$U_{22} = \Pi(iKW_{22})\left[\frac{1}{2}\left[\Lambda_1(v) - \frac{1}{2}\Lambda_2(v)\right] + \frac{1}{2}\left[\Lambda_1(v) - \Lambda_2(v)\right]\cos2\psi\right.$$

$$\left. - \varepsilon^4\left(\frac{1}{2}\left[\Lambda_1(\varepsilon v) - \frac{1}{2}\Lambda_2(\varepsilon v)\right] + \frac{1}{2}\left[\Lambda_1(\varepsilon v) - \Lambda_2(\varepsilon v)\right]\cos2\psi\right)\right]$$

$$- \frac{\Pi}{16}K^2W_{22}{}^2\left[\Lambda_3(v) - 3\Lambda_2(v) + 3\Lambda_1(v) + \cos2\psi\cdot\right.$$

$$\left[2\Lambda_3(v) - 6\Lambda_2(v) + 4\Lambda_1(v)\right]$$

$$+ \cos4\psi\left[2\Lambda_3(v) - 3\Lambda_2(v) + \Lambda_1(v)\right]$$

$$\left. - \varepsilon^6\right\{\Lambda_3(\varepsilon v) - 3\Lambda_2(\varepsilon v) + 3\Lambda_1(\varepsilon v) + \cos2\psi\cdot$$

$$\left[2\Lambda_3(\epsilon v) - 6\Lambda_2(\epsilon v) + 4\Lambda_1(\epsilon v)\right]$$

$$+ \cos 4\psi\left[2\Lambda_3(\epsilon v) - 3\Lambda_2(\epsilon v) + \Lambda_1(\epsilon v)\right]\Big\}\Big]$$

Coma:

$$U_{31} = \Pi(iKW_{31})(iv\cos\psi)\left[\frac{1}{4}\Lambda_2(v) - \frac{1}{12}\Lambda_3(v)\right.$$

$$\left. - \epsilon^6\left(\frac{1}{4}\Lambda_2(\epsilon v) - \frac{1}{12}\Lambda_3(\epsilon v)\right)\right.$$

$$- \frac{K^2\Pi}{4}W_{31}{}^2\left[\Lambda_1(v) - \frac{3}{2}\Lambda_2(v) + \Lambda_3(v) - \frac{\Lambda_4(v)}{4}\right.$$

$$\left. + \cos 2\psi\left[\Lambda_1(v) - 2\Lambda_2(v) + \frac{4}{3}\Lambda_3(v)\right]\right.$$

$$\left. - \epsilon^8\left(\left(\Lambda_1(\epsilon v) - \frac{3}{2}\Lambda_2(\epsilon v) + \Lambda_3(\epsilon v) - \frac{\Lambda_4(\epsilon v)}{4}\right)\right.\right.$$

$$\left.\left. + \cos 2\psi\left(\Lambda_1(\epsilon v) - 2\Lambda_2(\epsilon v) + \frac{4}{3}\Lambda_3(\epsilon v)\right)\right)\right]$$

$$U_{INTERACTION} = -\pi K^2 W_{20} W_{40}\left[\Lambda_1(v) - \frac{3}{2}\Lambda_2(v) + \Lambda_3(v) - \frac{1}{4}\Lambda_4(v) - \varepsilon^8\left(\Lambda_1(\varepsilon v) - \frac{3}{2}\Lambda_2(\varepsilon v) + \Lambda_3(\varepsilon v) - \frac{1}{4}\Lambda_4(\varepsilon v)\right)\right]$$

$$- \pi K^2 W_{11} W_{20}(iv\cos\psi)\left[\frac{1}{4}\Lambda_2(v) - \frac{1}{12}\Lambda_3(v) - \varepsilon^6\left(\frac{1}{4}\Lambda_2(\varepsilon v) - \frac{1}{12}\Lambda_3(\varepsilon v)\right)\right]$$

$$- \frac{\pi k^2}{2}(W_{31}W_{11} + W_{20}W_{22})\left[\Lambda_1(v) - \Lambda_2(v) + \frac{\Lambda_3(v)}{3} + \cos 2\psi\left[\Lambda_1(v) - \frac{3}{2}\Lambda_2(v) + \frac{\Lambda_3(v)}{2}\right] - \varepsilon^6\left(\Lambda_1(\varepsilon v) - \Lambda_2(\varepsilon v) + \frac{\Lambda_3(\varepsilon v)}{3}\right) + \cos 2\psi\left(\Lambda_1(\varepsilon v) - \frac{3}{2}\Lambda_2(\varepsilon v) + \frac{\Lambda_3(\varepsilon v)}{2}\right)\right]$$

$$- iK^2\pi v\cos\psi(W_{11}W_{40} + W_{20}W_{31})\left[\frac{\Lambda_2(v)}{4} - \frac{\Lambda_3(v)}{6} + \frac{\Lambda_4(v)}{24} - \varepsilon^8\left(\frac{\Lambda_2(\varepsilon v)}{4} - \frac{\Lambda_3(\varepsilon v)}{6} + \frac{\Lambda_4(\varepsilon v)}{24}\right)\right]$$

$$- iK^2W_{40}W_{31}\pi v \cos\psi\left[\frac{\Lambda_2(v)}{4} - \frac{\Lambda_3(v)}{4} + \frac{\Lambda_4(v)}{8} - \frac{\Lambda_5(v)}{40}\right.$$

$$\left. - \varepsilon^{10}\left(\frac{\Lambda_2(\varepsilon v)}{4} - \frac{\Lambda_3(\varepsilon v)}{4} + \frac{\Lambda_4(\varepsilon v)}{8} - \frac{\Lambda_5(\varepsilon v)}{40}\right)\right]$$

$$- \frac{iK^2\pi W_{11}W_{22}}{16}\left[\left(\left(-v\Lambda_3(v) + 3v\Lambda_2(v)\right)\cos\psi + \left(v\Lambda_2(v) - v\Lambda_3(v)\right)\cos 3\psi\right.\right.$$

$$\left.\left. - \varepsilon^6\left(\left(-v\Lambda_3(\varepsilon v) + 3v\Lambda_2(\varepsilon v)\right)\cos\psi + \left(v\Lambda_2(\varepsilon v) - v\Lambda_3(\varepsilon v)\right)\cos 3\psi\right)\right]$$

$$- \frac{iK^2\pi W_{31}W_{22}}{16}\left[\left(3\Lambda_2(v) - 2\Lambda_3(v)\right) + \frac{1}{2}\Lambda_4(v)\, v\cos\psi + \left(\Lambda_2(v) - \frac{4}{3}\Lambda_3(v)\right.\right.$$

$$\left. + \frac{1}{3}\Lambda_4(v)\right) v\cos 3\psi$$

$$- \varepsilon^8\left[\left(3\Lambda_2(\varepsilon v) - 2\Lambda_3(\varepsilon v) + \frac{1}{2}\Lambda_4(\varepsilon v)\right) v\cos\psi\right.$$

$$\left.\left. + \left(\Lambda_2(\varepsilon v) - \frac{4}{3}\Lambda_3(\varepsilon v) + \frac{1}{3}\Lambda_4(\varepsilon v)\right) v\cos 3\psi\right]\right]$$

The above expression enables us to determine the diffraction pattern amplitude in the presence of third-order aberrations less than quarter-wave in magnitude, where the effect of a circular obscuration has been included.

We now want to determine the analytical expression that describes the effect of the Zernike disk on the reimaged pupil. We do this by substituting the previous derived expression for $U(r,\psi)$ into the integral expression for $X(\rho,\theta)$. We then make use of the fact that the Λ functions can be expanded in a power series where

$$\Lambda_{N-1}(\varepsilon v) = 1 - \frac{\varepsilon^2 v^2}{4N} + \frac{\varepsilon^4 v^4}{16N^2(\frac{2}{N} + 2)} + \ldots .$$

We apply the three terms of the expansion to the unaberrated pupil U_o, and the quadratic approximation to the aberration terms. We also make use of the recursion relationship for Bessel functions

$$J_{N-1}(v) + J_{N+1}(v) = \frac{2N\, J_N(v)}{v},$$

and the integral relationships

$$\int_0^{2\pi} \cos M\theta e^{-iv\rho\cos(\theta-\psi)} d\theta = (-i)^M 2\pi\, J_M(v\rho)\cos M\psi,$$

and

$$\int_0^1 \rho^{\nu+1} J_\nu(v\rho)\, d\rho = \frac{1}{v} J_{\nu+1}(v).$$

After a good deal of tedious manipulation and evaluation we obtain

$$X(\rho,0) = X_o(\rho,0) + X_{Ab}(\rho,0),$$

where $X_o(\rho,\theta)$ is the effect of the Zernike disk on the unaberrated pupil and $X_{Ab}(\rho,\theta)$ is the effect rendered on the aberrated wavefront

$$X_o(\rho,\theta) = 2\pi^2 b^2\left[\frac{J_1(wb)}{wb} - \frac{b^2q^2}{8}\left(\frac{2}{w^2b^2}J_2(wb) - \frac{J_3(wb)}{wb}\right)\right]$$

$$- 2\pi^2\varepsilon^2 b^2\left[\frac{J_1(wb)}{wb} - \frac{b^2\varepsilon^2q^2}{8}\left(\frac{2}{w^2b^2}J_2(wb) - \frac{J_3(wb)}{wb}\right)\right]$$

$$+ \frac{2\pi^2b^6q^4}{192}\left[1-\varepsilon^6\right]\left[\frac{J_1(wb)}{wb} - \frac{4J_2(wb)}{w^2b^2} + \frac{8J_3(wb)}{w^3b^3}\right]$$

$$X_{Aberration}(\rho,\theta) = 2\pi^2b^2iKW_{20}\left[\frac{J_1(wb)}{2wb} - \frac{b^2q^2}{12}\left(\frac{2}{w^2b^2}J_2(wb) - \frac{J_3(wb)}{wb}\right)\right]$$

$$- i2\pi^2b^2KW_{20}\varepsilon^4\left[\frac{J_1(wb)}{2wb} - \frac{b^2\varepsilon^2q^2}{12}\left(\frac{2J_2(wb)}{w^2b^2} - \frac{J_3(wb)}{wb}\right)\right]$$

$$- b^2\pi^2K^2W_{20}{}^2\left[\frac{J_1(wb)}{3wb} - \frac{b^2q^2}{16}\left(\frac{2}{w^2b^2}J_2(wb) - \frac{J_3(wb)}{wb}\right)\right]$$

$$+ b^2\pi^2K^2\varepsilon^6W_{20}{}^2\left[\frac{J_1(wb)}{3wb} - \frac{b^2q^2\varepsilon^2}{16}\left(\frac{2}{w^2b^2}J_2(wb) - \frac{J_3(wb)}{wb}\right)\right]$$

$$+ 2\pi^2b^2iKW_{40}\left[\frac{J_1(wb)}{3wb} - \frac{b^2q^2}{16}\left(\frac{2}{w^2b^2}J_2(wb) - \frac{J_3(wb)}{wb}\right)\right]$$

$$- i2\pi^2 b^2 K W_{40} \varepsilon^6 \left[\frac{J_1(wb)}{3wb} - \frac{b^2\varepsilon^2 q^2}{12} \left(\frac{2J_2(wb)}{w^2b^2} - \frac{J_3(wb)}{wb} \right) \right]$$

$$- b^2\pi^2 K^2 W_{40}{}^2 \left[\frac{J_1(wb)}{5wb} - \frac{b^2 q^2}{24} \left(\frac{2}{w^2b^2} J_2(wb) - \frac{J_3(wb)}{wb} \right) \right]$$

$$+ b^2\pi^2 K^2 W_{04}{}^2 \varepsilon^{10} \left[\frac{J_1(wb)}{5wb} - \frac{b^2 q^2 \varepsilon^2}{24} \left(\frac{2J_2(wb)}{w^2b^2} - \frac{J_3(wb)}{wb} \right) \right]$$

$$+ iq2\pi^2 K W_{11} \cos\theta \left[\frac{J_2(wb)}{4wb} b^3 + \frac{q^2 b^5}{48} \left(\frac{2}{w^2b^2} J_3(wb) - \frac{J_2(wb)}{wb} \right) \right]$$

$$- iq2\pi^2 K \cos\theta W_{11} \varepsilon^4 \left[\frac{J_2(wb)}{4wb} b^3 + \frac{q^2\varepsilon^2 b^5}{48} \left(\frac{2}{w^2b^2} J_3(wb) - \frac{J_2(wb)}{wb} \right) \right]$$

$$- b^2 \frac{\pi^2}{2} K^2 W_{11}{}^2 \left[\frac{J_1(wb)}{2wb} - \frac{b^2 q^2}{12} \left(\frac{2}{w^2b^2} J_2(wb) - \frac{J_3(wb)}{wb} \right) + \cos 2\theta \frac{b^2 q^2}{24wb} J_3(wb) \right.$$

$$- \varepsilon^4 \left(\frac{J_1(wb)}{2wb} - \frac{b^2\varepsilon^2 q^2}{12} \left(\frac{2}{w^2b^2} J_2(wb) - \frac{J_3(wb)}{wb} \right) \right.$$

$$\left. \left. + \cos 2\theta \frac{b^2\varepsilon^2 q^2}{24wb} J_3(wb) \right) \right]$$

$$+ iq2\pi^2 KW_{31}\cos\theta\left[\frac{J_2(wb)}{6wb}\, b^3 + \frac{q^2b^5}{64}\left(\frac{2}{w^2b^2}\, J_3(wb) - \frac{J_2(wb)}{wb}\right)\right]$$

$$- iq2\pi^2 KW_{31}\cos\theta\varepsilon^6\left[\frac{J_2(wb)}{6wb}\, b^3 + \frac{q^2\varepsilon^2b^5}{64}\left(\frac{2}{w^2b^2}\, J_3(wb) - \frac{J_2(wb)}{wb}\right)\right]$$

$$- \frac{K^2\pi^2 W_{31}{}^2 b^2}{2}\left[\frac{J_1(wb)}{4wb} - \frac{b^2q^2}{20}\left[\frac{2}{w^2b^2}\, J_2(wb) - \frac{J_3(wb)}{wb}\right] + \cos2\theta\, \frac{b^2q^2J_3(wb)}{40wb}\right.$$

$$\left. - \varepsilon^8\left(\frac{J_1(wb)}{4wb} - \frac{b^2q^2\varepsilon^2}{20}\left(\frac{2}{w^2b^2}\, J_2(wb) - \frac{J_3(wb)}{wb}\right) + \cos2\theta\left(\frac{b^2\varepsilon^2q^2}{40wb}\, J_3(wb)\right)\right)\right]$$

$$+ i\pi^2 KW_{22}\left[\left(\frac{b^2J_1(wb)}{2wb} - \frac{b^4q^2}{12}\left(\frac{2}{w^2b^2}\, J_2(wb) - \frac{J_3(wb)}{wb}\right) + \cos2\theta\, \frac{b^4q^2}{24wb}\, J_3(wb)\right)\right.$$

$$\left. - \varepsilon^4\left(\frac{b^2J_1(wb)}{2wb} - \frac{b^4q^2\varepsilon^2}{12}\left(\frac{2}{w^2b^2}\, J_2(wb) - \frac{J_3(wb)}{wb}\right) + \cos2\theta\, \frac{b^4q^2\varepsilon^2J_3(wb)}{24wb}\right)\right]$$

$$- \frac{3}{8}\, K^2\pi^2 W_{22}{}^2\left[\left(\frac{b^2J_1(wb)}{3wb} - \frac{b^4q^2}{16}\left(\frac{2}{w^2b^2}\, J_2(wb) - \frac{J_3(wb)}{wb}\right)\right) + \cos2\theta\, \frac{b^4q^2}{24wb}\, J_3(wb)\right.$$

$$\left. - \varepsilon^6\left[\frac{b^2J_1(wb)}{3wb} - \frac{b^4q^2\varepsilon^2}{16}\left[\frac{2}{w^2b^2}\, J_2(wb) - \frac{J_2(wb)}{wb}\right] + \cos2\theta\, \frac{b^4q^2\varepsilon^2}{24wb}\, J_3(wb)\right.\right.$$

plus cross terms.

This equation has been programmed and the data run to obtain $X(\rho,\theta)$ for cases that show the effect of the Zernike disk radius on $X(\rho)$. As stated before, this information was used to calculate σ and T and is tablulated in Table V. These data were then used to obtain the no-aberration profiles for the reimaged pupil, which appear in Fig. 21. These vividly demonstrate the tradeoff between disk size and pupil uniformity. For an f/12 system operating at an effective wavelength of 0.6 μm, a 3- to 4-μm Zernike radius appears to be a reasonable compromise.

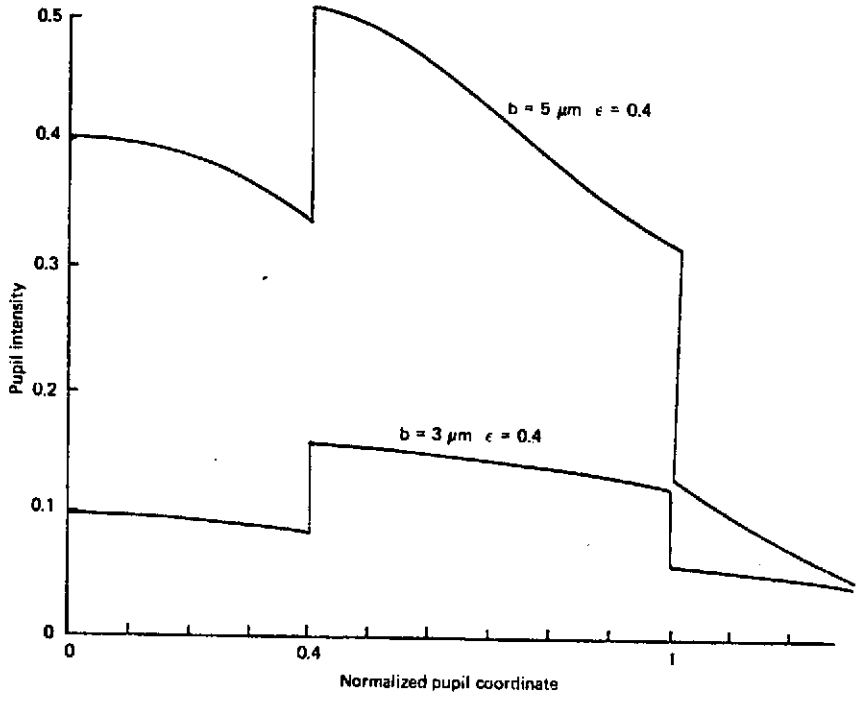

Fig. 21. Reimaged pupil through Zernike disk (no aberration).

d. Effect of Zernike Disk Size on the Reference Wave Characteristics in the Presence of Aberrations

The general equation for interference could, theoretically, be used to calculate the unknown system aberration, ϕ, from intensity measurements across the pupil, for any size Zernike disk. Of course, the process would involve a complicated interactive approach to obtain ϕ, since both Q and ψ are, in general, functions of the aberration ϕ. In other words, the reference wave amplitude and phase are, in general, affected by the aberration, and this effect must be taken into consideration when the intensity modulation in the reimaged pupil is analyzed. However, if the size of the Zernike disk is restricted, the reference wave amplitude variations can be kept within an acceptable departure from the amplitude of the nonaberrated reference wave, and the reference wave phase variation can be restricted to a constant shift plus a small linear variation, thus simplifying the interpretation of the intensity profile of the reimaged pupil.

Reference wave characteristics were determined from the derived equations for $X(\rho,\theta)$, assuming an f/12 system with an obscuration ratio of 0.4 operating at 0.6 μm wavelength. Zernike disk radii of 2, 3, 4, and 5 μm were used for the analysis. The primary consideration was to determine the effects produced by the various size disks on the reference wave as a function of the presence of different low-order aberrations. The most important results of this investigation are presented below.

It was found that the primary effect produced by the aberrations mixing in the reference wave was on ψ, the reference wave phase. The aberrations that caused change in Q, the amplitude factor of the reference

wave, were minimal and could be described, for the smaller disks, as a small constant percentage reduction in the reference wave amplitude. This amplitude reduction is due to the redistribution of energy out of the core of the aberrated diffraction pattern. The effect introduced by the larger disk (5 μm) showed departures from the constant percentage reduction, but the overall change remained small when compared to the variations introduced in the reference wave phase, ψ. Thus, for the sizes considered, amplitude variations were considered secondary, and the choice of the upper limit on disk size was dependent on the reference wave phase variations, which were taken as the primary indicator of aberration interaction in the reference wave.

The interaction of an aberrated test wave with the Zernike disk *always* produces a change in the reference wave phase ψ. For the even aberrations (defocus, spherical, astigmatism) the change rendered on ψ could be described, generally, as consisting of small nonlinear phase variation superimposed on a rather large constant phase shift. The smaller the disk the larger the constant phase shift, but the larger the disk, the greater the nonlinear phase variations. The odd aberrations (tilt, coma) caused a linear phase shift in the reference wave with superimposed small nonlinear variations. These effects decreased as the disk size decreased, and went to zero in a direction perpendicular to the orientation of the system aberration. The phenomena described above are indicated by the variations in ψ, which have been sketched in Figs. 22a through 22e, for the various disk sizes and aberration conditions.

The largest amounts of nonlinear variation in ψ were produced by the interaction of an astigmatic wave with the Zernike disk. If the 5-μm disk were used to measure astigmatism of 0.2 waves, a $\lambda/40$ astigmatic type perturbation would be introduced into the measurement because of the slight astigmatic quality of the reference wave.

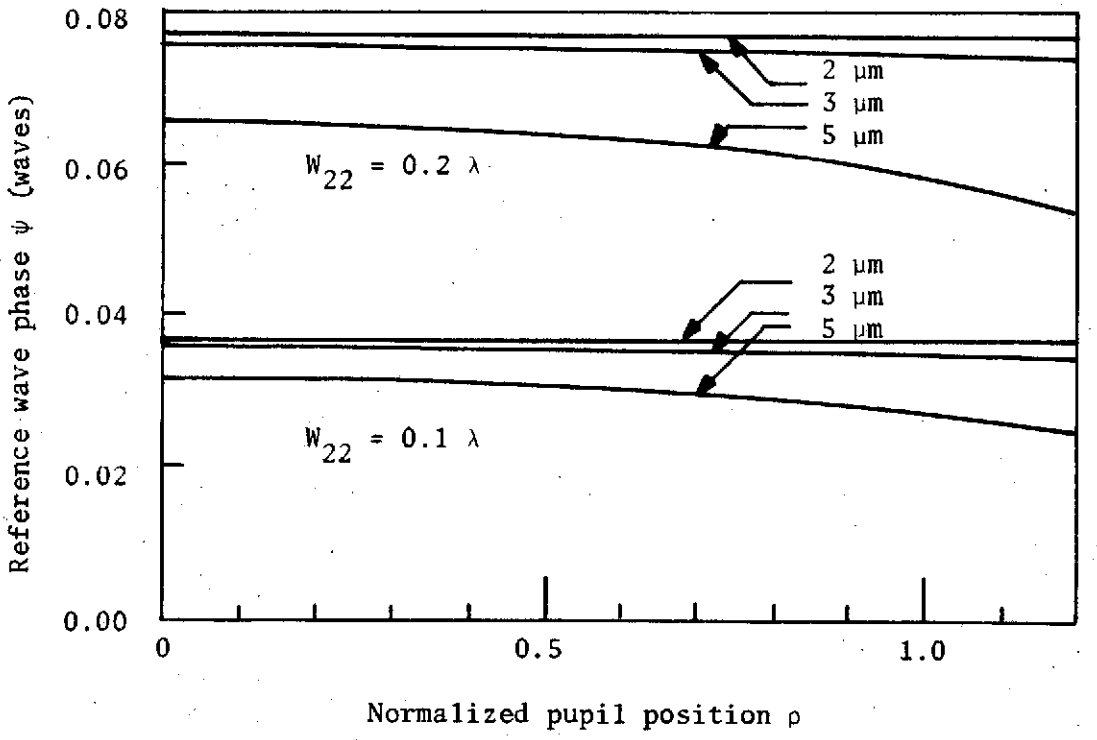

(a) Astigmatism W_{22} ($\theta = 90°$)

Fig. 22. Variation in reference wave phase as a function of normalized pupil position.

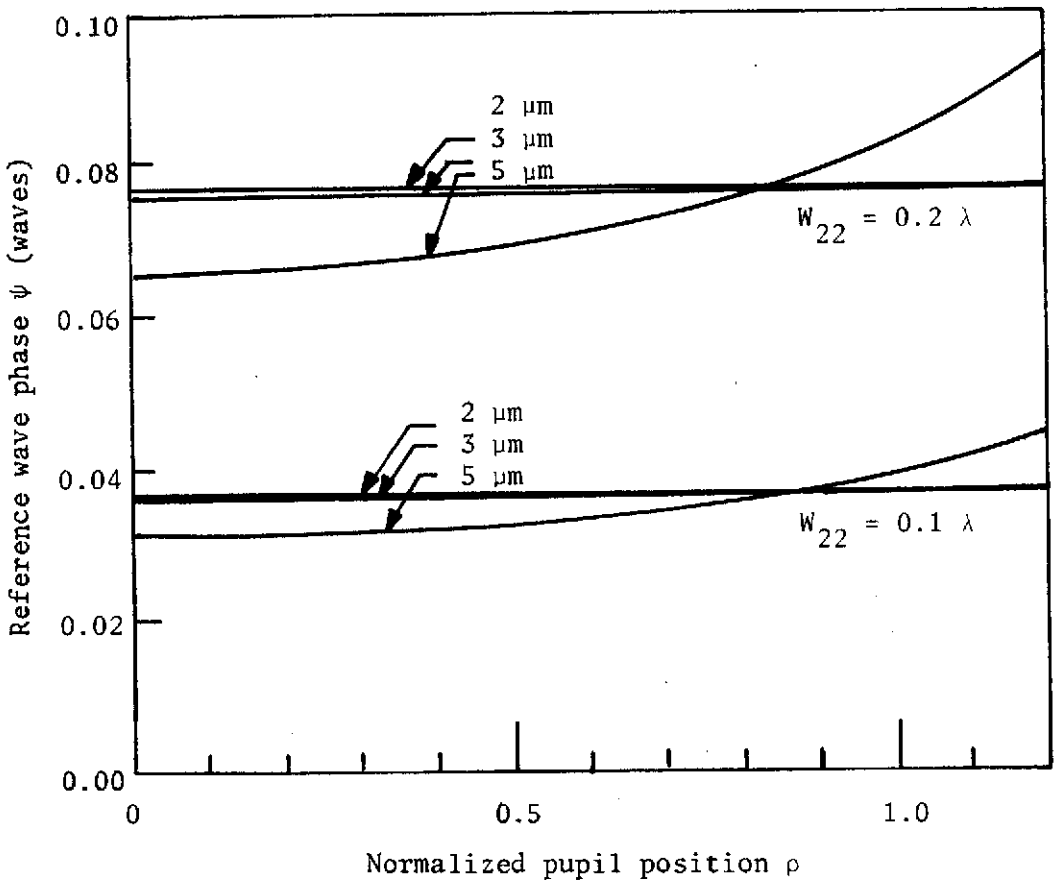

(b) Astigmatism W_{22} ($\theta = 0^{o}$)

Fig. 22. (Continued).

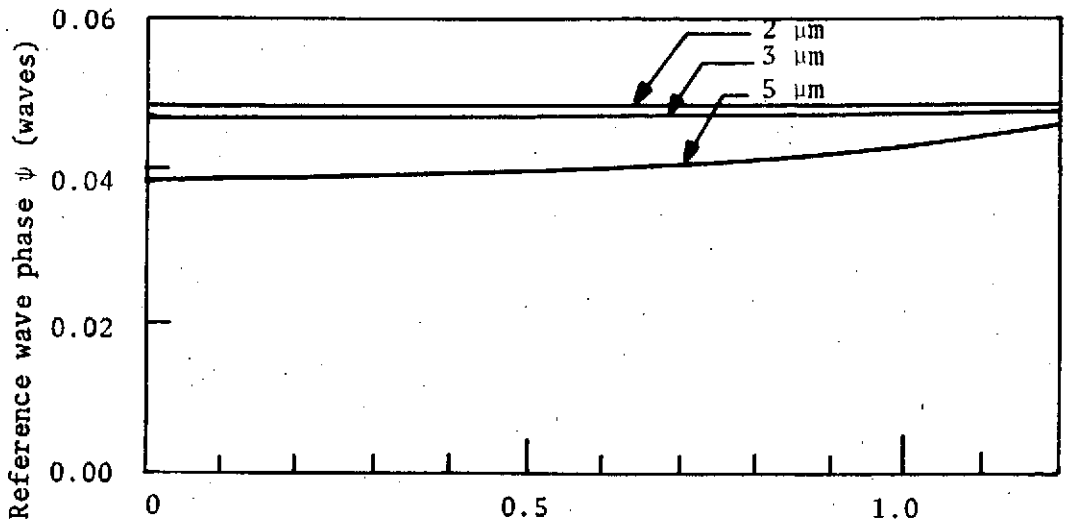

(c) Spherical aberration W_{40} = 0.1 λ

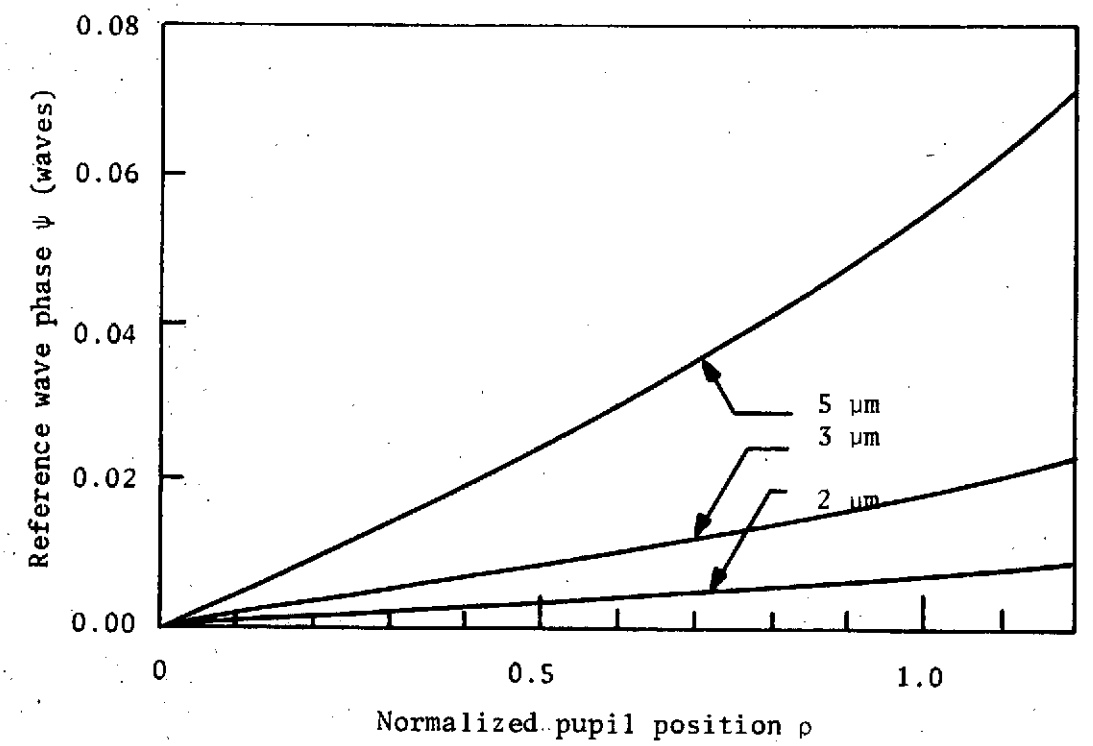

(d) Tilt W_{11} = 0.1 λ

Fig. 22. (Continued).

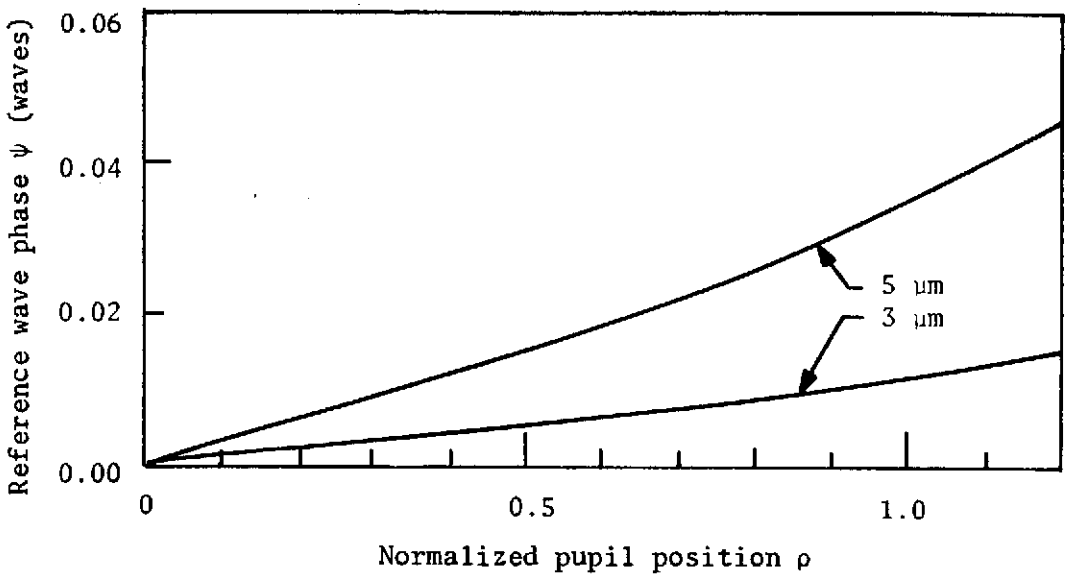

(e) Coma $W_{31} = 0.1\ \lambda$

Fig. 22. (Continued).

Similar statements could be made about the nonlinear perturbations arising out of the presence of coma or tilt. These effects are, however, smaller than those caused by the astigmatic wavefront. The analysis showed that if the Zernike disk size were kept to 2 μm or less, the nonlinear perturbations of the reference wave phase ψ would be essentially zero. However, if availability of light were a limiting factor, the Zernike disk could be chosen to have around a 3-μm radius, with the nonlinear effects amounting to no more than a few thousandths of a wave for the largest aberration being measured. These nonlinear effects would become vanishingly small, as the aberrations decreased to less than λ/20. Thus, if the Zernike disk size were limited to 3 μm, the nonlinear variations in ψ and the small nearly constant percentage reduction in reference wave amplitude could be ignored with better than

$\lambda/100$ accuracy over a $\pm \lambda/7$ operating range. If the operating range requirements were reduced, the disk size requirements could be relaxed while maintaining better than $\lambda/100$ accuracy. However, the constant shift in reference wave phase produced by the even aberrations, and the small linear phase shift in ψ, caused by the odd aberrations, must always be considered in the interpretation of the intensity distribution. The constant shift in ψ caused by the presence of the even aberrations is somewhat beneficial in that it effectively shifts the operating point on the fringe in the direction opposite to variations caused by the aberration ϕ. This effectively extends the linear range of operation for the even aberrations. The linear phase variation in ψ caused by the odd aberrations does not complicate the data reduction since the linear phase effects in ϕ caused by wavefront tilt would have to be considered in interpreting the reimaged pupil intensity distribution.

Figure 23a and b illustrates the modulation effects within the reimaged pupil and the diffracted reference wave intensity outside of the reimaged pupil. These graphs were generated assuming the use of an optimized 3-μm Zernike disk, testing an f/12, 0.4 obscuration ratio telescope under different aberration conditions. The figures graphically illustrate the small relative change of the reference wave amplitude for the 3-μm disk size as well as the excellent sensitivity of the test.

e. Tolerancing of Disks

As mentioned before, the ideal transmission and phase delay can be calculated from the equations developed for the Zernike disk.

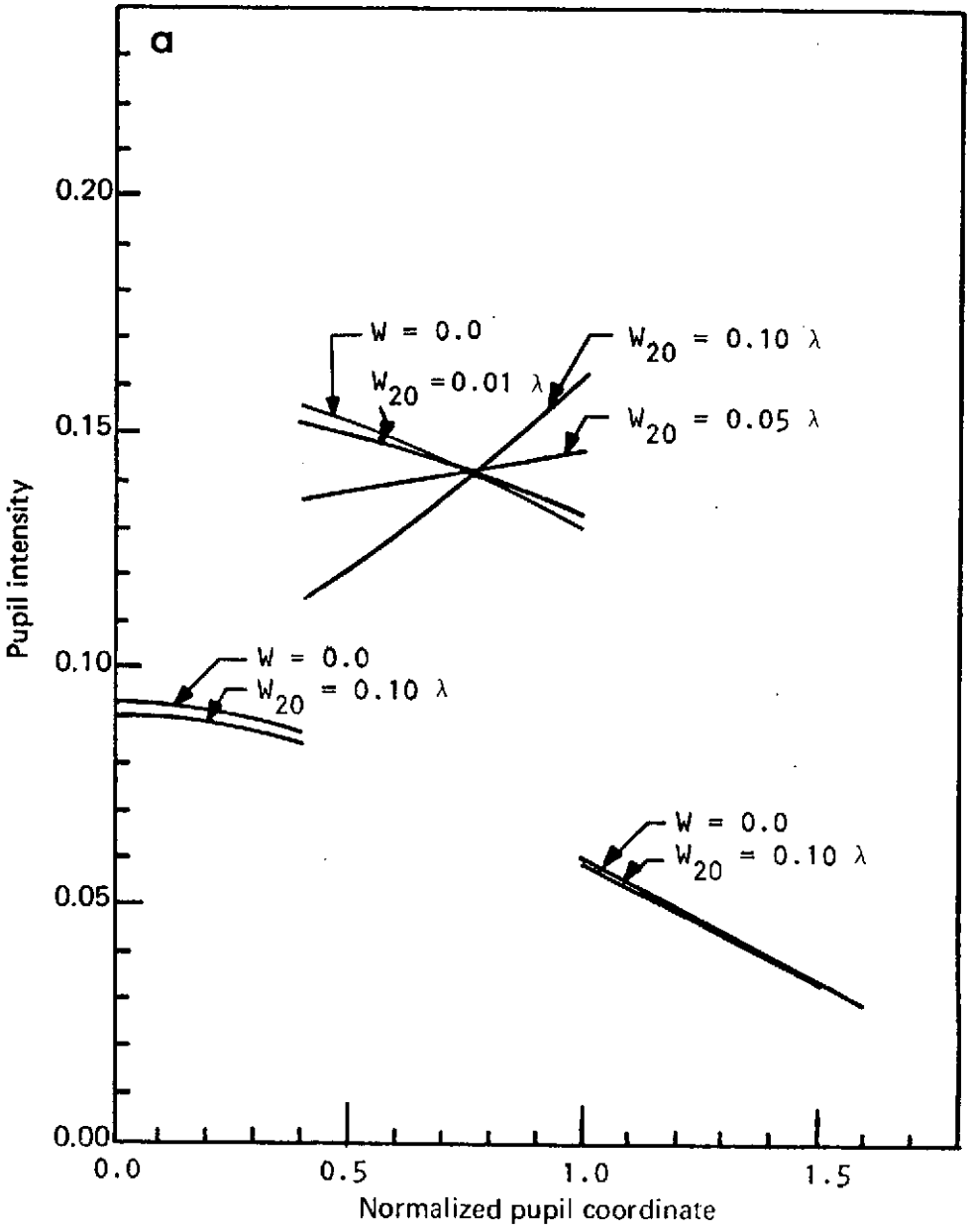

Fig. 23. Reimaged pupil with (a) defocus and (b) spherical aberration. $\lambda = 0.60$ μm, *F/No.* $= 12.000$, $b = 3.000$, $\varepsilon = 0.4000$, $\sigma = 0.206\ \lambda$, $T = 0.2605$.

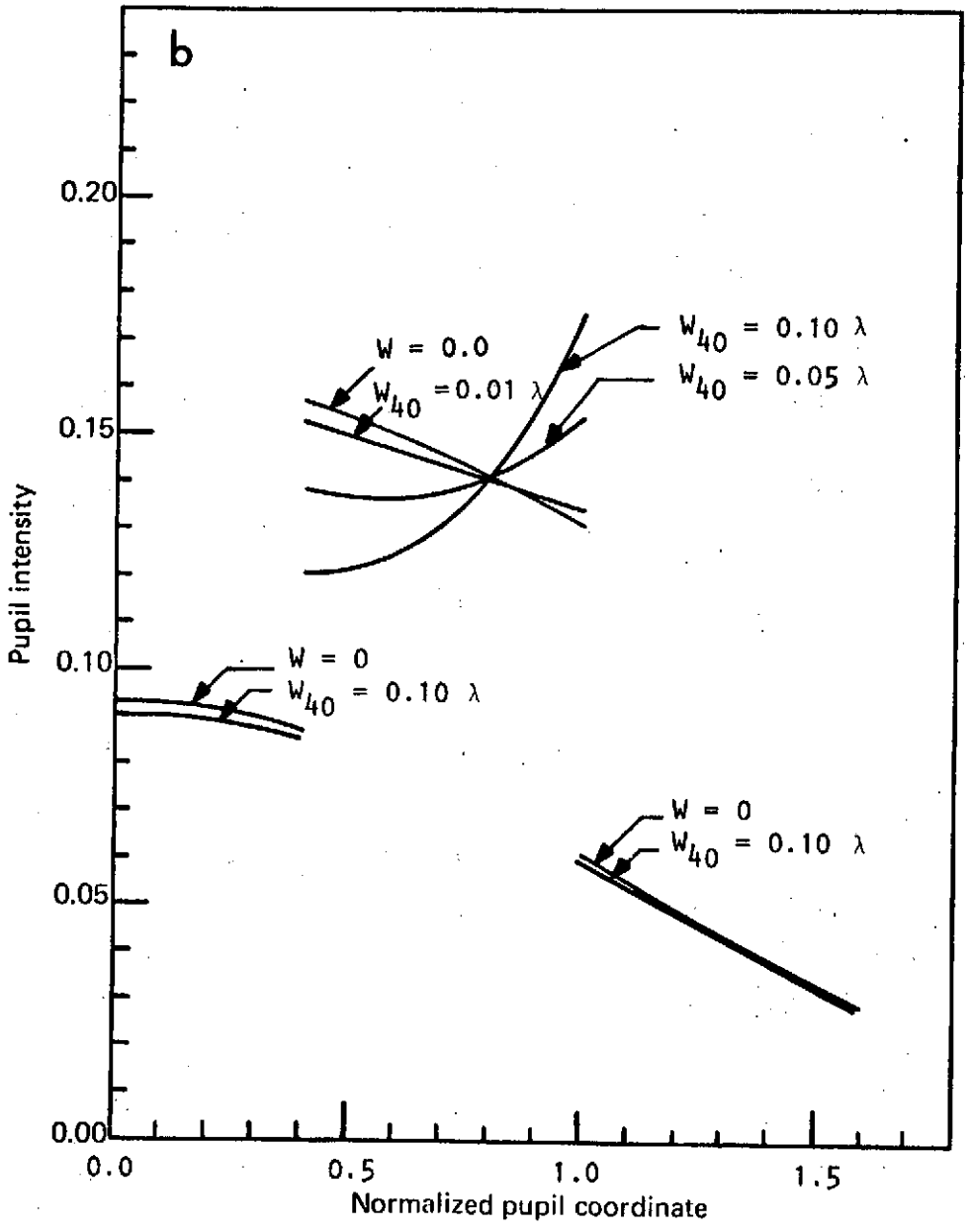

Fig. 23. (Continued).

Departures from the design values in the manufacturing process will result in two main effects. The first effect is a departure from maximum visibility, and the second effect will cause a shift in the zero-aberration operating point away from the zero condition. Figure 24 shows the effect on the visibility function V as a function of phase delay with three different transmission values. It can be seen that the visibility is indeed a slowly varying function and that for gross errors of phase delay and transmission its change is not significant.

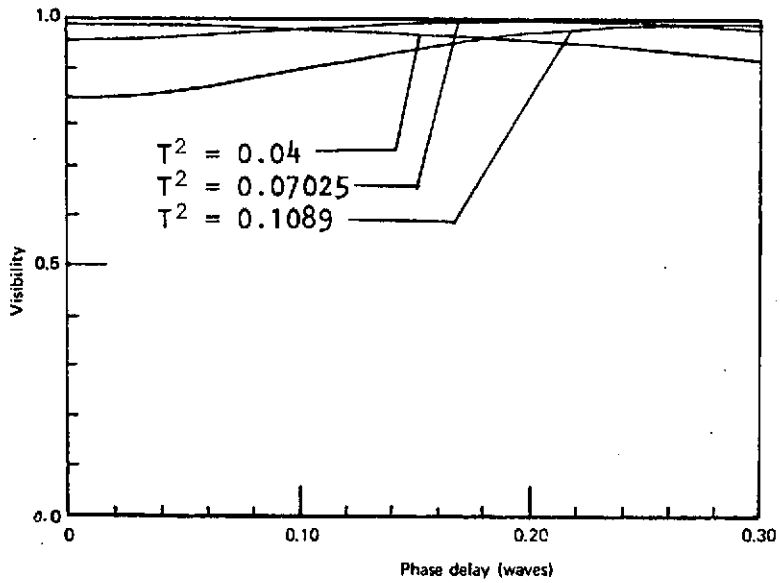

Fig. 24. Visibility as a function of phase delay. $\lambda = 0.6$, $\varepsilon = 0.4$, $b = 3$ μm.

The significant effect of fabrication errors is illustrated by Fig. 25. Here we can see the shift in the operating point (the point midway between the maximum and minimum of a fringe) due to departures in phase and transmission from the design values. For example, if the

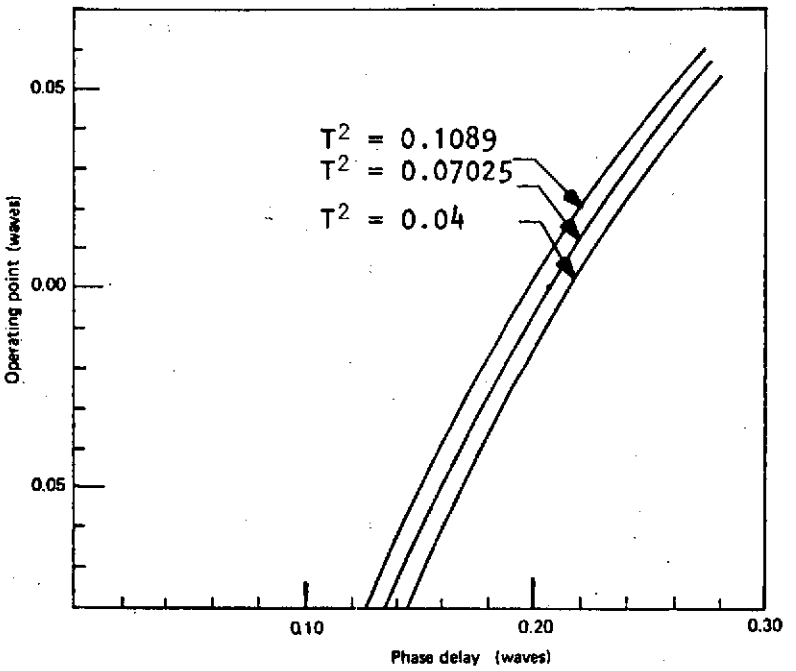

Fig. 26. Operating point as a function of phase delay. $\lambda = 0.6$, $\varepsilon = 0.4$, $b = 3$ μm.

phase delay upon manufacture was found to be 0.16 waves (instead of about 0.21 waves, which corresponds to the 0.00 operating point) the operating point has moved 0.05 waves from the symmetrical position. The range in one direction has thus been reduced from 0.25 λ to 0.20 λ. The prime purpose then of tight tolerancing will be to maintain a maximum range of operation (see Fig. 26). The other factor that influences our phase and transmission tolerancing is bandwidth. The shift in the operating point due to a finite bandwidth is $\pm \Delta\lambda/2\lambda_0$ at the edge of the bandwidth where λ_0 is the nominal design wavelength. In Table VI we have tabulated the effects of error in the manufacturing process on the range of operation for the Zernike disk. For the erosion process,

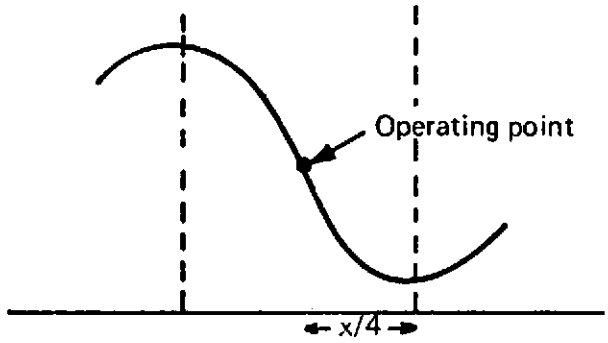

Fig. 26. Illustration of optimum operating point.

with careful control, and a 20-nm bandwidth the range of operation will be ± λ/8 in the worst case. For testing a well-corrected system the operating range can be reduced from ± 0.25 λ to a smaller range and the bandwidth can then be increased.

Table VI. Error budget for Zernike disk manufacture

Erosion range ± λ/8	Assign ± λ/120 transmission = ±2%
	± λ/10 phase delay = ± λ/5 erosion depth
	± λ/60 bandwidth = 20 nm

F. Signal-to-Noise Calculations

One can show that in making a measurement the statistical signal-to-noise ratio due to photon noise will be

$$S/N = \frac{(V)^{\frac{1}{2}}}{(2)^{\frac{1}{2}}} \frac{(AQTNatB)^{\frac{1}{2}}}{2\lambda F/No.}$$

where V, A, Q, T, λ, and F/No. are properties of the Zernike disk and the incident wavefront as defined before, N is the number of photons per sec per cm^2 per $\mathring{A}$ incident on the telescope entrance pupil, a is the pupil area sampled, t is the sampling time, and B is the bandwidth. For a Zernike disk designed for $\xi = 0$,

$$A^2 = 1 - T^2,$$

therefore,

$$S/N = \frac{(V)^{\frac{1}{2}}}{(2)^{\frac{1}{2}}} \frac{[T(1-T)^{\frac{1}{2}}QNatB]^{\frac{1}{2}}}{2\lambda F/No.}.$$

If we make two measurements of different phases, the percent change in signal will be equal to $V\Delta\phi$ for small phase changes $\Delta\phi$. The signal-to-noise ratio must be greater than $1/V\Delta\phi$. From this we can obtain an expression for the number of photons required to detect a phase change $\Delta\phi$

$$N = (NatB) = \frac{8\lambda^2 F/No.^2}{\Delta\phi^4 V^3 QT(1-T^2)^{\frac{1}{2}}}.$$

Figure 27 shows the minimum number of photons required to obtain $\Delta\phi$ = 0.01 λ, $\Delta\phi$ = 0.02 λ for various size Zernike radii.

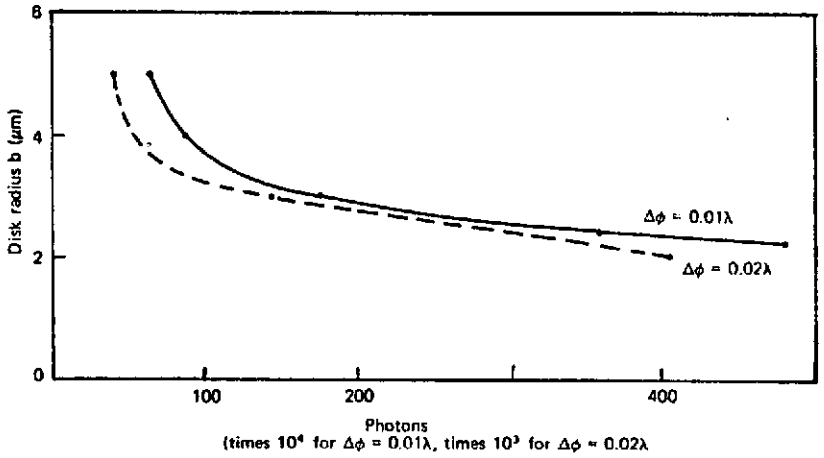

Fig. 27. Number of photons required to obtain S/N sufficient to measure $\Delta\phi$ (0.01 λ, 0.02 λ).

Assuming a collecting area a = 100 cm^2, a bandwidth of 20 nm, and an A_O type star, we have determined the integration times required for various star magnitudes. Figure 28a shows the star magnitude vs integration time per pupil point for $\Delta\phi$ = 0.01 λ for 3-μm and 4-μm radii Zernike disks, and Fig. 28b shows the same for $\Delta\phi$ = 0.02 λ. These calculations have assumed a *perfect* detector. For a real detector with a quantum efficiency of about 0.1, the photon requirement would have to be increased by a factor of 10, and the integration times would also have to be increased by a factor of 10. Thus, for reasonable collection

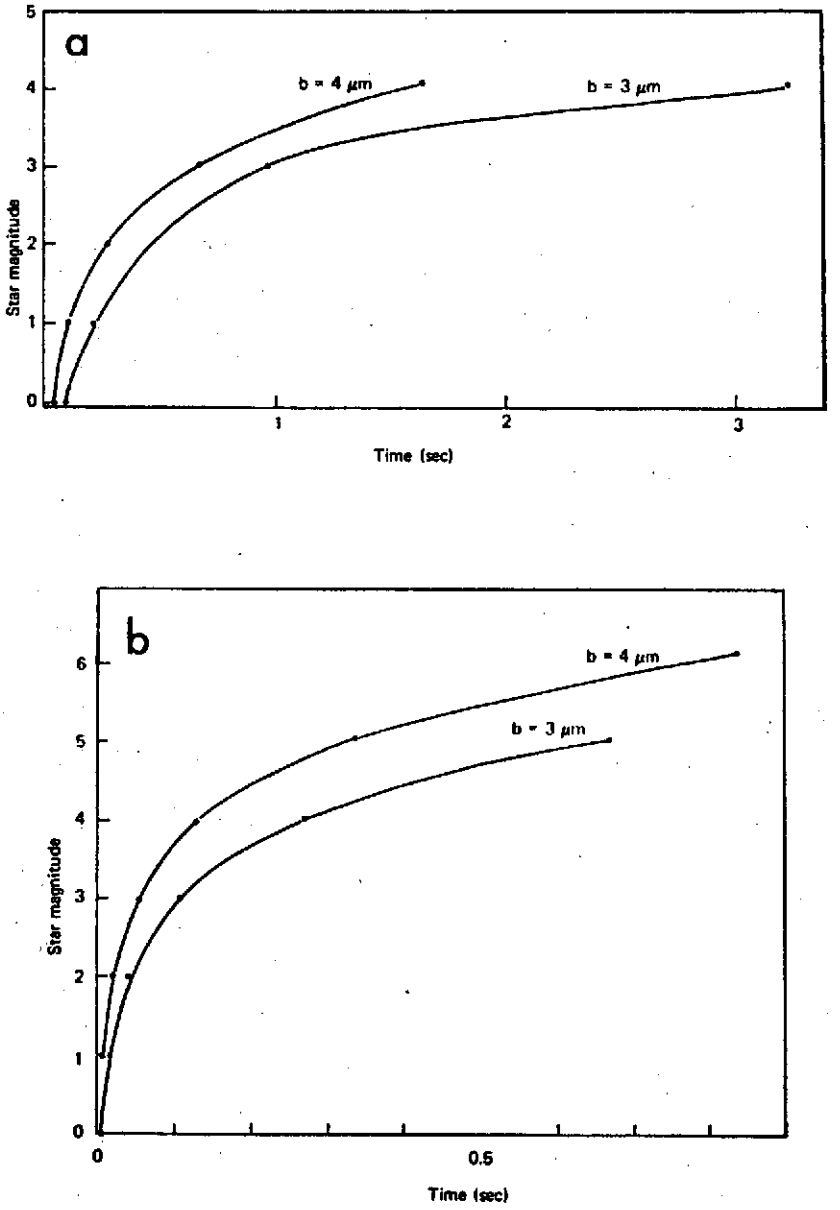

Fig. 28. Required star magnitude for (a) λ/100 detection and (b) λ/50 detection. A = 100 cm², Δλ = 200 Å, b = radius of Zernike disk.

times in a real system we are talking about star magnitudes of 0 or less for the Zernike test to resolve $\Delta\phi = 0.01\ \lambda$ over the full $\pm 0.25\ \lambda$ range.

g. Fabrication Process for Zernike Disks

Below is a step-by-step procedure for manufacturing a Zernike disk, a procedure that we developed in our clean area, solid-state circuitry facility. Much of the process is extremely sensitive to small dust particles, chemical contamination, and environmental controls. These factors all influence the success or failure of the process. In summary, dust must be minimized, care must be taken to avoid chemical contamination, and the temperature and humidity must be regulated in order to achieve repeatable results. Originally an aluminum coating was used. However, after doing a metal study, we found that chromium was a better choice for several reasons: (1) it coats better at our transmission values, (2) it is more resistant to the glass etch, and (3) it has a phase retardation effect rather than an advance, which significantly lowers the required glass etch depth.

i. Zernike manufacture (erosion method)

1. Clean substrate.
2. Coat with chromium to specified transmission.
3. Clean substrate.
4. Spin on photoresist
   Shipley: AZ-1350
   Spinner: ~ 5,000 rpm for 20 sec.
5. Bake at 75°C for 10 min.

6. Expose with mask in uv.
7. Develop in AZ-developer for 45 sec.
   a. (1:1 dilution).
   b. Rinse in deionized water.
8. Bake 20 min at 120°C.
9. Etch.
   a. Chromium etch.
      1:1.
      $HCl:H_2O$.
      ~ 60 sec.
      Initiate by contact with metal forceps.
   b. Glass etch. Rate (23°C): 0.46 μm/min.
      5:5:1 diluted to 1/8 strength with H_2O.
      $H_2O:NH_4F_2:HF$.
10. Photoresist removal.
    J-100 at ~80°C.
    Rinse in deionized H_2O.
    Dry - N_2.
11. Inspect.

ii. Zernike manufacture--metal phase shift effect

We have developed the equations that describe the optimum transmission and phase delays. Ideally we would like the phase delay to be introduced by the erosion process and the attenuation to be introduced by the aluminum coating. However, because of the complex index of refraction and finite thickness of the metal, we must make corrections to account for the phase delay introduced by the metal. We have calculated the *phase change* θ, introduced by the metal for various values of thickness d and also the transmission for various values of d. This information appears in Fig. 29. By referring to this graph and Table

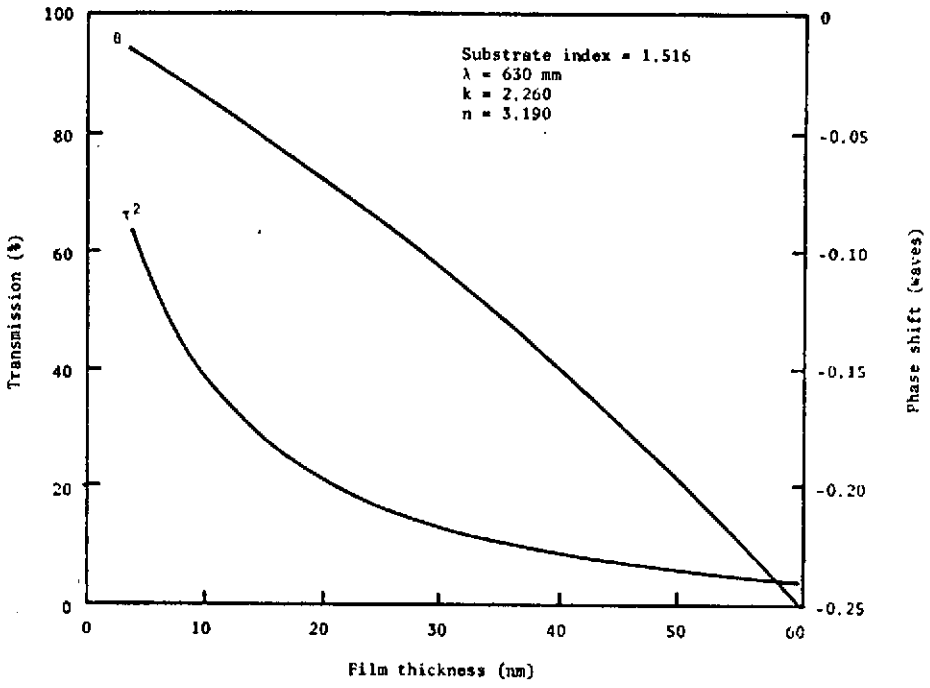

Fig. 29. Transmission, thickness, and phase shift for chromium films used in Zernike disk manufacture.

V for T^2 and σ we can calculate the required depth of erosion in our substrate using the equation

$$t = \frac{\theta + (d/\lambda) + \sigma}{n - 1}$$

where

θ = phase advance produced by chromium in waves

d = thickness of the chromium film

λ = wavelength

σ = required retardation in waves

n = index of refraction of substrate.

As an example for a 3-μm radius Zernike disk at 600 nm, we

require that T = 7%, and σ = 0.206 λ. From Fig. 29 we obtain θ = -0.17 λ and d = 45 nm. Taking n = 1.516 we obtain

$$t = \frac{-0.17 + (45/600) + 0.206}{0.516}$$

$$t \approx 0.215 \text{ waves (at 600 nm)}.$$

h. Experimental Evaluation

i. Laboratory experimental arrangement

In order to evaluate the sensitivity of the Zernike test, the configuration sketched in Fig. 30 was used. As a star source, a highly stabilized 20-nm-bandwidth white light source centered at 590 nm was used.

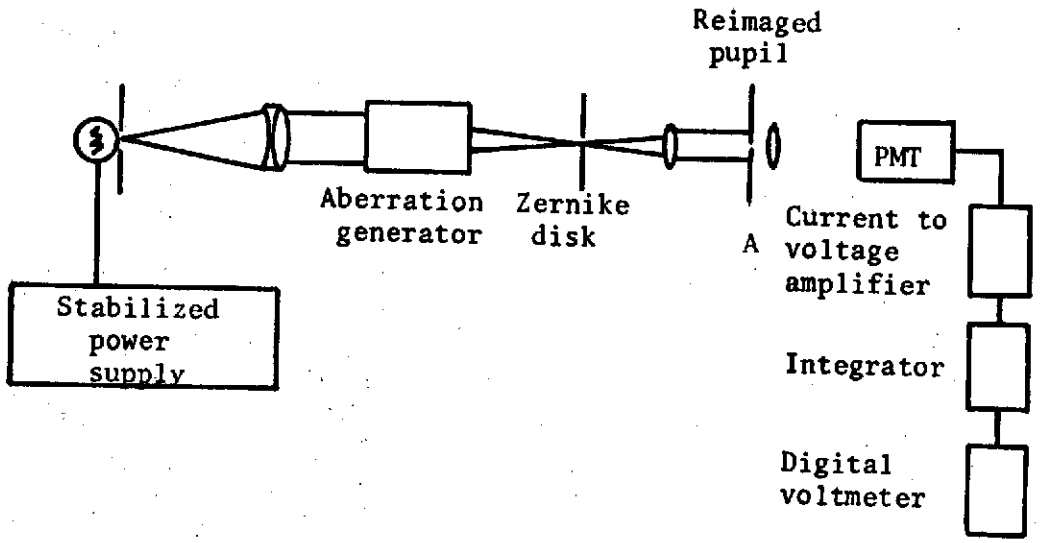

Fig. 30. Zernike test experimental arrangement.

The star source was imaged through the aberration generator onto the Zernike disk that was mounted on a three-axis, ultra-precision, highly stable slide. The lens following the disk reimaged the aberration generator pupil at A, where a 1.8-mm aperture was used to scan across the pupil. The energy through this aperture fell on the PMT creating an output current signal that was amplified and converted to a voltage signal, which was automatically integrated over a 10-sec period. This integrated value was then displayed on a digital voltmeter. This integration technique enabled us to average out most vibrational effects and other short-term variations.

Typical stability of light emitted from our lamp source with this scheme was better than one part in a hundred during an experiment.

ii. Manufactured Zernike disk parameters

Following the procedure outlined in the section on manufacturing, we produced a Zernike disk with the following properties:

Disk radius $b = 3.4\ \mu m$

Transmission $T^2 = 7\%$

Phase shift $\sigma = 0.19\ \lambda$.

The radius of the disk was measured using a filar eyepiece and calibration graticule and is correct to approximately $\pm 0.1\ \mu m$. The transmission of the coating was measured directly in the experimental arrangement described in the preceding section and is accurate to a small fraction of a percent. The phase shift σ was not entirely directly measured, but calculated from the complex index of refraction of chromium

and from the fringe shift measurement on the eroded sample. It is most likely that the error here is ± 0.04 λ.

iii. Generator adjustment

In order to evaluate the Zernike test in the small aberration range it was necessary to start with a system that was perfect to approximately λ/20 or better for the low-order aberrations. This was accomplished by stopping the aberration generator down to a resulting f/16 system. In the process the position of the spherical generator was changed to 49.2 mm as the nominal zero aberration setting.

iv. Experimental procedure

The purpose of this experiment was to determine the sensitivity of the Zernike test to measure small aberrations. First a baseline intensity scan of the pupil, reimaged through the Zernike disk, was made. Then, a small aberration was introduced, and the scan was repeated. The intensity values of these two runs were then subtracted and the data were plotted vs pupil position, with the central intensity change of the pupil always normalized to zero. The introduction of an aberration inevitably also introduced a small shift in the image position, which showed up on the data as a linear intensity variation. This term was removed and the resulting "de-tilted" data were used. Plotted on the same graphs we also included the predicted intensity changes for the introduced aberrations using the measured disk parameters. These are the plots illustrated in Figs. 31a through 31d for various amounts of defocus, coma, spherical aberration, and astigmatism.

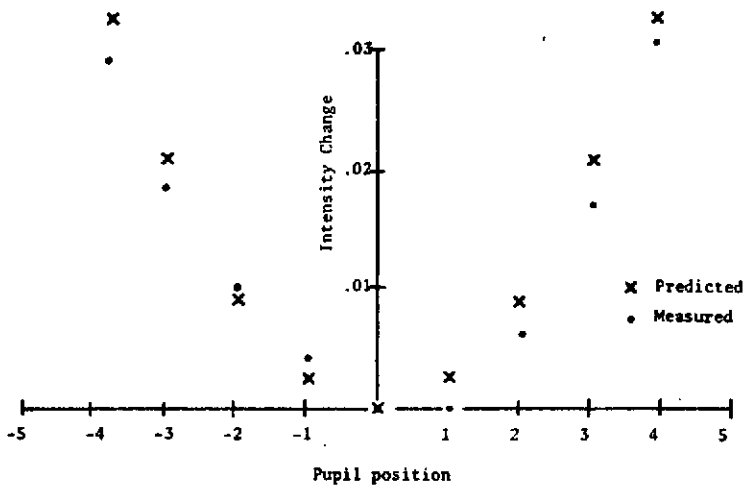

(a) Astigmatism. W_{22} = 0.102 λ at orientation θ = 33.0°. Predicted OPD is 0.043 λ at position 4.

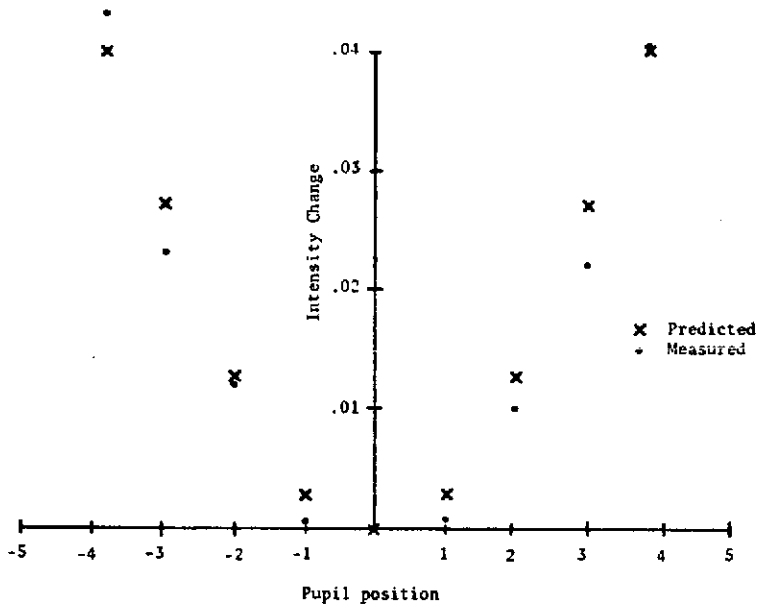

(b) Defocus. W_{22} = 0.08 λ. Predicted OPD is 0.051 λ at position 4.

Fig. 31. Reimaged pupil intensity change vs pupil position. F/No. = 16, λ = 590 nm, b = 3.4 μm, T^2 = 7.2%, σ = 0.19 λ.

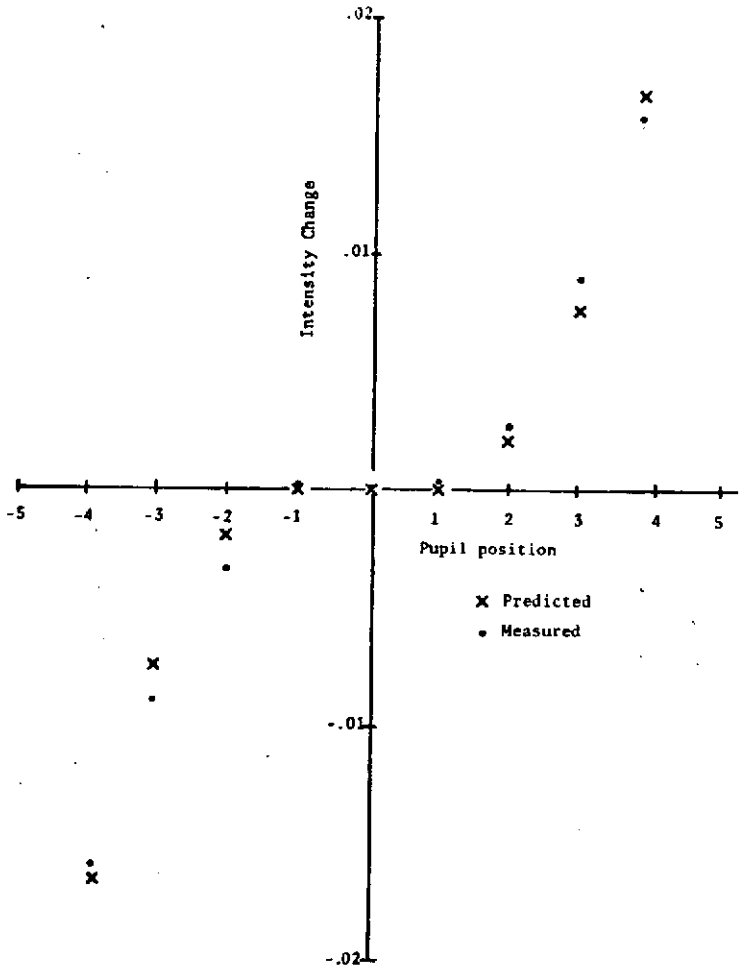

(c) Coma. $W_{31} = 0.0446\ \lambda$ at $\theta = 0^{\circ}$. Predicted OPD is $0.023\ \lambda$ at position 4. Note that the scale has been changed for the sake of clarity.

Fig. 31. (Continued)

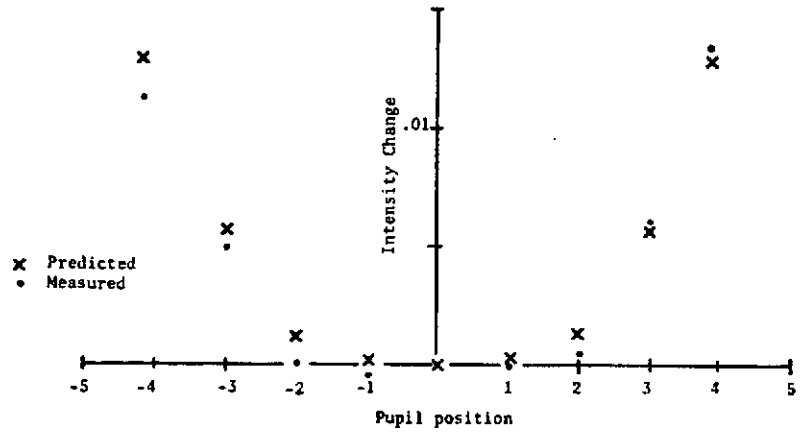

(d) Spherical aberration. $W_{40} = 0.0455\ \lambda$. *Predicted OPD is* $0.0176\ \lambda$ *at position 4. Note that the scale has been changed for the sake of clarity.*

Fig. 31. (Continued).

During the course of scanning the pupil, the image tended to drift slowly around the small vibrations that were averaged out through the integration scheme. This long-term drift was compensated by using the edge of the pupil as a reference intensity. Since the effect of image drift is a tilt aberration, the intensity effects are linear across the pupil. Thus, in order to compensate for tilt changes during a scan, one merely adds or subtracts a percentage of the edge reference intensity change; this percentage depends linearly on the pupil position. This very same procedure could be followed in an operational instrument to compensate for image motion.

v. Discussion of results

When inspecting Fig. 31a through 31d, it should be noted that the intensity change is the absolute percent energy change referred to the reimaged pupil. Since our light source was simulating a star with a magnitude of approximately 2, we would require integration times of approximately 5 sec at each point to satisfy statistical S/N relationships to obtain $\lambda/100$ sensitivity. We did, however, increase this time to 10 sec per point so that short-term laboratory vibrations and air turbulence could be averaged out more satisfactorily.

As we inspect each of the graphs, we see that all points agree with predicted values better than 0.01 λ with an rms error of 0.003 λ over all data collected. This degree of accuracy is actually beyond the calibration accuracy of the laboratory wavefront error simulator ($\lambda/100$). We can thus conclude that the Zernike test has sensitivity capabilities exceeding $\lambda/100$ and that the theory of operation developed here and the fabrication techniques are adequate for use to better than $\lambda/100$.

2. Polarization Interferometers

a. General Discussion

Polarization interferometers have generally been used up to now as devices for creating fringes. We can gain maximum sensitivity by taking phase information and converting it into states of linear polarization using a sensor that can read out the polarization state and thus obtain a phase reading. An instrument with a polarization readout in a Twyman-Green configuration has been built at the Optical Sciences Center

and has demonstrated sensitivities of $\lambda/500$. This is to be compared with a $\lambda/50$ sensitivity of the traditional two-beam fringe reading Twyman-Green interferometer. The Twyman-Green instruments, of course, operate with an artificial source that generates a nearly perfect reference wave. Since we are using a real star source we have to generate our own reference. Two possibilities are (1) the use of some sort of polarization pupil shearing technique, such as the lateral shear, which we have chosen for laboratory purposes or (2) the use of a method similar to the Zernike phase test, except operating in a polarizing sense, which can generate its own nearly perfect reference wave. The first concept we call the shearing polarization interferometer and the second the Zernike polarization disk interferometer.

b. The Shearing Polarization Test

There are many types of shear (lateral, radial, inverting, etc.) that can be used to produce interference effects between two points in the pupil of an optical system. For laboratory simplicity we have chosen to illustrate, analyze, and construct a polarizing lateral shearing device. The basic idea is as follows: In Fig. 32a we have the exit pupil of the system, which, in general, will be in some partially polarized state. We then reimage this pupil at C through the polarizing interferometer as follows. By means of a polarizer we put the wavefront into a linear polarized state. This linear polarized pupil is then operated on by a series of optical elements to produce at C two images of the system exit pupil slightly displaced from one another such that one image is

right-circularly polarized and the other image is left-circularly polarized. If we now look at a point in the sheared pupil image we have light right-circularly polarized from point A interfering with light left-circularly polarized from point B. If point A has phase Δ_A and point B has phase Δ_B, the two oppositely-circularly polarized coherent beams combine to produce a linearly polarized beam such that

$$\psi = (\Delta_A - \Delta_B)/2,$$

where ψ is the direction of linearly polarized light. This is illustrated in Fig. 32b. We now use some sort of device to detect this linear polarization state and thus obtain a direct measurement of the sheared phase $(\Delta_A - \Delta_B)$ across the pupil.

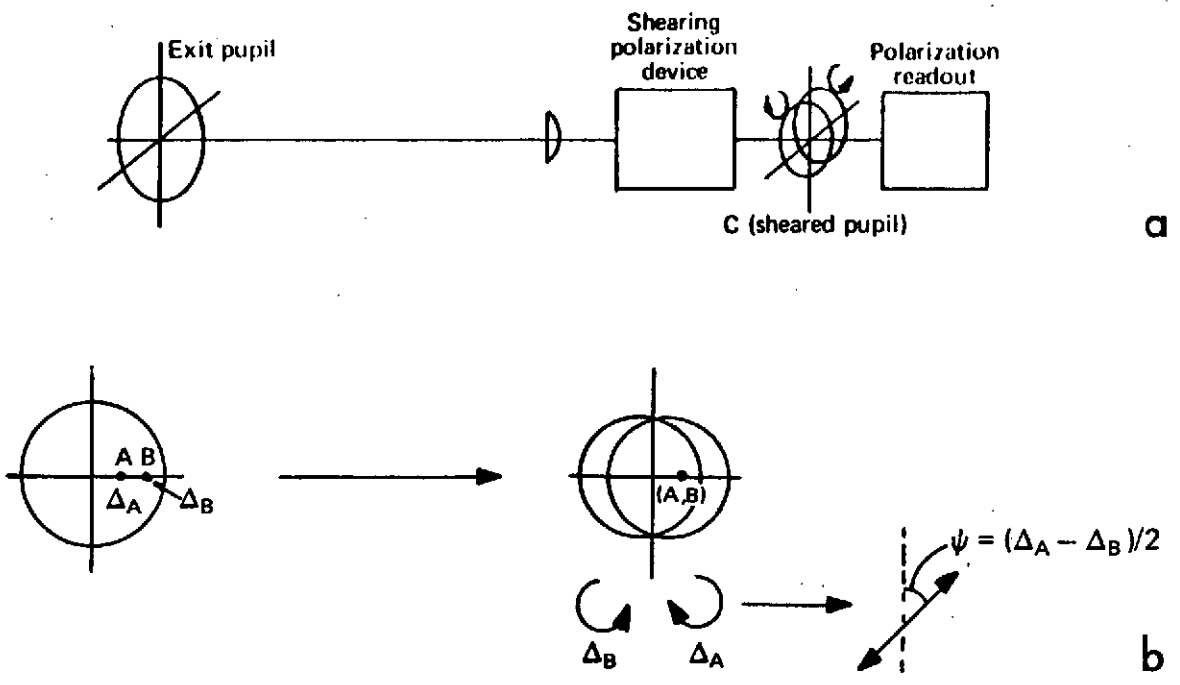

Fig. 32. Polarization shearing concepts.

i. Ways of producing the sheared polarization states

There are many possible ways of obtaining the desired orthogonal circularly polarized sheared pupil condition at point C. Several of these are illustrated below with some brief comments.

Figure 33 shows a neat, compact unit where the shear in the pupil is produced by displacement of the two halves of the modified pentaprism along the polarizing beamsplitter plane A-B. Plane polarized light at 45° is then passed through the prism and sheared into two orthogonal states of polarization. These two orthogonal states then emerge at D where they pass through an achromatic quarter-wave plate at 45°, which in turn yields two oppositely-circularly polarized pupils at plane C. We have a compact unit where the shear is easily varied from zero to any value by movement along A-B. We require manufacture using very low birefringence glass so as to maintain linear polarization states. For greater stability one could replace the second right angle prism with another prism. The above arrangement is achromatic in collimated light.

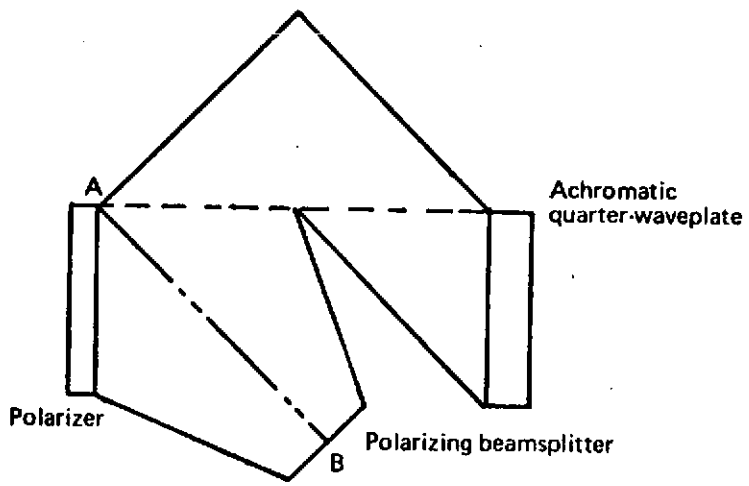

Fig. 33. Pentaprism polarization shearing device.

Figure 34 shows a compact way to obtain circularly-polarized light by using two Wollaston prisms. The amount of shear is controlled by the separation of the two matched prisms with the scaling factor set by the prism angle θ. The advantage of the unit is that it is naturally achromatic and compact. However, the disadvantages are that it is not able to go to zero shear, and the large separation D required for large shears may result in uncompensated path differences and coherence length problems. This device appears most suitable for a small, fixed, shear mode where the two prisms are made into a single unit. In this case we have a single, compact, shearing mechanism.

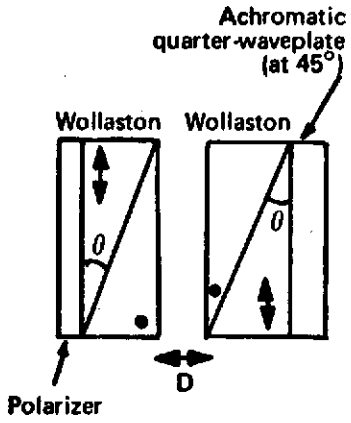

Fig. 34. Double Wollaston prism polarization shearing device.

In Fig. 35 we have a polarizing beamsplitter A-B. The shear is introduced by tilting a right angle prism about axis O. The shear is given by

$$S = 2t \sin u \left[1 - \left(\frac{1 - \sin^2 u}{n^2 - \sin^2 u}\right)^{1/2}\right]$$

where t is the total thickness of the upper prism, u is the tilt angle, and

$$S = 2tu\left[\frac{n - 1}{n}\right]$$

for small values of u.

In this case we can vary our shear from zero upwards. However, at large shears the variation is very nonlinear, and wavelength-dependent shear effects can be large. Low birefringence glass is required.

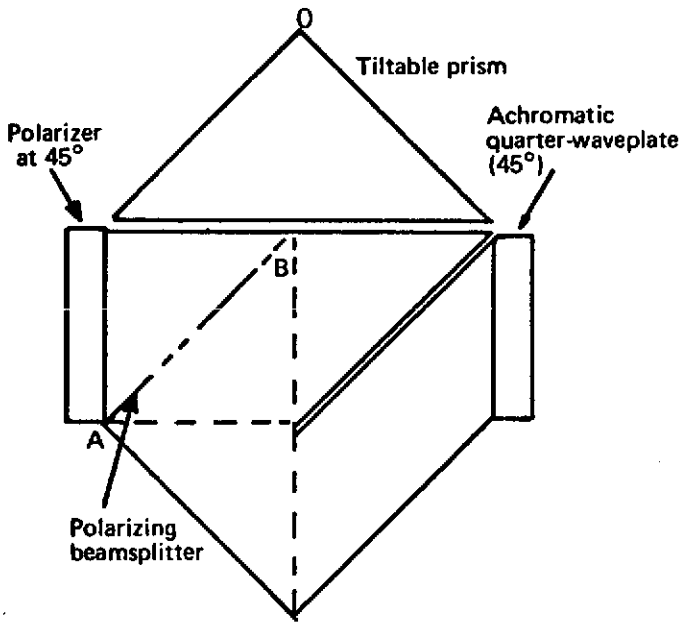

Fig. 35. Polarizing beamsplitter tiltable prism polarization shearing device.

In the simple arrangement shown in Fig. 36, a Wŏllaston prism is placed at the system focus. We have a fixed shear determined by the prism angle θ. Lens B will affect the polarization orthogonality of the shear, and the arrangement is very sensitive to positioning of the prism. The shear itself is no longer achromatic.

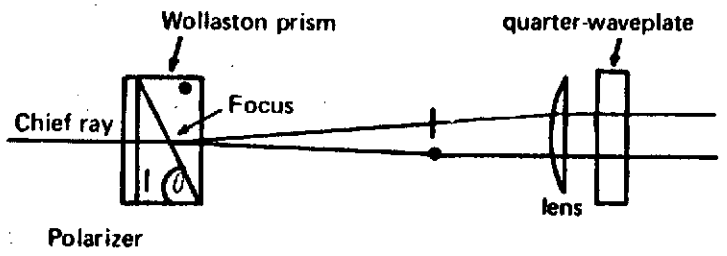

Fig. 36. Single Wollaston prism polarization shearing device.

There are other ways of introducing orthogonally-polarized sheared pupils either with birefringent materials or by using polarizing beamsplitters with tiltable glass plates or mirrors. Of the concepts presented, the first would be preferred based on its maximum versatility and simplicity. The second would be preferred based on its simplicity with limited versatility. For laboratory purposes and since we could use off-the-shelf components, we have designed our shearing unit about this second concept.

c. Ways of Reading Out Polarization States

We discuss here two possible ways of reading out polarization states.

i. Single rotatable Wollaston prism

Assuming we have produced two oppositely-circularly polarized sheared pupil images at C in Fig. 32, we know that these two coherent beams combine to produce a state of linear polarization where the angle is

$$\psi = \frac{\Delta_A - \Delta_B}{2} .$$

Behind this we position a Wollaston prism and a decollimating lens D, as shown in Fig. 36. If the original zero aberration position of the Wollaston prism is at 45°, we rotate this prism until the two oppositely-polarized intensities are equal. We can measure these intensities by use of an image dissector tube with deflection coils, in a synchronous amplification scheme (Fig. 37). We would thus rotate the Wollaston toward a null signal and encode the rotation, where a rotation of 1/60 rad (~1°) corresponds to a phase measurement $\Delta_1 - \Delta_2$ of ~ $\lambda/190$.

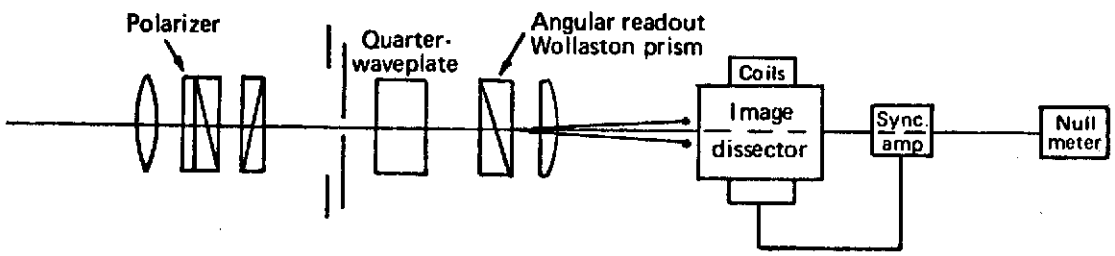

Fig. 37. Single channel polarization readout with image dissector.

We have chosen to simulate this scheme in the laboratory because of its simplicity. However, instead of using an image dissector we simulate the dissector with two counter-rotating prisms as illustrated in Fig. 38. We thus sequentially sample one of two beams at 28 Hz and synchronously amplify the difference signal. The Wollaston prism is rotated until this signal is minimized and this rotation is recorded.

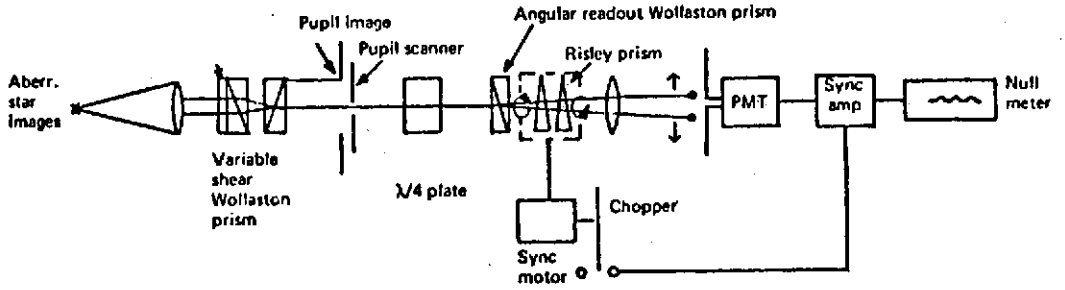

Fig. 38. Laboratory simulation of shearing polarization interferometer.

ii. The two-channel device

If we use the optical arrangement illustrated in Fig. 39, we get difference signals in each channel. In channel one, with the quarter-wave plate fast axis located at +45°, we obtain a sinusoidally modulated signal where $\Delta I_1 = I_1 - I_2 = K \sin(\Delta_1 - \Delta_2)$ and in channel two with the quarter-wave plate fast axis oriented at -45° we obtain $\Delta I_2 = K \cos(\Delta_1 - \Delta_2)$. The circuits are balanced for equal gain. Then the signals are divided so that

$$\Delta I_1/\Delta I_2 = \tan(\Delta_1 - \Delta_2),$$

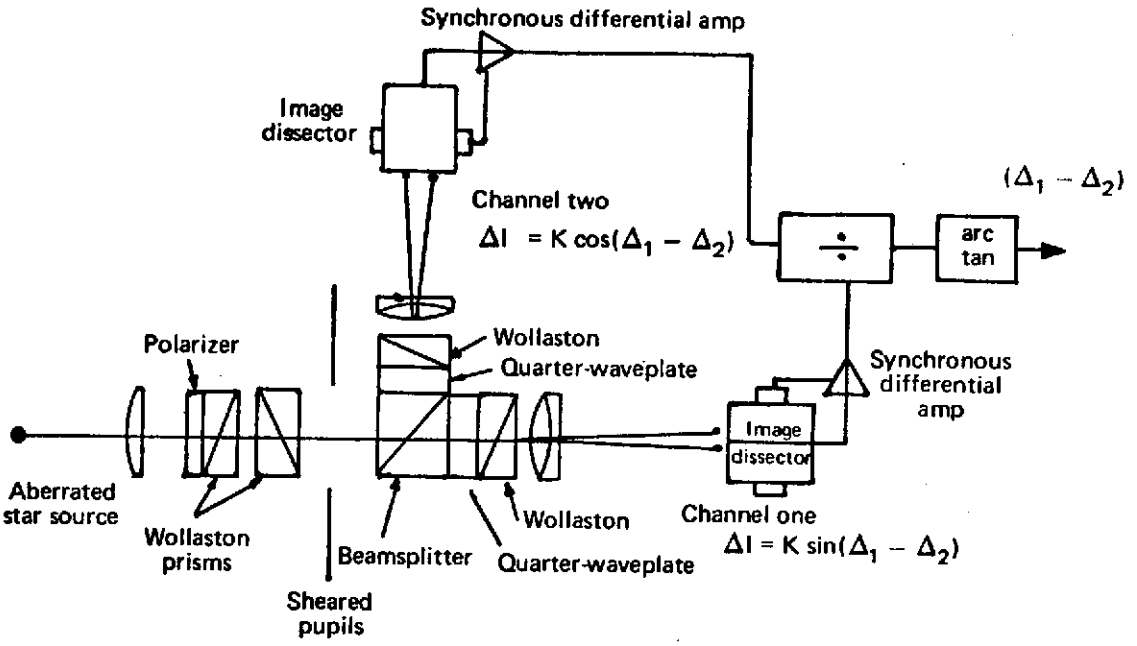

Fig. 39. Two-channel shearing polarization interferometer.

and then the arc tan $(\Delta I_1/\Delta I_2)$ is taken. All of this is done electronically without the need for movement of any components. As with the other scheme it is insensitive to source fluctuations. This type of readout has been utilized in a Twyman-Green configuration instrument constructed at the Optical Sciences Center, and phase errors of $\lambda/500$ have been measured.

d. Discussion of the Polarization Intensity Equations Including Alignment and Fabrication Errors

Below we derive expressions for the intensities of the sheared pupil signals as a function of (1) unbalanced signal amplitudes between two polarization states, (2) angular positioning of components, and (3) departure from perfect quarter-wave plate delay.

Let us assume that the polarizer-shearing combination produces a shear in the y direction, as illustrated in Fig. 40, where the amplitude of one polarization is

$$E_{\perp}\, e^{i\Delta[x,y - (S/2)]}$$

and the other is

$$E_{||}\, e^{i\Delta[x,y + (S/2)]},$$

where S is the total shear.

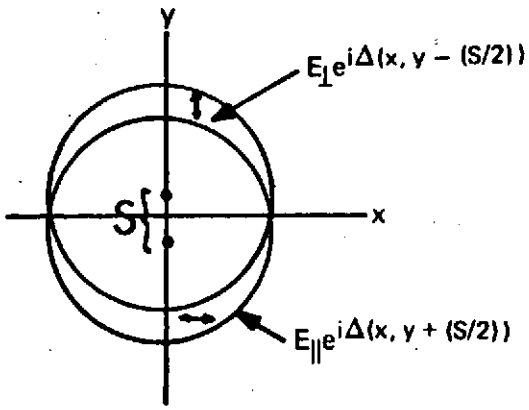

Fig. 40. Sheared pupil geometry.

These signals then pass through the quarter-wave plate (Fig. 41) oriented at some angle θ with respect to the x axis. (Ideally $\theta = \pm 45^{\circ}$, depending of whether we desire sine or cosine modulation, as discussed in the previous section.) The plate advances the phase by $(\pi/2) + \delta$ for the fast axis over the slow axis.

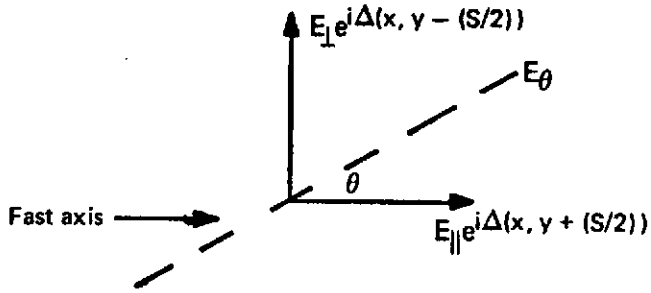

Fig. 41. Signal component passing through quarter-wave plate.

The field passing through the fast axis is

$$E_\theta = e^{i[(\pi/2) + \delta]}\left[E_\perp e^{i\Delta[x,y - (S/2)]}\sin\theta + E_\parallel e^{i\Delta[x,y + (S/2)]}\cos\theta\right].$$

The field passing through the slow axis direction is

$$E_{\theta+90^\circ} = E_\parallel e^{i\Delta[x,y + (S/2)]}\sin\theta - E_\perp e^{i\Delta[x,y - (S/2)]}\cos\theta.$$

We now orient a Wollaston prism at an angle ψ with respect to the x axis (Fig. 42). Light through this prism then produces one signal polarized in the ψ direction and another polarized at $\psi + 90^\circ$.

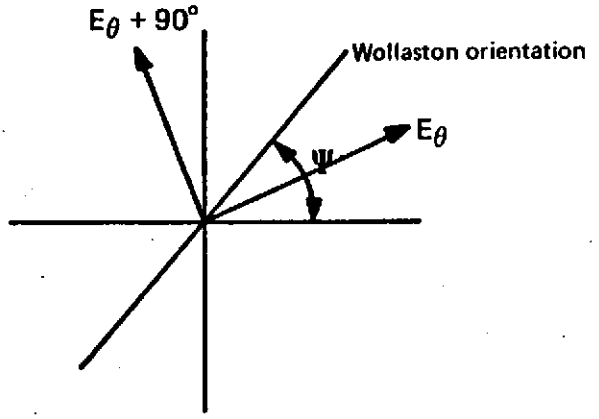

Fig. 42. Signal component passing through a Wollaston prism.

The output through the Wollaston is thus

$$I_\psi = E_\psi E_\psi^* = |E_\theta|^2 \cos^2(\theta-\psi) + |E_{\theta+90}|^2 \sin^2(\theta-\psi)$$

$$+ 2\mathrm{Re}\ E_\theta E_{\theta+90}\ \cos(\theta-\psi)\sin(\theta-\psi)$$

$$I_{\psi+90°} = E_{\psi+90} E_{\psi+90}^* = |E_{\theta+90}|^2 \cos^2(\theta-\psi)$$

$$+ |E_\theta|^2 \sin^2(\theta-\psi)$$

$$- 2\mathrm{Re}\ E_\theta E_{\theta+90}\ \cos(\theta-\psi)\sin(\theta-\psi).$$

We now substitute for E_θ, and $E_{\theta+90}$ and assume δ is small so that

$$e^{i(\frac{\pi}{2} + \delta)} \approx i - \delta.$$

This yields

$$I_{\psi} = [(E_{\perp}^2 \sin^2\theta + E_{||}^2 \cos^2\theta + E_{\perp}E_{||} \sin 2\theta) \cos^2(\theta - \psi)$$

$$+ (E_{\perp}^2 \cos^2\theta + E_{||}^2 \sin^2\theta - E_{\perp}E_{||} \sin 2\theta) \sin^2(\theta - \psi)] \cos\Delta$$

$$- E_{\perp}E_{||} \sin(2\theta - 2\psi) \sin\Delta$$

$$+ \delta\left[(E_{\perp}E_{||}) \cos\Delta - (E_{||}^2 - E_{\perp}^2) \frac{\sin 2\theta}{2}\right] \sin(2\theta - 2\psi)$$

$$I_{\psi+90^\circ} = (E_{||}^2 \sin^2\theta + E_{\perp}^2 \cos^2\theta - E_{\perp}E_{||} \sin 2\theta) \cos^2(\theta - \psi)$$

$$+ (E_{||}^2 \cos^2\theta + E_{\perp}^2 \sin^2\theta + E_{\perp}E_{||} \sin 2\theta) \sin^2(\theta - \psi) \cos\Delta$$

$$+ E_{\perp}E_{||} \sin(2\theta - 2\psi) \sin\Delta$$

$$- \delta\left[E_{\perp}E_{||} \cos\Delta - (E_{||}^2 - E_{\perp}^2) \frac{\sin 2\theta}{2}\right] \sin(2\theta - 2\psi).$$

We now substract the two signals

$$I_{\psi+90^\circ} - I_{\psi} = 2E_{\perp}E_{||} \sin\Delta \sin(2\theta - 2\psi)$$

$$- 2E_{\perp}E_{||} \sin 2\theta \cos\Delta \cos(2\theta - 2\psi)$$

$$- \delta\ E_{\perp}E_{||} \cos\Delta - (E_{||}^2 - E_{\perp}^2) \frac{\sin 2\theta}{2} \sin(2\theta - 2\psi).$$

i. Possible operating conditions for two-channel device

Neglecting δ for the present, if

		(Condition 1)
$\theta = 45^\circ$, $\psi = 0$	$\theta = 0$, $\psi = 45^\circ$	
$\Delta I = 2E_{\perp}E_{||} \sin\Delta$	$\Delta I = 2E_{\perp}E_{||} \sin\Delta$	

If

$\theta = -45^\circ, \quad \psi = -45$	$\theta = -45^\circ, \quad \psi = -45^\circ$	*(Condition 2)*
$\Delta I = 2E_\perp E_{\|\|} \cos\Delta$	$\Delta I = 2E_\perp E_{\|\|} \cos\Delta$	

We see we have two possible operating conditions for the two-channel device.

ii. Departure from perfect quarter-wave plate

In the one-channel device ψ is rotated until $\Delta I = 0$, or

$$\tan\Delta = \frac{1}{\sin 2\theta} \tan(90 - 2\theta + 2\psi) + \delta - \frac{(E_{\|}^2 - E_\perp^2)\delta}{2E_\perp E_{\|} \cos\Delta} .$$

With the orientation of the quarter-wave plate fast axis at $\theta = 45^\circ$, as far as tolerancing on δ goes, we see that for small phase errors the second error term will be a small fraction of the first. We can manufacture a quarter-wave plate with $\delta \simeq 1/100$ or less over 1000 Å bandwidth; i.e.,

$$\bar{\delta}_{ave} << \frac{1}{100} \text{ and } \tan \quad = \tan 2\psi + \delta.$$

The effect on small phase errors $\Delta \simeq \lambda/200$ will be to introduce a constant offset error $\bar{\delta}$, the constant offset being less than $\pm \lambda/500$. This constant correction would hold beyond Δ becoming somewhat greater than $\lambda/20$. Beyond this, the correction would get smaller for larger aberrations. If it were desired one could measure δ over the passband of the instrument and determine the average δ, which is $\bar{\delta}$, and compensate for measured values.

iii. Alignment of quarter-wave plate

Now let us examine small errors in θ and $\Delta\theta$ when $\theta = 45^\circ \pm \Delta\theta$

$$\tan\Delta = \frac{1}{\cos(90 - 2\Delta\theta)} \tan(90 - 2\theta + 2\psi)$$

$$\tan\Delta = \frac{1}{\cos(2\Delta\theta)} \tan(2\psi - 2\Delta\theta).$$

The $\cos(2\Delta\theta)$ effect is negligible for small $\Delta\theta$ of a few degrees, therefore,

$$\tan\Delta = \tan(2\psi - 2\Delta\theta)$$

$$\Delta = 2\psi - 2\Delta\theta.$$

We see that the effect of the quarter-wave plate misalignment is to introduce a constant bias of $2\Delta\theta$ in the measurements, if $\Delta\theta$ is kept to $\pm 2^\circ$.

e. Bandwidth Considerations

i. General discussion

If $\theta = 45^\circ$, we arrive at an error signal

$$\Delta I = I(\lambda) \sin(\Delta - 2\psi)$$

where $\Delta = (2\pi/\lambda)x$ and x is the physical path difference between the sheared points. If we let $K = 2\pi/\lambda$, then $\Delta = Kx$ and

$$\Delta I = I(K) \sin(Kx - 2\psi)\Delta K$$

for monochromatic radiation of bandwidth ΔK.

If we have a bandwidth of $\pm \Delta K/2$ and if we take into consideration the weighted spectral response of the detector, the shape of the bandpass filter, and the distribution of the radiation, we obtain an integrated effect. If the weighted function is symmetric about a K_{ave} we will show below that

$$\Delta I = \sin(K_W x - 2\psi) F(x, B(K), S, R) \Delta K$$

where K_W is the weighted average wave number and $F(x, B(K), S, R)$ is a function depending on the spectral distribution S, responsivity R, bandpass filter function B(K), and x.

It is desirable to have $F \sim 1$ and to have a much slower varying function of x than the sine function. If we consider the case of narrow bandwidths S, R can be assumed constant. If we take ΔK to be a square bandpass filter we find that

$$\Delta I = \sin(K_{ave} x - 2\psi) \operatorname{sinc} x \Delta K \Delta K.$$

If $\Delta\lambda = \pm 250$ Å, and for the range of x, $Kx \simeq 0$, then

$$\operatorname{sinc} x \Delta K \simeq \text{constant} \simeq 1,$$

and

$$\Delta I \simeq \sin(K_{ave} x - 2\psi) \Delta K$$

for a narrow band where

$$K_{ave} = \frac{K_{max} + K_{min}}{2}.$$

ii. General theory

In Fig. 43 F(K) represents the spectral energy distribution multiplied by the filter response multiplied by the detector response. The error signal for a setting ψ of our readout prism is

$$\Delta I = \int_{K_1}^{K_2} F(K)\sin(Kx - 2\psi)dK.$$

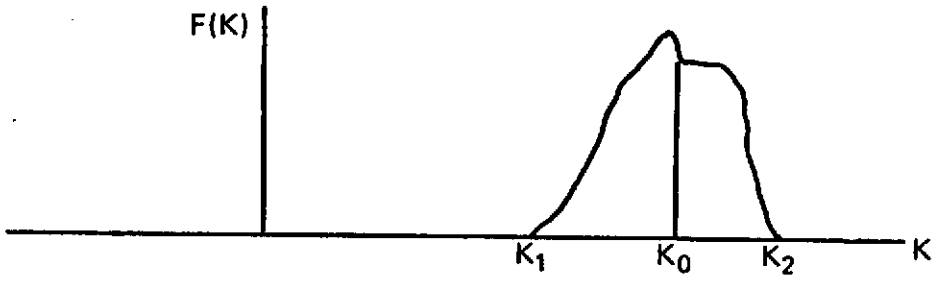

Fig. 43. Effective spectral energy distribution.

In the monochromatic case we have seen that $\Delta I = 0$ if $2\psi = Kx$. We would like to see the effect of this general radiation function F(K) on our error signal ΔI

$$\sin(Kx - 2x) = \frac{1}{2i}\left(e^{iKx}\, e^{-i2\psi} - e^{-iKx}\, e^{i2\psi}\right)$$

therefore,

$$\Delta I = \frac{1}{2i}\, e^{-i2\psi} \int_{K_1}^{K_2} F(K)e^{iKx}dK - e^{i2\psi} \int_{K_1}^{K_2} F(K)e^{-iKx}dK$$

$$\Delta I = \text{Imaginary part of } e^{-i2\psi} \int_{K_1}^{K_2} F(K) e^{iKx} dK$$

$$\Delta I = \text{Im } e^{i(K_0 x - 2\psi)} \int_{-(K_1 - K_0)}^{K_2 - K_0} F(K) e^{iKx} dK \ .$$

Here we have used the fact that F(K) is real, and the shift theorem of Fourier transforms, where K_0 is the weighted average

Now F(K) can be written as the sum of an even and odd function.

$$F(K) = EF(K) + OF(K)$$

$$\Delta I = \text{Im } e^{i(K_0 x - 2\psi)} \int (EF(K) e^{iKx} dK + \int OF(K) e^{iKx} dK \ .$$

The Fourier transform of an even function is real and even, and the Fourier transform of an odd function is imaginary and odd. Thus we obtain

$$\Delta I = \sin(K_0 x - 2\psi) F(EF) + i \cos(K_0 x - 2\psi) \ F(OF),$$

where F denotes Fourier transform.

We note that for any even distribution function our error signal is of the same functional form as in the monochromatic case, where K_0 is the weighted average wave number. In the case of a nonsymmetric distribution, the odd part of the distribution will cause in general an inability

to obtain the null condition at $K_0x - 2\psi = 0$. The condition for nulling now becomes

$$\tan(K_0x - 2\psi) = -\frac{iF(OF)}{F(EF)} \qquad \text{(relationship A)}.$$

In general we can thus make the bandwidth large if we take the spectral distribution function F(K) and correct for the null condition.

In particular we have our highest sensitivity requirement in the vicinity of $x \simeq 0$. In this region $F(OF) \simeq 0$, and we have $2\psi = K_0x$, the monochromatic condition, as a solution above, and $F(EF)$ only lowers the signal-to-noise ratio.

iii. Summary

In summary, our polarization interferometer can be used as a "white light" interferometer under the following conditions:

(1) In the near zero aberration area with no corrections on the monochromatic case provided we use $K = K_0$.

(2) In the larger aberration area, with no corrections, if the asymmetry of the distribution is small. For example, if

$$\left| \frac{iF(OF)}{F(EF)} \right| \leq \frac{1}{60},$$

we would have $\lambda/200$ error. We also assume $F(FE) \simeq 1$.

(3) In the larger aberration area if the spectral characteristics are known and we make corrections as provided by relationship A, or if we are willing to accept lower

accuracy for the larger aberration measurements, where the above relationship determines the measurement degradation if we know our distribution and sensitivity functions.

f. Signal-to-Noise Ratio

In order to resolve a small change in signal we want the S/N ratio to be greater than the ratio of signal to change in signal, produced by a phase difference, $I/\Delta I$. For a very high degree of confidence (99% or 3 σ), we require that $S/N > 3I/\Delta I$. For Δ small, $\psi \simeq 0$, $\theta = 45^{o}$, and $\Delta I \simeq I\Delta$. Therefore, $I/\Delta I = 1/\Delta$ and $S/N > 3/\Delta$. The signal-to-noise ratio results from taking *two* measurements on an approximate equal number of photons

$$S/N = [(\text{Number of photons})^{\frac{1}{2}}/(2)^{\frac{1}{2}}] \times DQE$$

where

Number of photons = NatB·E

N = number incident per unit time per Å per sec ≃ 1000

a = collecting area ≃ 100 cm^2

B = bandwidth ≃ 500 Å

E = polarizer effect = 0.5 (linear polarizer efficiency)
× 0.5 (Wollaston prism) = 0.25.

DQE = detective quantum efficiency of detector ≃ 0.33.

Thus

$$\text{Number of photons required} = (1/E)[3(2)^{\frac{1}{2}}/\Delta]^{2}(1/DQE^{2}).$$

This relationship is shown in Fig. 44.

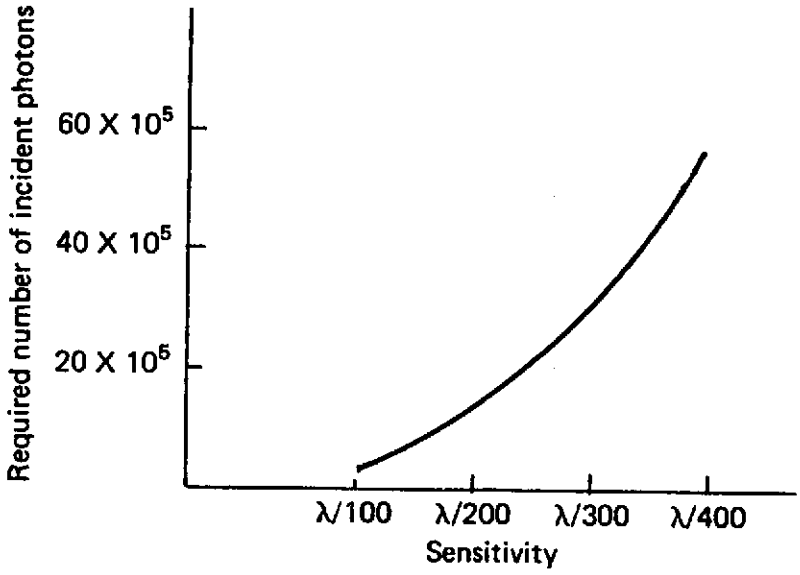

Fig. 44. Relationship between the required number of incident photons versus sensitivity.

Using

$a = 100\ cm^2$

$B = 500\ \text{Å}$

$N = 1060$ photons/cm^2sec Å for A_o zero magnitude star,

we obtain a graph of sampling time versus star magnitude for various sensitivity requirements as shown in Fig. 45.

g. Effect of Shearing on Low-Order Aberrations

In the shearing interferometer we measure the difference in optical path between two points in the pupil as shown in Fig. 46. Below we derive expressions in terms of the shear S and the aberration

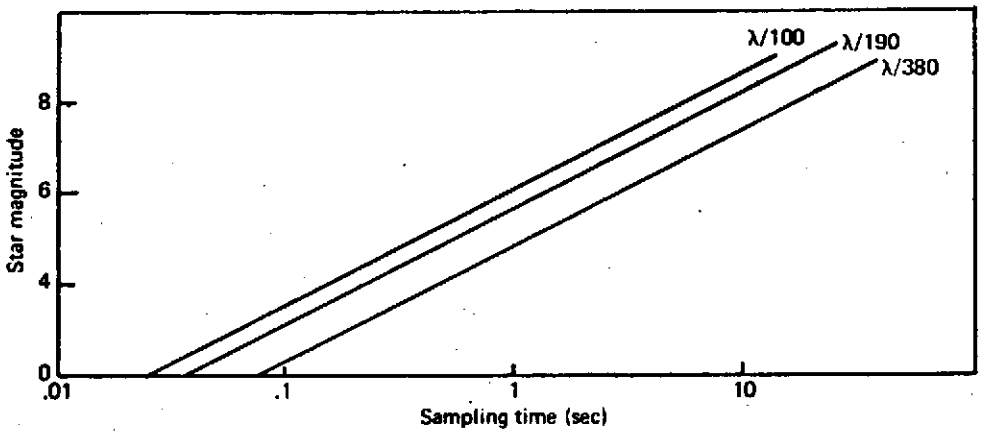

Fig. 45. Sampling times and stellar magnitudes required for three sensitivities.

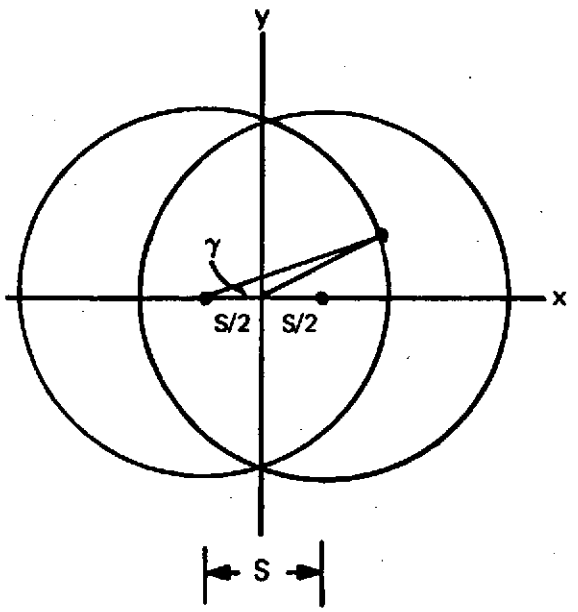

Fig. 46. Shear pupil geometry.

coefficients. From these expressions we will be able to predict the sensitivity of measurement for low-order aberrations as a function of shear S and instrument sensitivity

$$x^2 + y^2 \leq 1 + \frac{S^2}{4} - 2 \cdot \frac{S}{4} \cos\gamma$$

$$\sin\gamma = \frac{y}{1}$$

$$|y_{max}| = + [1 - (S/2)^2]^{\frac{1}{2}}$$

$$|x_{max}| = |1 - (S/2)|.$$

In the nonsheared pupil, if coma is oriented at angle θ, astigmatism at angle ψ, and tilt at angle α, all measured from the y axis, the general wavefront expression is

$$\begin{aligned} W(x,y) = {} & W_{20}(x^2 + y^2) + W_{40}(x^4 + 2x^2y^2 + y^4) \\ & + W_{11}x \sin\alpha + W_{11}y \cos\alpha + W_{31}(x^2 + y^2) \\ & (x \sin\theta + y \cos\theta) \\ & + W_{22}[\tfrac{1}{2}(x^2 + y^2) + \tfrac{1}{2}(y^2 - x^2) \cos 2\psi + xy \sin 2\psi]. \end{aligned}$$

This is a normalized expression where $x^2 + y^2 \leq 1$. We now shear the pupils by an amount S, where S is a number from 0 to 2 (where S = 2 is a shear of a pupil diameter). At some point A, we now have two waves, W(+) and W(-) interfering

$$W(\pm) = W(x \pm \frac{S}{2}, y).$$

By substituting in the previous expression for W we obtain

$$W(\pm) = W_{20}\{(x^2+y^2) \pm Sx + \frac{1}{4}S^2\}$$

$$+ W_{40}\{(x^2 + 2x^2y^2 + y^4) \pm 2x(x^2+y^2)S + \frac{1}{2}(3x^2+y^2)S^2 \pm \frac{1}{2}xS^3 + \frac{1}{16}S^4\}$$

$$+ W_{11}\{x \sin\theta \pm \frac{1}{2}S \sin\alpha + y \cos\alpha\}$$

$$+ W_{31}\{(x^2+y^2)(x \sin\theta + y \cos\theta) \pm \frac{1}{2}[(3x^2+y^2)(\sin\theta) + 2xy \cos\theta]S + \frac{1}{4}[3x \sin\theta + y \cos\theta]S^2 \pm \frac{1}{8}S^3\sin\theta\}$$

$$+ W_{22}\{[\frac{1}{2}(x^2+y^2) + \frac{1}{2}(y^2-x^2)(\cos2\psi) + (xy \sin2\psi)] + \frac{1}{2}[(1-\cos2\psi)x + (\sin2\psi)y]S + \frac{1}{8}[(1-\cos2\psi)]S^2\}.$$

At point A, we measure the difference between W(+) and W(-)

$$W(+) - W(-) = 2W_{20}xS + 4W_{40}x(x^2+y^2)S + W_{40}xS^3 + W_{11}S \sin\alpha + W_{31}[(3x^2+y^2)\sin\theta + 2xy \cos\theta]S + \frac{1}{4}W_{31}\sin\theta S^3 + W_{22}[(1-\cos2\psi)x + \sin2\psi y]S.$$

i. Sensitivity dilution

We can make use of the expression above to determine our ability to measure various amounts of the different aberration types as a function of (1) our ability to measure W(+) - W(-) and (2) the amount of shear S. This information is summarized in Table VII. We see that in general the result of shearing is to reduce the sensitivity in measuring small amounts of aberration. This dilution, of course, is dependent upon the functional form of the aberration and the amount of shear. For the LST a shear of 0.2 → 0.4 (the value of S) would be appropriate since it would give information over most of the pupil. The important thing to recognize here is that shearing dilutes the sensitivity of any readout one chooses and that in order to make up for this dilution one must look for more sensitive forms of readout, as in the case of the polarization type readout, which we are investigating.

Table VII

Shearing polarization interferometer with lateral shear

(a) λ/50 detection capability, static, fringe position reading

	Sensitivity (λ)		
	Shear		
Aberration	0.1	0.3	0.8
Defocus	1/10	1.25	1/48
Tilt	1/5	1/15	1/40
Spherical	1/16	1/37	1/50
Coma	1/14	1/32	1/50
Astigmatism	1/10	1/25	1/48

(b) $\lambda/300$ detection capability, polarization or other phase reading scheme

	Sensitivity (λ)		
	Shear		
Aberration	0.1	0.3	0.8
Defocus	1/60	1/150	1/290
Tilt	1/30	1/90	1/240
Spherical	1/100	1/220	1/300
Coma	1/80	1/195	1/300
Astigmatism	1/60	1/150	1/290

ii. Small Shear Limit.

As we make S small we can take the division

$$\frac{W(+) - W(-)}{S} = W_{11}\sin\alpha + 2W_{20}x + 4W_{40}x(x^2+y^2) + W_{31}[(3x^2+y^2)\sin\theta + 2xy\cos\theta] + W_{22}[(1-\cos 2\psi)x + \sin 2\psi y].$$

This is merely the expression for $\delta W/\delta x$, the slope of the wavefront (x component) at x,y. A corresponding shear in the y direction would then give the y component slope $\delta W/\delta y$.

h. Experimental Evaluation

i. Procedure

The experimental arrangement illustrated in Fig. 38 was set up on the optical bench, a photograph of which appears in Fig. 47. We

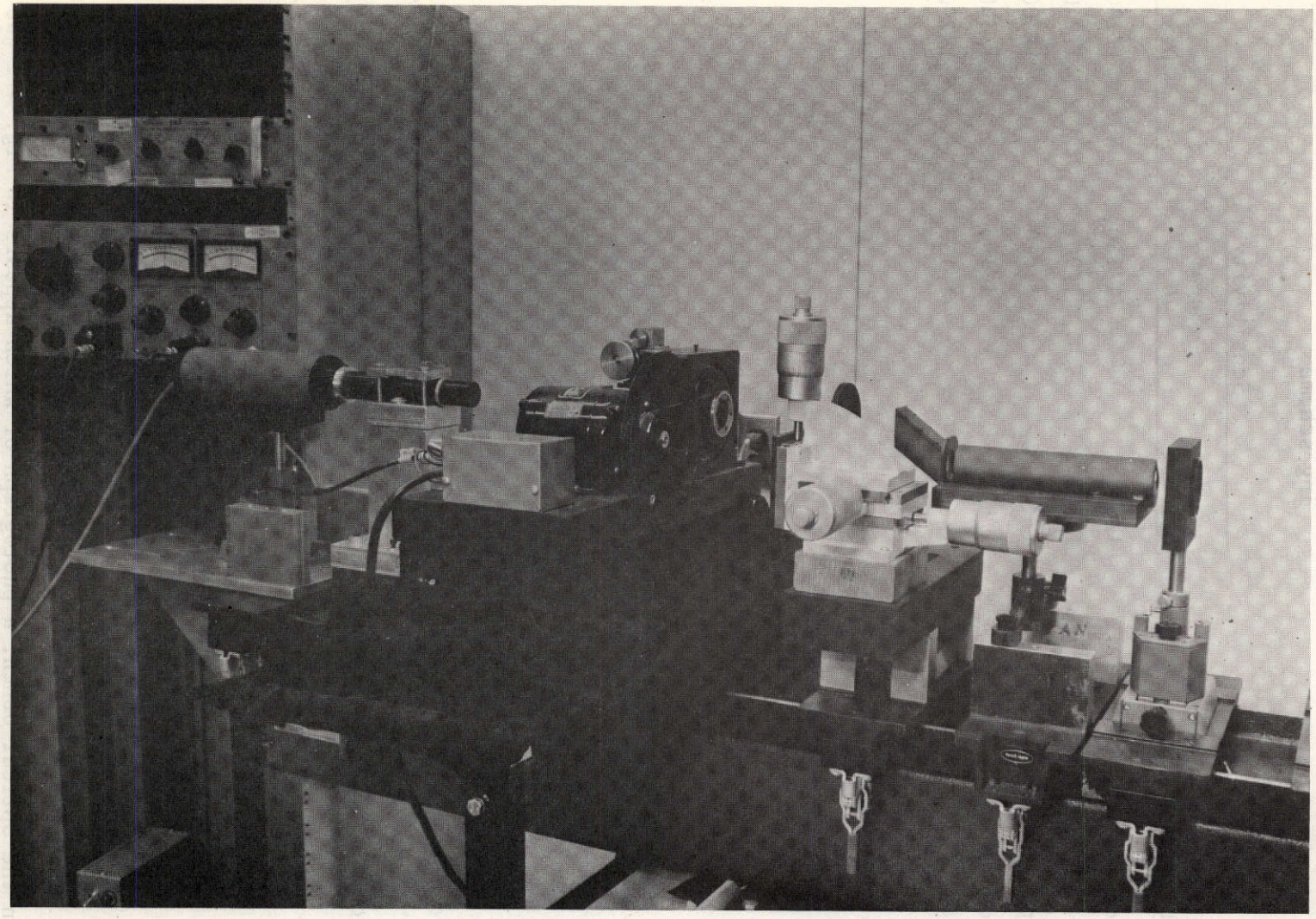

Fig. 47. Shearing polarization test experimental arrangement.

first attempted to use a narrowband white light source approximately 40 nm wide. Unfortunately, we were not able to produce the coherency required to obtain interference. While we have not quantitatively answered this problem we believe that it stems from the double Wollaston shearing scheme, which was chosen for laboratory convenience. We believe that the path differences accumulated by the orthogonally polarized sheared pupils exceeds the coherence length required for interference effects to occur. This problem probably arises from poor Wollaston matching, misalignment, and the fact that this shearing scheme is not self-compensating. However, we do feel that one of the other shearing mechanisms such as described in Fig. 33 could eliminate this problem if properly manufactured. Furthermore, we feel that the polarization read-out scheme is at least as important to evaluate as the shearing mechanism. With these things in mind, we substituted a laser source for the white light source and proceeded as follows.

The Wollaston separation was adjusted to give the sheared pupil situation illustrated in Fig. 48.

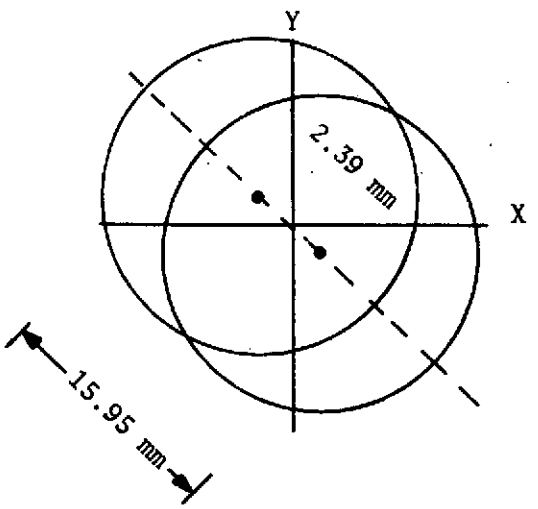

Fig. 48. Sheared pupil situation.

This corresponded to a shear value S = 0.27 at 45°. The pupil was then scanned in the shear direction using a 1.25-mm scanning aperture at four positions out to 7.2 mm. A similar procedure as was described for the Hartmann test was followed. First, a baseline was established by readout of the respective polarization angle measurements at each pupil position. Again the center pupil position was monitored to correct for image drift. Aberrations were then introduced and the same procedure was followed. The aberrations change data were then subtracted from the baseline, and a graph of sheared aberration angle vs pupil position was obtained. These data were then fitted to a low-order polynomial, which was then integrated with the proper scaling to produce optical path difference vs pupil positon data. Two runs were taken, one on defocus and the other on spherical plus defocus as shown in Fig. 49.

ii. Discussion

From the preceding data one can see that the sheared phase angle readout is consistently better than 1° departure from the expected value. Thus our readout scheme under laboratory conditions with a mechanically rotating prism scanner produced readout to better than $\lambda/200$, in the sheared sense. This produced OPD results that agreed with predicted values to the order of $\lambda/100$. Thus for an f/12 system, if coherency problems are eliminated in the shearing scheme, this interferometer should be able to satisfy $\lambda/100$ sensitivity requirements.

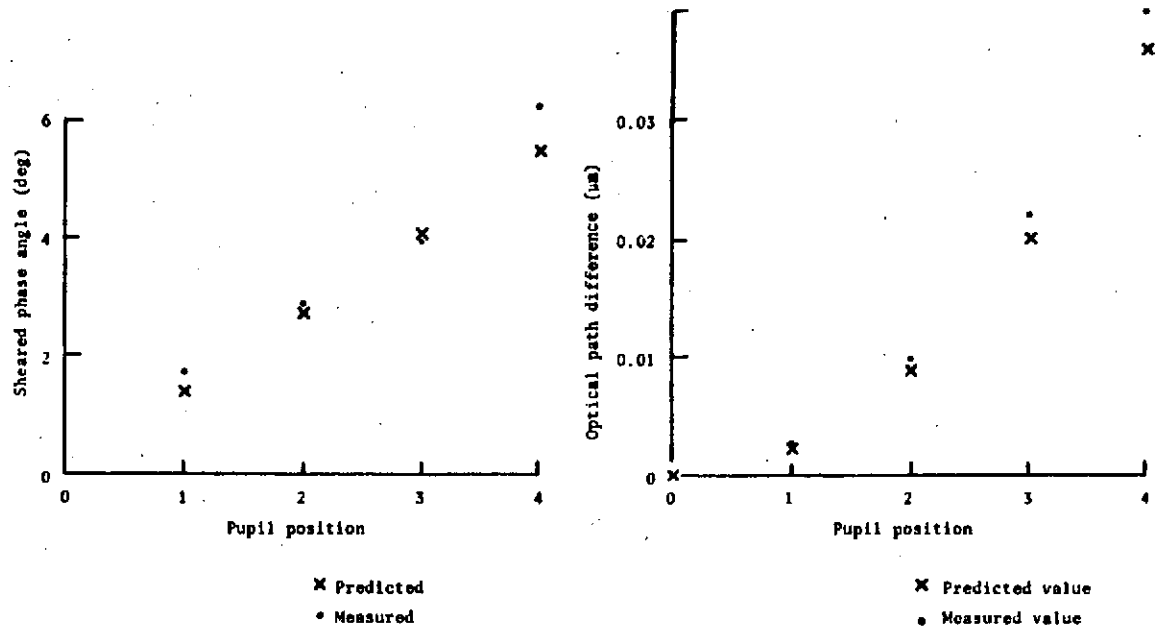

(a) Defocus

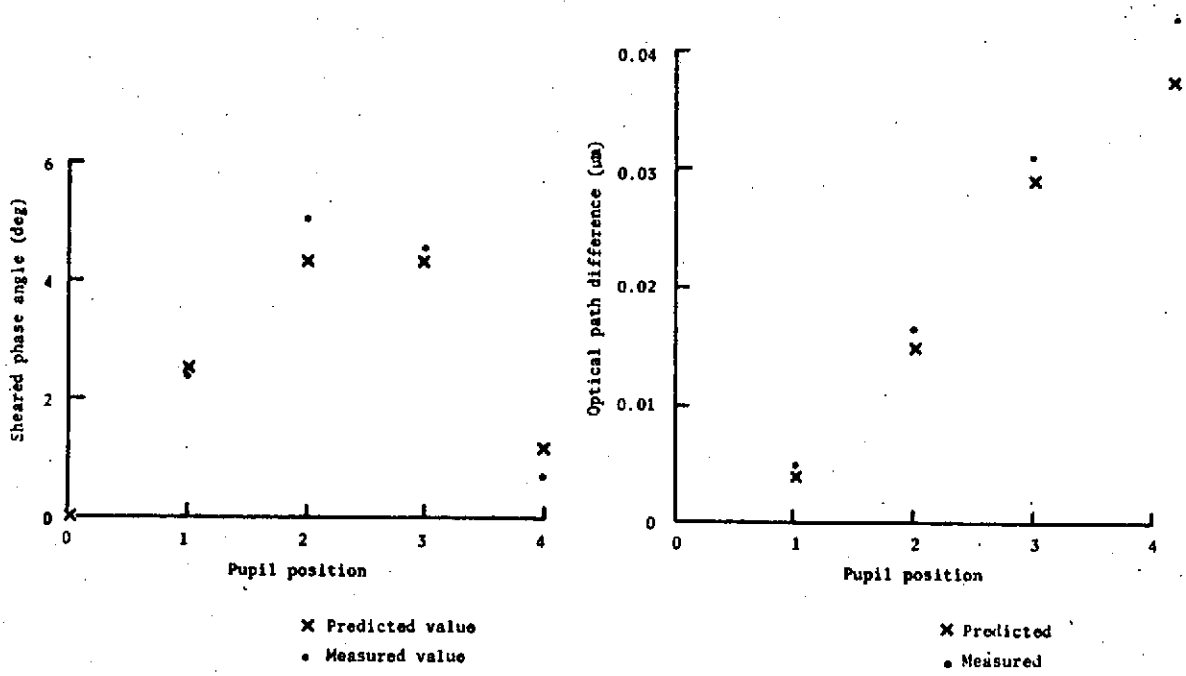

(b) Defocus plus spherical aberration

Fig. 49. Sheared phase angle and optical path difference vs pupil position for defocus and for defocus plus spherical aberration.

3. Zernike Polarization Sensor (ZPS)

a. General Discussion

The ZPS represents a conceptual attempt to marry the Zernike test to a polarization readout. The result can be a sensor with at least the sensitivity of the Zernike test and a readout that provides for a direct phase measurement in terms of the linear polarization state.

The experimental arrangement is indicated in Fig. 50. The wavefront from the system exit pupil first passes through a linear polarizer. At the system focus we place a birefringent crystal polished with its optic axis in the plane of the surface and adjusted to a multiple order thickness of a quarter wave. A small cylindrical well (~1/5 the Airy disk diameter) is eroded to a depth corresponding to a half-wave retardation between the ordinary and extraordinary waves. The area surrounding the square well is partially aluminized so that, with the Airy pattern centered across the well, the energy transmitted through the well is equal to the energy transmitted through the surround. As a result of this arrangement, we generate a reference wave of one circular polarization from the inner part of the central core of the diffraction pattern, and a test wave of the opposite circular polarization from the outer part of the diffraction pattern. The lens following reimages the system pupil at plane C. In this plane, the two oppositely circular polarized waves interfere. According to the equations developed for the Zernike test, which are again applicable here, the test wave contains the wavefront deformation from each point on the pupil, and the reference wave is of essentially constant phase across the pupil, the constant

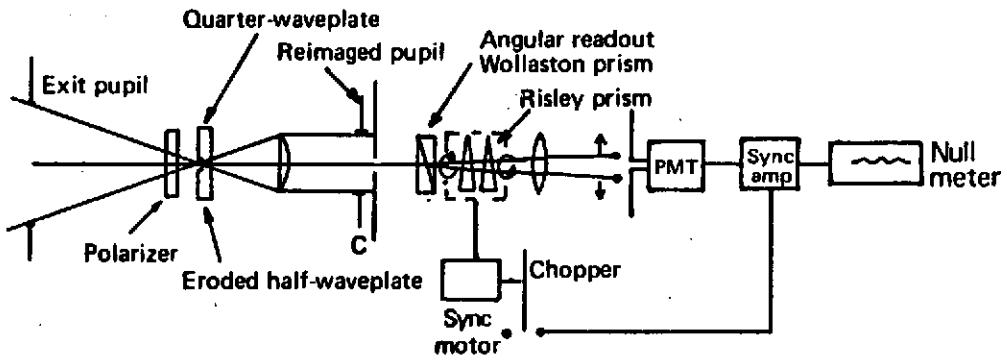

Fig. 50. Zernike polarization sensor laboratory simulation.

dependent on the amount and type of aberration and the size of the eroded well. These two waves combine to produce a linearly polarized state (the polarization direction depending on the phase difference at the point) at each point in the pupil. We measure this polarization using a device of the type discussed in Chapter 4 and illustrated again in Fig. 50. We thus have a test with the simplicity of the Zernike test where we read out phase directly.

b. Design Parameters for ZPS

The optimum design parameters for the ZPS are obtained from the same equations derived for use with the Zernike disk. The effects of the diameter of the half-wave plate will be manifested in the circular polarization variations in the generated reference wave. For small elliptical polarization effects, we want to keep this diameter about 1/5 the Airy core diameter. The transmission attenuation is introduced

only because of its effect on the visibility function since we are not concerned with the operating point using the ZPS.

c. Manufacture

The success of the ZPS depends on the ability to manufacture a small half-wave plate. In order to eliminate tunneling effects we decided to look at materials with a high birefringent index. The two we chose are calcite and rutile.

We prepared several samples of both materials cut with their optical axis lying in the planes of the polished surfaces. We sought a procedure that would yield a smooth controllable surface erosion for these materials. We tried many different acids on calcite and discovered one combination that gave promising results; however, combinations of acids under different conditions for rutile did not have positive results.

Unfortunately, we were not able to manufacture the microhalf-wave plate because of our inability to work out various chemical and imaging problems. The approach with calcite, however, still has possibilities and perhaps with further research the manufacturing details could be worked out.

CHAPTER 5

SUMMARY AND RECOMMENDATIONS

1. Wavefront Error Simulator

A wavefront error simulator was designed and manufactured in order to simulate various stellar magnitudes, wavelength ranges, and aberration conditions. The most critical part of the simulator design was that of the aberration generator. This component was designed, fabricated, and calibrated so that incremental changes of less than $\lambda/100$ could be introduced for low-order aberrations. The low-order aberrations represent the types of wavefront error expected in the operational LST. The wavefront error simulator was used in the experimental evaluation of the Hartmann test, the Zernike test, and the shearing polarization interferometer. Since low-order aberrations are more difficult to measure than high-order aberrations, the test sensitivities quoted below are in general likely to be conservative.

2. Hartmann Test

The most important consideration in the Hartmann test was the method chosen for determining the slope of the sampled bundle of rays from the telescope exit pupil. It was decided that the best approach was to nutate the diffraction pattern formed by the sampled ray bundle about a small collecting aperture. If the diffraction pattern nutation was not perfectly centered on the collecting aperture, an ac error signal indicated a ray bundle slope error. It was found that under laboratory

conditions the highest sensitivities for slope error detection were obtained when the collecting aperture was approximately the same size as the diffraction pattern of the sampled bundle. Slope determination was ultimately limited by the prevailing laboratory conditions. The random error associated with the slope measurement was approximately the same size as the diffraction pattern of the sampled bundle. Slope determination was ultimately limited by the prevailing laboratory conditions. The random error associated with the slope measurement was approximately 0.2 arc sec rms. The wavefront error simulator was used to introduce known aberration changes so that the wavefront error measuring capability of the Hartmann test could be determined. *It was found that low-order aberrations could be measured to accuracies of* $\lambda/50$ *to* $\lambda/100$. This degree of accuracy contrasts with the common misconception that the Hartmann test is a relatively coarse geometrical method.

It is recommended that, as a worthwhile continuation, the Hartmann test be constructed using a star tracker tube, with a deflection coil readout capability such as described in Chapter 3. Specifications for the tube and coil stability can easily be obtained from the results of the parametric and statistical studies. It would be worthwhile to incorporate a reference position monitoring mechanism, with differential detection. In this way slow drift effects and common vibrational effects such as discussed in the experimental evaluation in Chapter 3 could be eliminated.

3. Zernike Test

A general theory of the Zernike test was developed. It included a procedure for specifying Zernike disk parameters such as phase, transmission, and disk size so that the disk parameter choice was optimal for the particular experimental situation. A technique for manufacturing optimized Zernike disks was developed. One of these disks was incorporated into a laboratory Zernike figure sensor that was then used to measure the aberration changes introduced by the wavefront error simulator. *It was found that the aberration changes could be measured to better than $\lambda/100$ for all low-order aberrations.* The major source of experimental error was due to source intensity fluctuations and image drift.

4. Zernike Polarization Test

One of the major disadvantages of the Zernike test was that the aberration was not measured directly but rather in terms of an intensity change from a nominal zero aberration intensity level. It may be possible to eliminate this problem by using the Zernike disk principally in the form of a polarization interferometer, where the aberration would manifest itself as a linear polarization state change in the reimaged pupil. One approach to implementing the principal involved the use of a micro-half-wave plate manufactured from a birefringent material. We attempted to manufacture the micro-half-wave plate in calcite by an erosion process. Out attempt was not successful. However, we feel that a disk can be made with further research effort directed toward establishing a photoresist and etching procedure for calcite.

Another possible way of implementing the Zernike polarization test is illustrated in Fig. 51. Conceptually, as the light from the system exit pupil converges toward focus, it first passes through a polarizer and then enters the prism A through a concentric surface without introducing spherical aberration. At the polarizing beamsplitting surface I, the beam is split into two orthogonal linear polarizations. One of these beams comes to a focus in the vicinity of pinhole B and passes through. The pinhole is small enough to transmit only the central part of the Airy disk. The light getting through the pinhole forms a linearly polarized, near perfect reference wave. The light focused at B' is unaltered and thus contains the aberration information in an orthogonal-linear polarized state. The polarizer is rotated to equalize the energy in the two beams. The two beams continue to diverge, and the test beam passes completely through the second polarizing beamsplitter while the reference beam is totally reflected. The orthogonal-linear beams then pass through a quarter-wave plate oriented at 45° to the polarization directions and emerge in orthogonal circularly polarized states. Lens C then collimates these waves and reimages the exit pupil at D. At any point in the reimaged pupil at D, the oppositely circularly polarized states combine to yield a linear polarized state where the polarization direction is directly proportional to the phase error in the test wave. There are many methods that can be used to read out the polarization direction. Two of these methods indicate that the phase could be measured directly to better than $\lambda/200$.

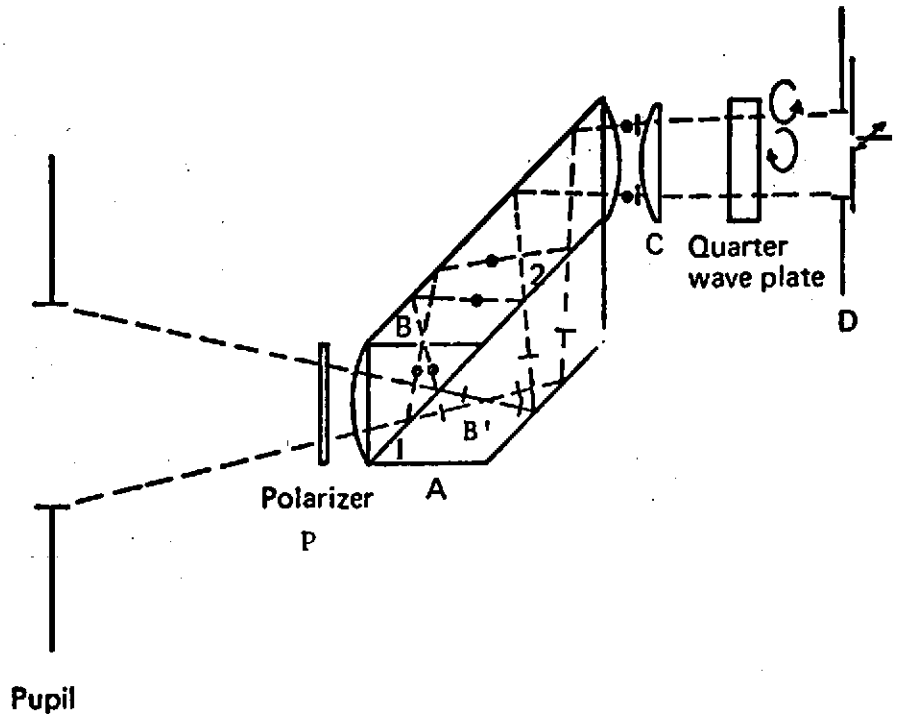

Fig. 51. Arrangement for Zernike polarization test.

The critical item for manufacture is the monolithic polarizing prism A. It would be required that the total optical path traveled by the reference wave be equal, to within the coherence length of the light used, to that traveled by the test wave.

5. Shearing Polarization Interferometer

We examined the general capability of the lateral shearing interferometer and reached the conclusion that a conventional lateral shearing device would not have adequate sensitivity because of the dilution of sensitivity inherent in a lateral shear. However, by incorporating a polarization-type readout into the interferometer we could increase the

sensitivity of the instrument significantly. Thus, in the laboratory the primary objective in the construction of a lateral shearing interferometer was the experimental analysis of the polarization-type readout using a star source. We thus designed and manufactured a white light lateral shearing polarization interferometer in order to evaluate the polarization readout scheme. We did S/N ratio studies and subsequent predictions on sensitivities and required stellar magnitudes. An error analysis on the system alignment and component fabrication also yielded results. The interferometer was constructed and evaluated using a laser star source because the shearing scheme did not maintain the coherency required for broadband use. With the laser source it was found that the sensitivity to low-order aberration measurement was $\lambda/100$.

6. Concluding Comments

A surprising and important result obtained in the research was the discovery that the Hartmann test is remarkably sensitive. The Hartmann test was originally considered to be suitable only for measuring aberrations in the range of many waves down to about a tenth of a wave. The results of the research indicate that the Hartmann test has sensitivities approaching $\lambda/100$, and at this point the laboratory environment limited the sensitivity attainable. Thus, it may be possible to use the Hartmann test to measure the very large aberrations as well as small aberrations with sensitivities approaching that of the Zernike test.

APPENDIX

This Appendix contains a bibliography on optical testing. The work was compiled at the Instituto Nacional de Astrofísica, Optica, y Electrónica, located in Puebla, Puebla, Mexico. It represents a two-year effort by graduate students under the direction of Dr. D. Malacara-Hernandez and is included here with his kind permission.

1. NEWTON AND FIZEAU INTERFEROMETERS

1.1 Newton Fringes and Test Plates

Hodgkinson, I. J., "A Method for Mapping and Determining the Surface Defects Function of a Pair of Coated Optical Flats," *Appl. Opt.*, 8, 1373 (1969).

Malacara, D., and A. Cornejo, "Testing of Aspherical Surfaces with Newton Fringes," *Appl. Opt.*, 9, 837 (1970).

Speyer, E., "A Calculation of Newton Ring Tolerances for Prism Faces," *J. Opt. Soc. Am.*, 34, 529 (1944).

1.2 Fizeau Interferometer

Ashton, A., and A. C. Marchant, "Note on the Testing of Large Glass Panels," *Optica Acta*, 14, 203 (1967).

Biddles, B. J., "A Non-Coating Interferometer for Testing Steepled Curve Surfaces," *Optica Acta*, 16, 137 (1968).

Bunnagel, R., A. Oehring and K. Steiner, "Fizeau Interferometer for Measuring the Flatness of Optical Surfaces," *Appl. Opt.*, 7, 331 (1968).

Collyer, P. W., "A Method of Sharpening Fizeau Fringes," *J. Opt. Soc. Am.*, 41, 285 (1951); (Paper #1 of the OSA, Winter 1951).

Dukhopel, I. I., and I. Y. Urnis, "Selection of the Best Interferometer for Quality Control of Spherical Surfaces," *Sov. J. of Opt. Tech.*, 36, 545 (1969).

_____, "Interference Methods and Instruments for Inspecting Optical Flats," *Sov. J. of Opt. Tech.*, 38, 570 (1971).

Heintze, L. R., H. O. Polster and J. Vrabel, "A Multiple Beam Interferometer for Use with Spherical Wavefronts," *Appl. Opt.*, 6, 1924 (1967).

Kontiyevskiy, Yu P., O. A. Klochkova and A. Ya. Perezhogin, "Improved Two-Beam Interferometer," *Sov. J. of Opt. Tech.*, 35, 559 (1968).

Landewehr, R., and Z. Menden, "Zur Mussung der Ebenheit Von Reflektieranden Flachen Mittels Interferenzen Glaicher Dicke (The Measurement of Planess of Reflecting Surfaces using Fringes of Equal Thickness)," *Optik*, 5, 354 (1949).

Leppelmeier, G. W., "A Technique to Measure the Wedge Angle of Optical Flats," *Appl. Opt.*, 9, 509 (1970).

Murty, M.V.R.K., "A Note on the Testing of Large Aperture Parallel Plates of Glass," *Appl. Opt.*, 2, 1377 (1963).

_____, "Addendum to: A Note on the Testing of Large Aperture Parallel Plates of Glass," *Appl. Opt.*, 3, 784 (1964).

_____, "Interferometry Applied to Testing of Optics," *Bull. Opt. Soc. India*, 1, 29 (1967).

_____, and R. P. Shukla, "Some Considerations of Fizeau Interferometer," *Bull. Opt. Soc. India*, 4, 13 (1970).

Post, D., "Characteristics of the Series Interferometer," *J. Opt. Soc. Am.*, 44, 243 (1954).

Primak, W., "The Determination of the Absolute Contours of Optical Flats," *Appl. Opt.*, 7, 1917 (1968).

Raman, C. V., and V. S. Rajagolapan, "Haidinger Interference in Curved Plates," *J. Opt. Soc. Am.*, 29, 413 (1939).

_____, et al., "Haidinger's Fringes in Non-Uniform Plates," *Phil. Mag.*, 29, 508 (1939).

Roesler, F. L., "Mapping of High Quality Optical Flats without Reflection Coating," *J. Opt. Soc. Am.*, 52, 471 and 600 (1962).

_____, and W. Traub, "Precision Mapping of Pairs of Uncoated Optical Flats," *Appl. Opt.*, 5, 463 (1966).

Saunders, J. B., "Parallel Testing Interferometer," *J. Res. Nat. Bur. Standards*, 61, 491 (1958).

_____, "In-Line Interferometer," *J. Opt. Soc. Am.*, 44, 241 (1959).

Scherf, G.,"El Planimetro 12, Aparato Optico de Interferencia para la Comprobacion de Superficies Plana," *Revista Jena*, 2, 107 (1966).

Schonrock, O., "Testing Planes of Surface by Haidinger's Rings," *Z. Instrumentenk*, 59, 31 (1939).

Schulz, G., J. Schmider, C. Hiller, and B. Kickur, "Establishing an Optical Flatness Standard," *Appl. Opt.*, 10, 929 (1971).

Sen, D., and D. N. Puntambgkar, "An Inverting Fizeau Interferometer," *Optica Acta*, 12, 137 (1965).

Speyer, G., "The Interference Spherometer," *Rev. Sci. Instr.*, 14, 336 (1943).

Taylor, W.G.A., "Fizeau Interferometer," *Nature*, 34, 399 ( ).

Timms, C., "The Measurement of Finally Finished Surfaces by Optical Interference," *J. Sci. Instr.*, 22, 245 (1945).

Van Heel, A. S., "Interferometric Testing of Concave Mirrors with Laser Light and the Correction of S.A. of a Sphere by a Plane Parallel Plate," *Optica Acta*, 13, 383 (1966).

Yoder, P. R. Jr., and W. W. Hollis, "Design of a Compact Wide Aperture Fizeau Interferometer," *J. Opt. Soc. Am.*, 47, 858 (1957).

2. TWYMAN-GREEN, MACH ZEHNDER AND JAMIN INTERFEROMETERS

2.1 Twyman-Green Interferometer

Bottema, M., and F. Zernike, "The Three-Beam Interferometer," *J. Opt. Soc. Am.*, 41, 870 (1951).

Bruning, J. H., and D. R. Herriot, "A Versatile Laser Interferometer," *Appl. Opt.*, 9, 2180 (1970).

Buin, A. P., M. P. Semeneva and L. A. Kiryukhina, "Inspection of the Surface Quality of Large Scale Optical Components of an Unequal-Arm Interferometer," *Sov. J. Opt. Tech.*, 36, 720 (1969).

DeVany, A. S., "A Note on Testing Homogeneity of Glass," *Appl. Opt.*, 3, 645 (1964).

_____, "On Using a Williams Interferometer for Making a Divider Plate," *Appl. Opt.*, 4, 365 (1965).

Grigull, V., and H. Rottenkolber, "Two Beam Interferometer Using a Laser," *J. Opt. Soc. Am.*, 57, 149 (1967).

Hansen, G., "Die Sichtbarkeit der Interferenzen Beim Twyman-Interferometer," *Optik*, 12, 5 (1955).

Harper, D. C., and R. D. Pickering, "The Use of Power Compensation in the Testing of Optical Components in the Twyman-Green Interferometer," *J. Opt. Soc. Am.*, 43, 813 (1953).

Houston, J. B. Jr., C. J. Buccini and P. K. O'Neill, "A Laser Unequal Path Interferometer for the Optical Shop," *Appl. Opt.*, 6, 1237 (1967).

Lenouvel, L., and F. Lenouvel, "Etude des Faisceaux Convergents," *Rev. Opt.*, 17, 350 (1938).

Marechal A., and P. Dejonc, "Quelques Aspects des Franges de Twyman (Some Aspects of Twyman Fringes)," *Rev. Opt.*, 29, 430 (1950).

Michelson, A. A., "Correction of Optical Surfaces," *Astrophys. J.*, 47, 283 (1917).

Murty, M.V.R.K., "Simulation of Primary Aberrations of a Lens using a Generalized Michelson Interferometer," *J. Opt. Soc. Am.*, 50, 1089 (1960).

Ostrorskaya, M. A., and N. F. Filimonova, "Use of Gas Laser for Interferometric Quality Control in Telescope Manufacture," *Sov. J. Opt. Tech.*, 36, 563 (1969).

Puryayev, D. T., "Quality Control of Aspherical Surfaces by an Interferometric Compensating Method," *Sov. J. Opt. Tech.*, 35, 624 (1968).

Saunders, J. B., and F. L. Gross, "Interferometer for Large Surfaces," *J. Res. Nat. Bur. Stands.*, 62, 137 (1959).

_____, "Precision Method for Evaluating Primary Aberrations of Lenses with a Twyman Interferometer," *J. Res. Nat. Bur. Stands.*, 69c, 251 (1965).

Slevgot, H., "Zur Geometrischen Optik der Zweistrahl-Interferometer (The Geometrical Optics of Two-Beam Interferometers)," *Optik*, 11, 366 (1954).

Twyman F., "La Production des Surfaces Aspheriques (The Production of Aspheric Surfaces)," *Rev. Opt.*, 26, 461 (1947).

_____, "Interferometers for the Experimental Study of Optical Systems from the Point of View of the Wave Theory," *Phil. Mag.*, 35, 49 (1918).

_____, "Correction of Optical Surfaces," *Astrophys. J.*, 48, 256 (1918).

_____, "The Interferometer in Lens and Prism Manufacture," *Nature*, 151, 43 (1943).

Tynes, A. R., and D. L. Bisbee, "Precise Interferometry of Glass Plates," *J. Quant. Elec.*, 3 QE, 459 (1967).

Van Heel, A.C.S., and C.A.J. Simmons, "Lens and Surface Testing with Compact Interferometers," *Appl. Opt.*, 6, 803 (1967).

Van Rooyen, E., "Design for a Variable Shear Prism Interferometer," *Appl. Opt.*, 7, 2423 (1968).

Young, T. R., "Test of Aerial Camera Lenses of Large Aperture with a Twyman Interferometer," *J. Opt. Soc. Am.*, 42, 874 (1952).

2.2 Jamin and Mach-Zehnder Interferometer

Lummer, O., *Ann. Physik*, 23, 513 (1884).

Murty, M.V.R.K., "Some Modifications of the Jamin Interferometer Useful in Optical Testing," *Appl. Opt.*, 3, 535 (1964).

Saunders, J. B., "Parallel Testing Interferometer," *J. Res. Nat. Bur. Stands.*, 61, 491 (1958).

Waetzman, E., "Jamin Interferometer," *Ann Physik*, 39, 1042 (1912).

2.3 Polarized Light Interferometer

Bruning, J. H., and D. R. Herriot, "A Versatile Laser Interferometer," *Appl. Opt.*, 9, 2180 (1970).

3. MULTIPLE REFLECTION INTERFEROMETERS

3.1 Single Source Interferometers

Duffieux, D. M., "Harmonic Analysis of Interference Fringes Produced by Multiple Reflections," *Rev. Opt.*, 18, 1 and 201 ( ).

Houston, J. B. Jr., "How to Make and Use a Scatterplate Interferometer," *Optical Spectra*, 4, 32 (1970).

Langenbeck, P., "VI. Multipass Interferometry," *Appl. Opt.*, 8, 543 (1969).

Meier, B., "A Workshop Interference Microscope on the Multibeam Method," *Review Jena*, 5, 148 (1958).

Pastor, J., and P. H. Lee, "Transmission Fringes in Reflection Multiple Beam Interferometry," *J. Opt. Soc. Am.*, 58, 149 (1968).

Sakurai, T., and K. Shishido, "Test of an Optical Flat by the Fabry-Perot Etalon," *Sci. Rep. Res. Inst.* (Tohuko University), 1, 83 ( ).

Schulz, L. J., "Accurate Thickness Measurements with a Fabry-Perot Interferometer," *J. Opt. Soc. Am.*, 40, 177 (1950).

Schoemaker, A. H., and M.V.R.K. Murty, "Some Further Aspects of Scatter Fringe Interferometry," *Appl. Opt.*, 5, 603 (1966).

Tolansky, S., "New Contributions to Interferometry," *Phil. Mag.*, 36, 225 (1945).

_____, and M. Omar, "Thin Film Interferometer Technique for High Magnification Topographic Studies," *Nature* (London), 170, 181 ( ).

_____, "Multiple Beam Interferometry," *Endeavour*, 9, 196 ( ).

3.2 Multiple Source Interferometers

Herriot, D. R., "Multiple Wavelength, Multiple Beam Interferometric Observation of Flat Surfaces," *J. Opt. Soc. Am.*, 51, 1142 (1961).

_____, "Long Path Multiple Wavelength, Multiple Beam Interference Fringes," *J. Opt. Soc. Am.*, 56, 719 (1966).

Murty, M.V.R.K., "Multiple-Pinhole, Multiple Beam Interferometric Observation of Flat Surfaces," *Appl. Opt.*, 1, 364 (1962).

Pilston, R. G., and G. N. Steinberg, "Multiple Wavelength Interferometry with Tunable Lasers," *Appl. Opt.*, 8, 553 (1969).

4. COMMON-PATH INTERFEROMETERS

4.1 Burch Interferometer

Burch, J. M., "Scatter Fringes of Equal Thickness," *Nature*, 171, 889 (1953).

Hodgkinson, I. J., "A Simpler Scatter Method for Optical Surface Roughness and Slope Measurements Roughness of Polished Fused Silica," *J. of Physics E, Scientific Instruments*, 3, 342 (1970).

Houston, J. B. Jr., "How to Make and Use a Scatterplate Interferometer," *Optical Spectra*, 4, 32 (1970).

Koehler, W. F., and W. C. White, "Multiple Beam Fringes of Equal Chromatic Order, Part IV Method of Measuring Roughness," *J. Opt. Soc. Am.*, 45, 1011 (1955).

4.2 Fresnel Zone Plate Interferometer

Murty, M.V.R.K., "Common Path Interferometer using Fresnel Zone Plates," *J. Opt. Soc. Am.*, 53, 568 (1963).

4.3 Birefringent Interferometer

Dyson, J., "A Common-Path Interferometer for Testing Purposes," *J. Opt. Soc. Am.*, 47, 386 (1957).

_____, "Very Stable Common-Path Interferometer and Applications," *J. Opt. Soc. Am.*, 53, 690 (1963).

5. SHEARING INTERFEROMETERS

5.1 Radial Shearing Interferometers

Bryngdahl, O., "Reversed-Radial Shearing Interferometry," *J. Opt. Soc. Am.*, 60, 915 (1970).

_____, "Shearing Interferometry with Constant Radial Displacement," *J. Opt. Soc. Am.*, 61, 169 (1971).

Donath, E., and W. Carlough, "Radial Shearing Interferometer," *J. Opt. Soc. Am.*, 53, 395 (1963).

Hariharan, P., and D. Sen, "Interferometric Measurement of the Aberrations of a Microscope Objective," *Optica Acta*, 9, 159 (1962).

Murty, M.V.R.K., "A Compact Radial Shearing Interferometer Based on the Law of Refraction," *Appl. Opt.*, 3, 853 (1964).

Som, S. C., "Theory of Compact Radial Shearing Laser Interferometry," *Optica Acta*, 17, 81 (1970).

5.2 Rotary and Inverting Shearing Interferometers

Armitage, J. D., and A. Lohman, "Rotary Shearing Interferometry," *Optica Acta*, 12, 185 (1965).

Bryngdahl, O., "Longitudinally Reversed Shearing Interferometry," *J. Opt. Soc. Am.*, 59, 142 (1969).

Gates, J. W., "Reverse Shearing Interferometry," *Nature*, 176, 359 (1955).

Murty, M.V.R.K., "Interference Between Rotated or Reversed with Respect to each other and its Relation to Spatial Coherence," *J. Opt. Soc. Am.*, 54, 1187 (1964).

_____, and E. C. Hagerott, "Rotational Shearing Interferometry," *Appl. Opt.*, 5, 615 (1966).

Saunders, J. B., "Measurement of Wavefront without a Reference Standard. Part II: The Wavefront Reversing Interferometer," *J. Res. Nat. Bur. Stands.*, 66 B, 29 (1962).

5.3 Lateral Shearing Interferometers

Ashton, A., and A. C. Marchant, "A Scanning Interferometer for Wavefront Aberration Measurement," *Appl. Opt.*, 8, 1853 (1969).

Bates, W. J., "A Wavefront Shearing Interferometer," *Proc. Phys. Soc.* London, 59 B, 940 (1947).

_____, "The Evaluation of Interferograms by Displacement and Stereoscopic Methods," *Brit. J. Appl. Phys.*, 5, 133 (1954).

Brown, D., "A Shearing Interferometer with Fixed Shear and its Application to Some Problems in the Testing of Astro-Optics," *Phys. Soc. Proc. B*, 67, 232 (1954).

_____, "The Application of Shearing Interferometry to Routine Optical Testing," *J. Sci. Instr.*, 32, 137 ( ).

De Vany, A. S., "Some Aspects of Interferometric Testing and Optical Figuring," *Appl. Opt.*, 4, 831 (1965).

_____, "Quasi-Ronchigrams as Mirror Transitive Images of Shearing Interferograms," *Appl. Opt.*, 9, 1477 and 1944 (1970).

_____, "Supplement to: Some Aspects of Interferometric Testing and Optical Figuring," *Appl. Opt.*, 9, 1219 (1970).

Drew, R. L., "A Simplified Shearing Interferometer," *Phys. Soc. Proc.*, 64, 1005 (1951).

Dutton, D., A. Cornejo and M. Latta, "A Semiautomatic Method for Interpreting Shearing Interferograms," *Appl. Opt.*, 7, 125 (1968).

Dyson, J., "A Common-Path Interferometer for Testing Purposes," *J. Opt. Soc. Am.*, 47, 386 (1957).

_____, "Very Stable Common-Path Interferometer and Applications," *J. Opt. Soc. Am.*, 53, 690 (1963).

Hariharan, P., and D. Sen, "Triangular Path Interferometer," *J. Opt. Soc. Am.*, 49, 1105 (1959).

Komissaruk, V. A., "Investigation of Wavefront Aberration of Optical Systems Using Three Beam Interference," *Opt. Spectrosc.*, 16, 571 (1964).

_____, "The Displacement Interferogram in the Case of a Wavefront Having Rotational Symmetry," *Sov. J. Opt. Tech.*, 36, 8 (1969).

Lohman, A., and O. Bryngdahl, "A Lateral Wavefront Shearing Interferometer with Variable Shear," *Appl. Opt.*, 6, 1934 (1967).

Malacara, D., and M. Mendez, "Lateral Shearing Interferometry of a Wavefront," *Optica Acta*, 15, 59 (1968).

Murty, M.V.R.K., and D. Malacara, "Some Applications of the Gas Laser as a Source of Light for the Testing of Optical Systems," *Jap. J. Appl. Phys.*, 4, Supplement I, 106 (1965). (Proceedings of the Conference on the Photographic and Spectroscopy Optics, Kyoto and Tokyo, 1964.)

_____, "Fabrication of Fixed Shear Cube Type Shearing Interferometer," *Bull. Opt. Soc. India*, 3, 55 (1969).

_____, "A Compact Lateral Shearing Interferometer Based on the Michelson Interferometer," *Appl. Opt.*, 9, 1146 (1970).

_____, "A Simple Method of Introducing Tilt in the Ronchi and Cube Type of Shearing Interferometers," *Bull. Opt. Soc. India*, 5, 1 (1971).

Rooyen, E., and H. G. Nouten, "Design of a Wavefront Shearing Interferometer Useful for Testing Large Aperture Optical Systems," *Appl. Opt.*, 8, 91 (1969).

Salzman, H., "A Simple Interferometer Based on the Ronchi Test," *Appl. Opt.*, 9, 1943 (1970).

Saunders, J. B., "Measurement of Wavefront without a Reference Standard. Part I: The Wavefront Shearing Interferometer," *J. Res. Nat. Bur. Stands.*, 65 B, 239 (1961).

_____, "Wavefront Shearing Prism Interferometer," *J. Res. Nat. Bur. Stands.*, 68 C, 155 (1964).

_____, "Interferometer Test of the 26-Inch Refractor at Leander McCormick Observatory," *Astron. J.*, 69, 449 (1964).

_____, "Some Applications of the Wavefront Shearing Interferometer," *Jap. J. Appl. Phys.*, 4, Supplement I, 99 (1965). (Proceedings of the Conference on Photographic and Spectroscopic Optics, Tokyo and Kyoto, 1964.)

_____, "A Simple Inexpensive Wavefront Shearing Interferometer," *Appl. Opt.*, 6, 1581 (1967).

_____, and R. J. Bruening, "A New Interferometric Test and its Application to the 84-Inch Reflecting Telescope at Kitt Peak National Observatory," *Astron. J.*, 73, 415 (1968).

_____, "A Simple Interferometric Method for Workshop Testing of Optics," *Appl. Opt.*, 9, 1623 (1970).

Schroeder, J. H., and B. P. Ramsan, "Optical Properties of Grating Interferometer," *J. Opt. Soc. Am.*, 30, 355 (1940).

Sen, D., and P. N. Puntambekar, "Shearing Interferometer for Testing Corner Cubes and Right Angle Prisms," *Appl. Opt.*, 6, 1009 (1967).

Wyant, J. C., "Interferometer for Measuring Power Distribution of Ophthalmic Lenses," Technical Note, OLTN 70-51, January, 1971.

5.4 Koester's Prism

Saunders, J. B., "Inverting Interferometer," *J. Opt. Soc. Am.*, 45, 133 (1955).

_____, "Construction of a Koester Double Image Prism," *J. Res. Nat. Bur. Stands.*, 58, 21 (1957).

_____, "Large Aperture Interferometers with Samll Beam Dividers," *J. Res. Nat. Bur. Stands.*, 67 c, 201 (1963).

_____, "Wavefront Shearing Prism Interferometer," *J. Res. Nat. Bur. Stands.*, 68 c, 155 (1964).

5.5 Murty's Interferometer

DeVany, A. S., "An Instrument for Measuring Strain and Homogeneity in Glass," *Appl. Opt.*, 4, 513 (1965).

_____, "Supplement to: An Instrument for Measuring Strain and Homogeneity in Glass," *Appl. Opt.*, 4,756 (1965).

Murty, M.V.R.K., "The Use of a Single Plane Parallel Plate as a Lateral Shearing Interferometer with a Visible Gas Laser Source," *Appl. Opt.*, 3, 531 (1964).

_____, "Some Modifications of the Jamin Interferometer Useful in Optical Testing," *Appl. Opt.*, 3, 535 (1964).

5.6 Polarized Light Interferometers

Francon, M., "Interferometre pour L'Etude en Lumiere Blanche des Variations Quelconques de Chamin Optique," (Interferometer for the Study in White Light of Variations of Optical Flat), *Acad. Sci. Paris*, 234, 311 (1932).

_____, "Application des Interferences par Double Refraction A L'Etude des Aberrations," *Rev. Opt.*, 32, 601 (1953).

Takasaki, H., "Photoelectric Measurement of Polarized Light Means of an ADP Polarization Modulator IV. Lens Interferometer," *J. Opt. Soc. Am.*, 51, 1146 (1961).

6. KNIFE EDGE AND WIRE TESTS

6.1 Testing of Spherical Mirrors and Systems without Spherical Aberration

Coleman, H. S., and S. W. Harding, "The Loss in Resolving Power Caused by Primary Astigmatism, Spherical Aberration in Telescope Systems," *J. Opt. Soc. Am.*, 38, 217 (1948).

Everhart, E., "Null Test for Wright Telescope Mirrors," *Appl. Opt.*, 5, 717 (1966).

Foucault, L. M., "Description des Procedes employes pour reconnaitre la configuration des surfaces optiques," *Ann. D'Observat. Paris*, 5, 197 (1859); *Comp. Ren. Acad. Sci. Paris*, 47, (1858).

Gascoine, S.C.B., "The Theory of the Foucault Test," *Monthl. Not. Roy. Astron. Soc.*, 104 326 (1944).

Gaviola, E., "Foucault Knife Edge Test on Mirrors," *J. Opt. Soc. Am.*, 26, 163 (1936).

, J., "Improvement of Foucault Knife Edge Test," *Astrophys. J.*, 27, 254 (1908).

Hyde, H. (R.E.C.), "An Improved Foucault Testing Device," *Sky and Telescope*, 33, 45 (1967).

Haven, Jr., A. C., "A Simple Recording Foucault Test," *Sky and Telescope*, 38, 51 (1969).

Kingslake, R., "Knife Edge Test for Spherical Mirrors," *Phys. Soc. Proc.*, 49, 376 (1937).

Kutter, A. (A.E.C.), "Testing Long Focus Convex Secondary Mirrors," *Sky and Telescope*, 18, 348 (1958).

Linfoot, E. H., "A Contribution to the Theory of the Foucault Test," *Proc. Roy. Soc. A.*, 186, 72 (1945).

_____, "On the Interpretation of the Foucault Test," *Proc. Roy. Soc. A.*, 193, 248 (1946).

_____, "Astigmatism under the Foucault Test," *Monthl. Not. Roy. Astron. Soc.*, 105, 193 ( ).

Lower, , Amateur Making Telescope, (Advanced Book, pp. 412, Ed. Scientific American), 1953.

Philbert, M., "Procede Analogique Associe a la Methode de Foucault pour la Determination," *Optica Acta*, 14, 169 (1967).

Porter, W. R., "Photography as an Aid in Testing Mirrors' Shadows," *Astrophys. J.*, 47, 324 (1917).

Raiskii, S. M., "On a Way of Realising the Shadow Mehtod," *J. Exper. Therory Phys.*, 20, 378 (1950).

Rank, D. H., P. R. Joder, Jr. and J. Vrabel, "Sensitivity of a Rapid Test for High Speed Parabolic Mirrors," *J. Opt. Soc. Am.*, 39, 36 (1949).

Sudhansukumar, B., "Some Phenomena Observed in Foucault Test," *Astrophys. J.*, 48, 50 (1918).

Yoder, Jr., P. R., "A Quantitative Optical Test for Telescope Mirrors and Lenses," *J. Opt. Soc. Am.*, 24, 250 (1934).

_____, F. B. Patrick and A. E. Gee, "Application of the Rayleigh Criterion to the Null Test of Dall-Kirkham Primary Mirrors," *J. Opt. Soc. Am.*, 45, 881 (1955).

6.2 Phase Contrast Test

Burch, C. R., *Month. Not. Roy. Astron. Soc.*, 94, 384 (1934).

Coleman, H. S., and D. G. Clark, "The Production and Calibration of Foucault Test Objects of Various Contrasts," *J. Opt. Soc. Am.*, 37, 272 (1947).

_____, M. F. Coleman and S. W. Harding, "The Influence of Magnifying Resolving Power of Telescopic Systems for Foucault Test Objects of Different Inherent Contrast," *J. Opt. Soc. Am.*, 39, 771 (1949).

Linfoot, E. H., "On the Zernike Phase Contrast Test," *Roy Astron. Soc.*, 58, 759 (1946).

Zernike, F., *Month. Not. Roy. Astron. Soc.*, 94, 377 (1934).

6.3 Wire and Double-Wire Tests

Cox, R. E., "The Hot Wire Foucault Test," *Sky and Telescope*, 25, 114 (1963).

DeVany, A. S., "Spherical Aberration Analysis of Double Wire Testing," *Appl. Opt.*, 6, 1073 (1967).

_____, "Supplement to: Aberrations by Double Wire Testing," *Appl. Opt.*, 9, 1720 (1970).

Gaviola, E., and R. Flatzeck, "Testing Method of Cassegrain Mirrors," *J. Opt. Soc. Am.*, 29, 480 (1939).

King, J. H., "A Quantitative Optical Test for Telescope Mirrors and Lenses," *J. Opt. Soc. Am.*, 24, 250 (1934).

Platzeck, R., and E. Gaviola, "Testing Method for Parabolas," *J. Opt. Soc. Am.*, 29, 484 (1939).

Schroeder, H., *Sci. Am.*, 196, 429 (1953).

7. RONCHI TEST

7.1 Testing of Spherical Mirrors and Systems without Spherical Aberration

Adachi, I., "Quantitative Measurement of Aberrations by Ronchi Test," *Atti. Fond. G. Ronchi*, 15, 461 (1960).

di Francia, G. Toraldo, "Geometrical and Interferential Aspects of Ronchi Test," Optical Image Evaluation Symposium, NBS Circular 256, p. 161, ( ).

Erdos, P., "Ronchi Test of Fifth Order Aberrations," *J. Opt. Soc. Am.*, 49, 865 (1959).

Lumley, E. (R.E.C.), "Figuring a Paraboloidal with the Ronchi Test," *Sky and Telescope*, 22, 298 (1961).

Malacara, D., "Ronchi Test and Transversal Aberrations," *Bol. Obser. Tonant. y Tacub.*, No. 27, 73 (1965).

Porter, R. W., and J. A. Anderson, "Ronchi's Method of Optical Testing," *Astrophys. J.*, 70, 175 (1929).

Ronchi, V., "Forty Years of History of a Grating Interferometer," *Appl. Opt.*, 3, 437 (1964).

_____, "On the Phase Grating Interferometer," *Appl. Opt.*, 4, 1041 (1965).

Sherwood, A. A., "Ronchi Test Charts for Parabolic Mirrors," *J. and Proc. Roy. Soc. of New South Wales*, 93, 19 (1959).

7.2 Testing of Aspherical Mirrors

Cornejo, A., and D. Malacara, "Ronchi Test of Aspherical Surfaces, Analysis and Accuracy," *Appl. Opt.*, 9, 1897 (1970).

Malacara, D., "Geometrical Ronchi Test of Aspherical Mirrors," *Appl. Opt.*, 4, 1371 (1965).

7.3 Testing of Lenses

Malacara, D., and A. Cornejo, "Modified Ronchi Test to Measure the Axial Chromatic Aberration in Lenses," *Appl. Opt.*, 10, 679 (1971).

8. HARTMANN AND MICHELSON TESTS

8.1 & 8.2 Testing of Spherical Mirrors and Systems without Spherical Aberration and Testing of Aspherical Mirrors

Bowen, I. W., "Final Adjustments and Tests of the Hale Telescope," *ASPA*, 62, 91 (1950).

Fox, P., "An Investigation of the 40" Objective of the Yerke's Observatory," *Astrophys. J.*, 27, 237 (1908).

Hartmann, J., *Z. Instrumentenk.*, 20, 51 (1900).

Lehman, H., "Hartmann's Test," *Z. Instrumentenk.*, 22, 325 (1902).

Malacara, D., "Hartmann Test of Aspherical Mirrors," *Appl. Opt.*, 11, 99 (1972).

Plaskett, H. H., "Oxford Solar Telescope and Hartmann Test of Its Performance," *Roy. Astron. Soc.*, 99, 219 ( ).

_____, "82-Inch Mirror of McDonald Observatory," *Astrophys. J.*, 89, 84 (1939).

Schultz, D. H., "A Hartmann Test Reduction Program," *Appl. Opt.*, 7, 119 (1968).

Stetson, H. T., "Optical Tests of the 69-inch Perkins Observatory Reflector," *J. Opt. Soc. Am.*, 23, 293 (1933).

Williams, T. L., "A Spot Diagram Generator for Lens Testing," *Optica Acta*, 15, 553 (1968).

8.3 Michelson Test

Cotton, A., *Physica*, 1, 274 (1921).

De, M., and M. K. Sen Gupta, *J. Opt. Soc. Am.*, 51, 158 (1961).

Michelson, A. A., "On the Correction of Optical Surfaces," *Astrophys. J.*, 47, 283 (1918).

Vaidya, W. M., and M. K. Sen Gupta, *J. Opt. Soc. Am.*, 50, 467 (1960).

9. STAR TESTS

9.1 Testing for Chromatic Aberrations

Calvet, E., "Perfectionnement Aux Bancs d'Optique," *Rev. Opt.*, 27, 245 (1948).

Herriot, W. J., "A Photoelectric Lens Bench," *J. Opt. Soc. Am.*, 37, 472 (1947).

Houghton, J. L., and E.W.H. Selwyn, "Lens Testing Bench," *J. Sci. Instr.*, 15, 367 (1938).

Kingslake, R., "A New Bench for Testing Photographic Lenses," *J. Opt. Soc. Am.*, 22, 207 (1932).

Leistner, K., B. Marcus and B. W. Wheeler, "Lens Testing Bench," *J. Opt. Soc. Am.*, 43, 44 (1953).

Washer, F. E., and W. R. Darling, "Factors Affecting the Accuracy of Distortion Measurements Made on the Nodal Slide Optical Bench," *J. Opt. Soc. Am.*, 49, 517 (1959).

Welford, W. T., "On the Limiting Sensitivity of the Star Test for Optical Instruments," *J. Opt. Soc. Am.*, 50, 21 (1960).

10. HOLOGRAPHIC AND MOIRE TECHNIQUES

10.1 Interferometers using Real Holograms

Baker, L. R., and T. L. Williams, "New Electronic Wavefront Plates," *Appl. Opt.*, 4, 285 (1965).

Bryngdahl, O., "Shearing Interferometry by Wavefront Reconstruction," *J. Opt. Soc. Am.*, 58, 865 (1968).

_____, "Multiple Beam Interferometry by Wavefront Reconstruction," *J. Opt. Soc. Am.*, 59, 1171 (1969).

Champagne, E., "Optical Mehtod for Producing Presnel Zonal Plates," *Appl. Opt.*, 7, 381 (1968).

Chan, Henry M., and H. Horman, "Demonstration of the Application of Wavefront Reconstruction to Interferometry," *Appl. Opt.*, 5, 1237 (1966).

_____, "Zonal Plates Produced Optically," *Appl. Opt.*, 8, 1209 (1969).

Haines, K. A., and B. P. Hildebrand, "Surface Deformation Measurement using the Wavefront Reconstruction Technique," *Appl. Opt.*, 5, 595 (1966).

Hansler, R. L., "A Holographic Foucault Knife Edge Test for Optical Elements of Arbitrary Design," *Appl. Opt.*, 7, 1863 (1968).

Hildebrand, B. P., and K. A. Haines, "Interferometric Measurements Using the Wavefront Reconstruction Techniques," *Appl. Opt.*, 5, 172 (1966).

_____, K. A. Haines and R. Larkin, "Holography as a Tool in the Testing of Large Apertures," *Appl. Opt.*, 6, 1267 (1967).

Horman, M. H., "An Application of Wavefront Reconstruction to Interferometry," *Appl. Opt.*, 4, 333 (1965).

_____, and H. M. Chan, "Zone Plate Theory Based on Holography," *Appl. Opt.*, 6, 317 (1967).

Matsumoto, K., "Holographic Multiple Beam Interferometry," *J. Opt. Soc. Am.*, 59, 777 (1969).

Miles, C. L., "The Production of Fresnel and Sine Wave Zone Plates," *Appl. Opt.*, 7, 976 (1968).

Pastor, J., E. E. Evans and J. S. Harris, "Hologram-Interferometry," *Optica Acta*, 17, 81 (1970).

Rogers, G. L., "The Equivalent Interferometer in Holography," *Optica Acta*, 17, 527 (1970).

Schwider, J., Comptes Randus du Sumposium International Applications Holographie, Besancon, France, Julliet 1970.

Smart, R. N., "A Variable Transmittance Beam Splitter," *Appl. Opt.*, 9, 970 (1970).

Snow, K., and R. Vandewarker, "On Using Holograms for Test Glasses," *Appl. Opt.*, 9, 822 (1970).

Tsuruta, T., and Y. Itoh, "Holographic Two Beam Interferometry using Multiple Reflected Light Beams," *Appl. Opt.*, 8, 2033 (1969).

Van Deelen, W., et al., "Mirror Blank Testing by Real-Time Holographic Interferometry," *Appl. Opt.*, 8, 951 (1969).

10.2 Interferometers using Synthetic Holograms

Brown, B. R., and A. Lohman, *Appl. Opt.*, 5, 967 (1966).

Lee, W. H., *Appl. Opt.*, 9, 639 (1970).

Lohman, A., and D. Paris, *Appl. Opt.*, 6, 1739 (1967).

McGovern, A. J., and J. C. Wyant, "Computer Generated Holograms for Testing Optical Elements," *Appl. Opt.*, 10, 619 (1971).

10.3 Two Wavelength Holographic Interferometer

Haines, K. A., and B. P. Hildebrand, *Phys. Letter*, 19, 10 (1962).

Hildebrand, B. P., and K. A. Haines, *J. Opt. Soc. Am.*, 57, 155 (1967).

Tsuruta, T., et al., *Japan J. Appl. Phys.*, 6, 661 (1967).

Wyant, J. C., "Testing Aspheric using Two Wavelength Holography," *Appl. Opt.*, 10, 2113 (1970).

Zelenka, J. S., and J. R. Varner, *Appl. Opt.*, 7, 2107 (1968).

_____, and J. R. Varner, "Multiple-Index Holographic Contouring," *Appl. Opt.*, 8, 1431 (1969).

10.4 Uses of Moire Fringes

Lanyenbeck, P., "Optical Wavefront Mapping by Dual Interferometry," *J. Opt. Soc. Am.*, 58, 499 (1968).

Lohman, A., "Das Moire-Getter als Vicseitigs Testobjekt," *Optical Acta*, 6, 27 (1959).

_____, and D. E. Silva, "An Interferometer Based on the Talbot Effect," *Optics Communications*, 2, 413 (1971).

Ramsay, B. P., "A Grating Interferometer," *J. Opt. Soc. Am.*, 24, 253 (1934).

Vogl, G., "A Phase Grating Interferometer," *Appl. Opt.*, 3, 1089 (1964).

Von Lau, E., "Die Dupligramm Methode zur Auswertung von Interferogrammen (The Dupligram Method for Evaluating Interferograms)," *Optik*, 12, 23 (1955).

11. NULL TESTS USING COMPENSATORS

11.1 Dall Compensators

Brown, E. B., "An Experience with the Dall Null Test," *Sky and Telescope*, 14, 512 (1954).

Burch, C. R., "Reflection Compensators for Testing Paraboloids," *Roy. Astron. Soc.*, 96, 438 (1936).

Cox, A. E., "Construction of a Dall Null Tester," *Sky and Telescope*, 18, 222 (1958).

Dall, H. E., "A Null Test for Paraboloids," *J. of British Astron. Assoc.*, 57, 201 (1947); Amateur Telescope Making, Book Three, Ed. Scientific American, New York (1953).

Gascoine, S.C.B., "Null Test for Concave Mirrors," *Roy Astron. Soc.*, 100, 462 (1940).

Holleran, R. T., "Immersion Null Test for Aspherics," *Appl. Opt.*, 2, 1336 (1963).

_____, "Null Testing Telescope's Mirrors by Immersion," *Sky and Telescope*, 28, 242 (1964).

_____, "Third Order Wavefronts and Related Null Tests," *Appl. Opt.*, 5, 1244 (1966).

_____, "An Algebraic Solution for the Small Lens Null Compensator," *Appl. Opt.*, 7, 137 (1968).

James, W. E., and M. D. Waterworth, "A Method for Testing Aspheric Surfaces," *Optica Acta*, 12, 223 (1965).

Ross, F. E., "Parabolizing Mirrors without Flat," *Astrophys. J.*, 98, 341 (1943).

11.2 Offner Compensators

Lytle, J. D., "A Suggested Procedure for Testing Large Cassegrainian Optical Systems," *Appl. Opt.*, 9, 2497 (1970).

Offner, A., "A Null Corrector for Paraboloidal Mirrors," *Appl. Opt.*, 2, 153 ( ).

12. OTHER TESTS

Bryngdahl, O., Chapter II--Applications of Shearing Interferometry, Progress in Optics. Vol. IV, pp. 39-83, Ed. E. Wolf, North Holland (1965).

Candler, C., Modern Interferometers, Hilger & Watts Ltd., (1951).

Francon, M., Optical Interferometry, Addison-Wesley, New York, (1966).

Herriott, D. R., Chapter V--Some Applications of Lasers to Interferometry, Progress In Optics, Vol. VI, pp. 171-209, Ed. E. Wolf, North Holland, (1967).

Ingalls, A. G., Amateur Making Telescope, 3 Vols., Scientific American Inc., New York (1953).

Linfoot, E. H., Recent Advances in Optics, Oxford University Press (1953).

Martin, L. C., Technical Optics, Pitman and Sons Ltd., London (1960).

Osterberg, H., Production Phase Tests, Military Handbook MIL-HDBK-141, Section 16, U.S.A. Dept. of Defense, ( ).

Scott, R. M., Chapter 2--Optical Manufacturing, Applied Optics and Optical Engineering, Vol. III, R. Kingslake Ed., Academic Press (1967).

Shannon, R. R., Chapter 5--The Testing of Complete Objectives, Applied Optics and Optical Manufacturing, Vol. III, R. Kingslake Ed., Academic Press (1967).

Steel, W. H., Chapter III--Two Beam Interferometry, Progress in Optics, Vol. V, pp. 145-197, Ed. E. Wolf, North Holland (1966).

Strong, J., Chapter II--Procedures in Experimental Physics, Prentice Hall, Inc., (1938).

_____, Concepts of Classical Optics, Prentice Hall, Inc., ( ).

Tolansky, S., Multiple-Beam Interferometry, Clarendon Press, Oxford, England, (1948).

Twyman, F. W., Prism and Lens Making, Hilger and Watts Ltd., ( ).

Young, A. W., Chapter 7--Optical Workshop Instruments, Applied Optics and Optical Engineering, Vol. IV, R. Kingslake Ed., Academic Press, (1967).

ACKNOWLEDGMENTS

The authors would like to extend their appreciation to personnel who contributed to this study. These individuals are Richard Buchroeder, William McKinley, James Osmundsen, Stephen Shore, Robert Tornquist, and David Zachary.